DECOHESION OF GRAIN BOUNDARIES IN THREE-DIMENSIONAL STATISTICAL REPRESENTATIONS OF ALUMINUM POLYCRYSTALS

A Dissertation

Presented to the Faculty of the Graduate School

of Cornell University

in Partial Fulfillment of the Requirements for the Degree of

Doctor of Philosophy

by

Erin Iesulauro

August 2006

DECOHESION OF GRAIN BOUNDARIES IN THREE-DIMENSIONAL STATISTICAL REPRESENTATIONS OF ALUMINUM POLYCRYSTALS

Erin Iesulauro, Ph.D.

Cornell University 2006

Since the 1950's, researchers have studied fatigue crack propagation utilizing fracture mechanics. Such work has provided advances in calculating stress intensity factors, determining elastic-plastic crack tip parameters, and investigating the effects of crack closure. Predictions of fatigue life have been made using crack growth rate models. Over the years, this work has served to influence structural maintenance and damage tolerance philosophies; however, understanding, predicting, and simulating fatigue crack growth is still based on experimental curve fitting and phenomenological rate "laws."

The work discussed in this thesis is a step toward understanding fatigue crack incubation, nucleation and microstructurally small crack growth from a first principles approach. To this end, capabilities have been created and assembled to generate, mesh, analyze, and post-process 3D statistical representations of metallic polycrystals with cohesive grain boundaries. A component-based framework facilitates flexibility, growth, and multiscale modeling. Components are accessed and connected through Web service interfaces. The Polycrystal Generator accesses the components for generating, meshing, and assigning properties and boundary conditions to a 3D polycrystal sample. It also provides an interface to a molecular dynamics component to facilitate loosely coupled multi-scale analyses. Analyses

are conducted utilizing a parallel solution software package, PETSc, and in-house finite element library, FemLib. The large samples and resulting data is managed using Microsoft SQL Server 2000, an off-the-shelf relation database. Finally, sample geometries, mesh models, and results are visualized using PView, a real-time visualization tool created using OpenDX, Python, and SQL.

The assembled framework is used to conduct a parametric study of 3D statistical polycrystals under monotonic loading. The samples are analyzed with variation introduced in geometry, grain constitutive model and parameter values, cohesive grain boundary parameter values, and boundary conditions. This parametric study gives insight into how each variation influences when and where cracks nucleate.

Finally, the results from the parametric study are utilized to conduct simulations under cyclic loading. These analyses give insight into the ability to accurately capture grain boundary decohesion leading to fatigue crack nucleation.

BIOGRAPHICAL SKETCH

A native of Reynoldsburg, Ohio, Erin studied Civil Engineering at Ohio Northern University in Ada, Ohio. After receiving her BSCE in 1998 she left Ohio to pursue graduate studies at Cornell University with Professor Anthony Ingraffea. She received her Master of Science in 2001.

Build me straight, O worthy Master!

Staunch and strong, a goodly vessel,

That shall laugh at all disaster,

And with wave and whirlwind wrestle!

from *The Building of the Ship*

Henry Wadsworth Longfellow

ACKNOWLEDGEMENTS

The work contained in this thesis was supported by grants from NASA Langley Research Center (LaRC) NAG-1-0205, the National Science Foundation (NSF) Information Technology Research (EIA-0085969), NFS RI (EIA-9972853), and Defense Advanced Research Projects Agency (DARPA). Computational resources were [in part] provided by the Cornell Theory Center.

Special thanks to Professor Ingraffea and the members of the Cornell Fracture Group for their assistance, collaboration, and friendship. And finally to my family who have supported me and my endeavors.

TABLE OF CONTENTS

1 Introduction **1**
- 1.1 2D Statistical Representations of Aluminum Polycrystals 4
- 1.2 3D Statistical Representations of Aluminum Polycrystals 8
- 1.3 Multi-scale Approach 9
- 1.4 Thesis Outline 11

2 Summary of 2D Polycrystal Analyses **13**
- 2.1 Sample Generation 13
- 2.2 Grain Material Models and Property Assignment 14
- 2.3 Grain Boundary Representation 15
  - 2.3.1 Grain Boundary Property Assignment 15
  - 2.3.2 Cohesive Zone Models 16
  - 2.3.3 Coupled Cohesive Zone Model 17
  - 2.3.4 Unloading of the Coupled Cohesive Zone Model 19
  - 2.3.5 Interface Elements 21
- 2.4 Sub-Grain Sized Particles 21
- 2.5 Results 22
  - 2.5.1 Parametric Study 22
  - 2.5.2 Analyses Under Cyclic Loading 23
  - 2.5.3 The Influence of Sub-grain Sized Particles 24
- 2.6 Summary 28

3 Transition to 3D Simulations **30**
- 3.1 Generating 3D Polycrystal Geometries 31
- 3.2 Generating 3D Meshes 34
  - 3.2.1 Geometric Issues for Meshing 36
  - 3.2.2 Mesh Refinement Control 38
- 3.3 Constitutive Models and Elements Implemented in FemLib 41
  - 3.3.1 Grain Constitutive Models 42
  - 3.3.2 Bi-linear Cohesive Zone Model for Grain Boundary Representation 43
  - 3.3.3 Exponential Cohesive Zone Model for Grain Boundary Representation 46
  - 3.3.4 The Interface Element in 3D and Its Implementation 47
- 3.4 Parallel Solution 48
- 3.5 Data Management Using SQL Database 49
- 3.6 Visualization 50
- 3.7 Summary 51

4 Web Services and Multi-scale Modeling 54
4.1 Introduction . . . 54
4.2 Details of the Polycrystal Generator . . . 56
4.3 Multi-scale Modeling: Linking Scales . . . 65
4.3.1 Linking the Polycrystal and Atomistic Scales . . . 67
4.3.2 Modified Stillinger-Weber versus Orthotropic, Linear Elastic FE . . . 76
4.3.3 Isotropic Stillinger-Weber versus Isotropic, Linear Elastic FE 78
4.4 Summary . . . 84

5 Verification using 3D Polycrystals with Regular Grains 85
5.1 Constitutive Model Verification using Polycrystals with Cubical Grains 86
5.2 Verification Problem Definition . . . 88
5.3 Effects of Mesh Refinement on Verification . . . 93
5.4 Effects of Element Order on Computational Requirements . . . 94
5.5 Determining Optimal Computational Solution Parameters . . . 97
5.6 Investigation of an Exponential CCZM . . . 99
5.7 Problems Increasing Sample Size . . . 103
5.8 Investigation of Variation of Model Parameters on Effective Response and Self-Consistency . . . 107
5.9 Summary and Conclusions . . . 113

6 Grain Boundary Decohesion in Statistical 3D Polycrystals 115
6.1 Statistical 3D Geometry Generation . . . 115
6.2 Introducing Variation in Constitutive Parameters . . . 117
6.3 Description of Boundary Conditions and Loading . . . 118
6.4 Computational Resources Utilized . . . 120
6.5 Observations of Internal Variation . . . 123
6.5.1 Variation in Response Due to Grain Properties . . . 123
6.5.2 Variation in Response Due to Grain Orientation . . . 127
6.5.3 Variation in Response Due to Grain Boundary Parameters . 137
6.5.4 Variation in Response Due to Boundary Conditions . . . 138
6.6 Discussion . . . 142

7 3D Polycrystal Simulations Under Cyclic Loading 146
7.1 Setup . . . 146
7.2 Observations . . . 147
7.3 Discussion . . . 151

8 Conclusions 154

A Simulations on Statistical Representations of Polycrystals using Franc2D/L 161

Bibliography 205

LIST OF TABLES

4.1 Elastic Constants from Stillinger-Weber potentials. 69
4.2 Grain Material Parameter Values 73
4.3 Bi-Linear CCZM Parameter Values for Orthotropic Grains 74
4.4 Bi-Linear CCZM Parameter Values for Isotropic Grains 75

5.1 Grain Material and Grain Boundary Property Values 90
5.2 Rate-Independent FCC Crystal Plasticity Property Values 95
5.3 Data size and solution data for linear and quadratic analyses of 64 cubical grain sample with linear, elastic grains and cohesive grain boundaries. 97
5.4 Energetically Equivalent Exponential CCZM Properties 100
5.5 Number of analyses steps and computational time for various sized samples of cubical grain samples. 107
5.6 Grain Material Property Distributions 109
5.7 Effective Young's Moduli for 64 cubical grain sample with linear, elastic grains and without cohesive grain boundaries 110
5.8 Effective Young's moduli for 64 cubical grain samples with linear, elastic grains and cohesive grain boundaries 112

6.1 Linear, elastic isotropic grain material properties. 118
6.2 Rate-independent FCC crystal plastic grains material properties. . 118
6.3 Rate-dependent FCC crystal plastic grains material properties. . . 118
6.4 Bi-linear coupled cohesive zone model parameters. 119
6.5 Mesh and computational details for polycrystal samples with linear tetrahedra and interface elements. 121
6.6 Mesh and computational details for polycrystal samples with quadratic tetrahedra and interface elements. 121
6.7 Average E_{gr} and resulting E_{eff} for artificial polycrystals without cohesive grain boundaries. 124
6.8 Effective Young's moduli, E_{eff}, and global displacement at which softening was first detected, Δ_{soft}, for artificial polycrystals with cohesive grain boundaries. 126
6.9 Global displacement at which plasticity was first detected, Δ_{soft}, for samples with variation in grain orientation using rate-independent crystal plasticity. 131
6.10 Global displacement at which plasticity was first detected, Δ_{soft}, for samples with variation in grain orientation using rate-dependent crystal plasticity. 131
6.11 Global displacements at which yielding, Δ_{yld}, and cohesive softening, Δ_{soft}, are first detected for samples with various grain orientation and cohesive grain boundaries using rate-independent crystal plasticity. 136

6.12 Resulting E_{eff} and Δ_{soft} due to variation in cohesive grain boundary parameters. 138
6.13 Variation in E_{eff} due to boundary condition type in samples with linear, elastic grains. 140
6.14 Variation in Δ_{yld} due to boundary condition type in samples with rate-independent crystal plasticity and without cohesive grain boundaries. 141
6.15 Variation in E_{eff} due to boundary condition type in samples with rate-independent crystal plasticity and cohesive grain boundaries. . 141

7.1 Grain Material and Grain Boundary Property Values 147
7.2 Computational Time for Fatigue Analyses 149

LIST OF FIGURES

1.1 2D and 3D regular, repeating grain geometries used to simplify microstructure scale models [1]. 5
1.2 Micrograph provided by Alcoa Co. of a crack that has nucleated along a grain boundary. Incubation and MSCG has been influenced by the local geometry and texture in AA 7075-T6. 7
1.3 Continuous observation of microstructural degradation during tensile loading of AA 7075- T651 [2]. 7
1.4 Micrograph provided by Alcoa Co. of a crack that has nucleated along a grain boundary. Incubation and MSCG has been influenced by the local geometry and texture. 8
1.5 Overview of multi-scale approach to simulation of strength and life of a cracking structure. 10

2.1 Generation of Voronoi cell. 14
2.2 Coupled cohesive zone model 17
2.3 Possible unloading paths for the cohesive zone model. 20
2.4 6 noded interface elements and location of integration points. . . . 21
2.5 Fatigue Loading Spectrum [3]. 24
2.6 Grain geometry for fatigue crack nucleation simulation [3]. 25
2.7 Deformation, grain boundary opening (λ), and stress in the Y-direction (σ_{yy}) seen at the peaks of the cyclic loading. Grain boundary opening shown for the grain boundaries circled in deformed mesh [3]. 26
2.8 Cohesive opening and σ_{yy} contours under applied strain [4]. 27

3.1 Micrograph of AA 7075, 445x magnification [5]. 32
3.2 Microstructure of a AA 7075-T6 rolled sheet, 455x magnification [5]. 32
3.3 Alternate geometry generation technique through merging smaller Voronoi cells to form grains [6]. 33
3.4 18 copies of initial Voronoi nuclei used to create bounding cube. . . 35
3.5 Unbounded and bounded 10 grain Voronoi tessellations using the same set of initial points. 35
3.6 Removing short edges can result in making an originally planar facet non-planar. 37
3.7 Each edge within the geometry is defined by two vertices. A local CEL value equal to the minimum of the adjacent edge lengths and the global CEL is stored at each vertex. These CEL values will be used to subdivide the edge for meshing. 39
3.8 Subdivisions are created starting from each vertex and graduating across the edge. Dividing the edge in half can lead to an undesirable transition in subdivision lengths at the midpoint of the edge. . . . 40

3.9 The edge is question is divided into two segments based on the CEL values stored at each vertex. This allows for more graduation along the edge minimizing the discrepancy in subdivision lengths when the segments meet together. 40
3.10 Finite element mesh for a 64 grain sample. 41
3.11 Tvergaard and Hutchinson bi-linear CCZM [7]. 43
3.12 Smith and Ferrante exponential coupled cohesive zone model (CCZM). 46
3.13 2D and 3D triangular interface elements. 48
3.14 PView with OpenDX program and interactive control panels showing geometry inspection. 51
3.15 PView with OpenDX program and interactive control panels showing surface mesh inspection. 52
3.16 PView showing cohesive grain boundary results. 52

4.1 Geometry Tab of the Polycrystal Client. This tab collects information for generating a 3D Voronoi grain geometry using the *gen_poly* Web service. 57
4.2 Behind the scenes details of the Geometry Tab, including storing the parameter set and then generating the grain geometry. Red text indicates data being transmitted across the Internet. Purple boxes indicate components being used. 58
4.3 Retrieve Tab of the Polycrystal Client. This tab allows the user to retrieve a document from the XMLrepository. 59
4.4 Mesh Tab of the Polycrystal Client. This tab collects information for generating a 3D tetrahedral mesh using the PolyMesh Web service. 60
4.5 Behind the scenes details of the Meshing Tab, including retrieving a stored grain geometry and then generating the mesh. Red text indicates data being transmitted across the Internet. Purple boxes indicate components being used. 61
4.6 Attributes Tab of the Polycrystal Client, grain material sub-tab. This tab allows the user to specify material models and property distributions as well as boundary conditions through a series of sub-tabs. 62
4.7 Attributes Tab of the Polycrystal Client, boundary conditions sub-tab. This tab allows the user to specify material models and property distributions as well as boundary conditions through a series of sub-tabs. 62
4.8 Status Tab of the Polycrystal Client. This tab allows the user to check the current status of a request. 64
4.9 Project Tab of the Polycrystal Client. This tab tracks current UUIDs generated by other tabs as well as their type and user specified name. 65

4.10 Atomistic Tab of the Polycrystal Client. This tab gathers information including which geometry and mesh to retrieve from the XMLRepository to conduct an atomistic simulation. 66
4.11 Particle on a grain boundary simplified geometry. 68
4.12 Labeled grain boundary and particle-grain interfaces. 70
4.13 Atomic sample of Interface 14. 70
4.14 Traction-displacement relationships determined through molecular dynamic simulations for each of the 11 interfaces present in the sample using the Isotropic Stillinger-Weber potential. 71
4.15 Traction-displacement relationships determined through molecular dynamic simulations using the Isotropic Stillinger-Weber potential and the corresponding bi-linear cohesive model generated for Interface 14. 73
4.16 Simple tension boundary conditions. 77
4.17 MD results for the 30 $\mathring{A}$ sample using the modified Stillinger-Weber potential. 79
4.18 Interface opening in the loading direction for the 30 $\mathring{A}$ FE analysis with orthotropic, linear elasticity. 80
4.19 Deformed shape for the 30 $\mathring{A}$ FE analysis with orthotropic, linear elasticity. 81
4.20 MD results for the 30 $\mathring{A}$ sample using the isotropic Stillinger-Weber potential. 82
4.21 Interface opening in the loading direction for the 30 $\mathring{A}$ FE analysis with isotropic, linear elasticity. 83
4.22 Deformed shape for the 30 $\mathring{A}$ FE analysis with isotropic, linear elasticity. 83

5.1 Regular polycrystal samples using 50 μm cubical grains. 87
5.2 Simplified model of grains and grain boundaries as a series of elastic blocks and springs. 88
5.3 Weakened grain boundaries in the middle of the center plane of sample. 91
5.4 Simple tension boundary conditions. 91
5.5 Analytic and numeric displacement versus load curves for the 64 cubical grain sample under uniaxial tension. 92
5.6 Coarse and fine mesh models for the 64 cubical grain sample. . . . 94
5.7 Analytic and numeric displacement versus load curves for the 64 cubical grain sample with coarse and fine mesh models. 95
5.8 Load versus displacement curves for the 64 cubical grain sample with linear, elastic grains and bi-linear grain boundaries using linear and quadratic elements. 96
5.9 Load versus displacement curves for the 64 cubical grain sample with rate-independent plastic grains and bi-linear grain boundaries using linear and quadratic elements. 96

5.10 Load versus displacement curves for the 64 cubical grain sample using 0.010, 0.005, and 0.001 μm maximum step sizes. 99
5.11 Energy equivalent bi-linear and exponential CCZM. 100
5.12 Traditional application of cohesive zone models for a cantilevered beam specimen with a single failure path. 101
5.13 Analytic results using bi-linear and exponential CCZMs. 102
5.14 Analytic and numeric displacement versus load curve for the 64 cubical grain sample under uniaxial tension using the exponential CCZM. 103
5.15 Analytic and numeric displacement versus load curve for the 64 cubical grain sample under uniaxial tension. 104
5.16 Analytic and numeric displacement versus load curve for the 216 cubical grain sample under uniaxial tension. 105
5.17 Analytic and numeric displacement versus load curve for the 512 cubical grain sample under uniaxial tension. 105
5.18 Analytic and numeric displacement versus load curve for the 1000 cubical grain sample under uniaxial tension. 106
5.19 Load versus displacement for cubical grain samples with exponential cohesive grain boundaries. 108
5.20 Displaced shape of model with exponential cohesive grain boundaries for the 512 cubical grain sample. 108
5.21 Load versus displacement curves for the 64 cubical grain sample using uniform and random grain properties. 111
5.22 Load versus displacement curves for the 64 cubical grain sample using uniform and random grain properties. 111

6.1 Artificial 64 grain polycrystals generated using the Polycrystal Generator, with an average grain size of 50 mum and overall dimension of 0.2 mm. 116
6.2 Artificial 216 grain polycrystals generated using the Polycrystal Generator, with an average grain size of 50 mum and overall dimension of 0.3 mm. 116
6.3 Artificial 512 grain polycrystals generated using the Polycrystal Generator, with an average grain size of 50 mum and overall dimension of 0.4 mm. 116
6.4 Artifical 1,000 grain polycrystal generated using the Polycrystal Generator, with an average grain size of 50 mum and overall dimension of 0.5 mm. 117
6.5 Boundary condition scenarios applied to the analyses herein. 119
6.6 Finite element meshes for each sample size. 122
6.7 σ_{zz} stress contours for the 216(1) grain sample using linear, elastic isotropic grains with Uniform and Random1 instances of E_{gr}. . . . 125
6.8 Response curves for different geometries with all grains having the same or random grain parameters with cohesive grain boundaries. . 128

6.9 Final λ contours for the 216(1) grain sample with uniform and random values of E_{gr}. 129
6.10 Internal grain boundary damage for the 216(1) grain sample with uniform and random values of E_{gr}. 129
6.11 Response curves for different geometries with all grains having the same or random orientations using rate-independent crystal plasticity. 133
6.12 Elastic σ_{zz} contours for the 216(1) grain sample with uniform and random values of E_{gr}. 134
6.13 Response curves for different geometries with all grains having the same or random orientations with cohesive grain boundaries 135
6.14 Final λ contours for the 216(1) grain sample with uniform and random grain orientations and rate-independent plasticity. 136
6.15 Internal grain boundary damage for the 216(1) grain sample with random rain orientations and rate-independent plasticity. 137
6.16 Resulting different response curves due to fixed or random grain boundary properties. 139
6.17 Resulting different response curves due to various boundary conditions. 141
6.18 Resulting different response curves due to various boundary conditions. 142

7.1 Individual grain geometries subjected to fatigue loading. 147
7.2 Fatigue Loading History. 148
7.3 Boundary conditions applied to fatigue analyses. 148
7.4 Maximum λ per load cycle for the 216 grain sample. 150
7.5 Maximum λ per load cycle for the 512 grain sample. 150
7.6 λ contours for the 216-grain samples loaded under fatigue. 152
7.7 λ contours for the 512-grain samples loaded under fatigue. 153

8.1 Experimentally observed intergranular fatigue cracking in 7050-T6 (Photo courtesy of Alcoa, Inc). 155
8.2 3D polycrystal simulation of grain boundary decohesion. 155

A.1 Coupled cohesive zone model 166
A.2 Possible unloading paths for the cohesive zone model. 168
A.3 6-noded interface elements and location of integration points. . . . 169
A.4 16-element block. 177
A.5 Matlab figure output from DM_tess 183
A.6 FRANC2D/L showing the beginning of Grain Boundary Decohesion 187
A.7 Matlab figure output from DM_Particlelist 192
A.8 CCZM Pre-Processing Menus 204

Chapter 1

Introduction

Research since the 1950's has investigated fatigue crack propagation in polycrystalline metals using fracture mechanics. Such work has included such fundamentally important topics as calculating stress intensity factors; determining elastic-plastic parameters at the crack tip; using finite element, boundary elements, and finite difference methods for analysis; observing constraint effects on crack growth; discovering crack closure; determining crack growth rates laws; predicting fatigue life; and studying small crack growth behavior. In the 1980's and 1990's, military and commercial fleets of aircraft began to age, and fatigue was more often observed as a cause of fracture related failures. This renewed interest in a more fundamental understanding of the fatigue cracking process.

Fatigue crack growth is divided into phases: incubation, nucleation, microstructurally small crack growth (MSCG), long crack propagation (LCP), and failure. The study of LCP and failure has been fairly exhaustive with experiments conducted on specimens ranging from small lab specimens to full-scale components, and with analytical and numerical simulation efforts. The 1960's saw the beginning of research focusing on the incubation, nucleation, and MSCG phases. Observation showed nucleation and early growth along favorable slip systems. Small crack growth was shown to be highly influenced by microstructural features such as grain boundaries, voids, and small particles. It was also observed that nucleation is more likely to occur on the surface of a material, where local stresses are higher, stress concentrations induced by particles are higher, environmental effects are felt initially, and damage is more often found due to machining or operation.

Focusing on small crack behavior, researchers began investigating crack closure effects [8] and the size of plastic zones at the crack front [9] [10]. The plastic zone was described through models such as the Dugdale-Barenblatt strip yield model. Studies also began predicting crack growth rates. Predictors for large cracks included crack extension vs. number of cycles (da/dn) curves which were fit by the Paris law [11]. However, the growth rate laws developed were based primarily on empirical data matching, making them phenomenological models. The da/dn data are specific to the alloy tested, environmental conditions, boundary conditions, and the geometric configuration used, limiting the use of the resulting curves. Also, attempts to include the details of the underlying physics were sparse. For the short crack growth work, many experiments were conducted using specimens with long cracks and then focusing on additional short increments of growth [12] [13]. This practice ignores the underlying physics that cause a crack to nucleate. It also alters the environment in which a truly microstructurally small crack exists. Such experiments do not examine why a crack nucleates where it does or why some cracks incubate to macro-cracks and others arrest before becoming larger than the surrounding microstructural features. The local microstructure holds the key to these questions. Ignoring local variability in the microstructure ignores inherent variability present in a component or structure. Capturing this variability is necessary to accurately determine reliability at a structural scale.

The aerospace industry is especially concerned with fatigue in metals. Military and commercial aircraft fleets are getting older. The costs of building new aircraft are high, causing the current fleets to be in service past their design life. Therefore, maintenance practices have been reviewed and altered in the last few decades to take advantage of the most up-to-date information about fatigue cracking. In the

late 1960's, the Air Force maintenance plan replaced the under-skin of the KC-135, made of aluminum alloy AA2024, every 13,500 flight hours to avoid detectable damage or failure due to fatigue cracking. Re-testing of fatigue life in the early 1970's reduced the replacement time to every 11,500 flight hours. Fatigue damage, however, continued to be a problem. This prompted changes in the safe-life maintenance philosophy of the Air Force away from assuming an initially flaw-free aircraft and using 1/4 of the fatigue life of test specimens. This philosophy was replaced with a damage tolerance approach assuming the presence of flaws and focusing on monitoring crack growth and the resulting damage.

The safe-life maintenance philosophy assumes that a component is initially flaw free. Flaws are not accounted for until they are of a detectable size. The majority of fatigue crack research has therefore focused on growth after a crack has reached a detectable size. However, components are not initially flaw free. Mechanical processing of the material and milling processes to generate a specific component result in microscopic internal and surface flaws. However, Suresh [14] and Schijve [15] both noted that 60-80% of the fatigue life is concentrated in the incubation, nucleation and MSCG phases. All of these phases are greatly influenced by the local microstructure. A crack may grow to a detectable size and eventual cause structural failure or it may arrest almost immediately. Previous 2D simulations of metallic polycrystals conducted by this author have alluded to the microstructural influences on incubation, nucleation, and MSCG. These simulations and related work also support the need for including statistical information at the microstructural scale to capture the variability seen and to obtain reliability information at the structural scale. The research discussed herein expands on the previous simulations by extending to 3D statistical representations of aluminum polycrystals

to conduct non-deterministic numerical simulations of incubation and nucleation processes in polycrystalline aluminum alloys dominated by grain boundary damage mechanics.

1.1 2D Statistical Representations of Aluminum Polycrystals

Currently, there are many finite element and analytical software packages available to simulate fatigue crack growth. The packages provide material modeling varying from linear elasticity to orthotropic plasticity. The incubation/nucleation/MSCG process consists of the user placing a small (but microstructurally large) crack at an assumed critical location or location observed in experiment. Then, subsequent crack growth is determined by the empirical growth rate laws currently available, such as the Paris law [16]. Such modeling has given insight into the direction of crack growth and the fatigue life left after initial detection of a crack. Information gained has aided in new designs as well as redesign, patching and repair techniques, and maintenance planning. However, such modeling does not capture the full fatigue life. Nor does it consider the probability of the assumed initial crack actually occurring. The assumed location of the introduced crack may be a critical location; however, a crack may be more probable to reach a detectable or critical size in another location. Then what happens to the fatigue life and reliability of the structure?

In recent years, work has classified microstructural features to help understand the link between these features and corrosion behavior. The work of Gao *et al.* [17], Campestrini *et al.* [18], and Stanzl-Tschegg *et al.* [19] has focused on identifying

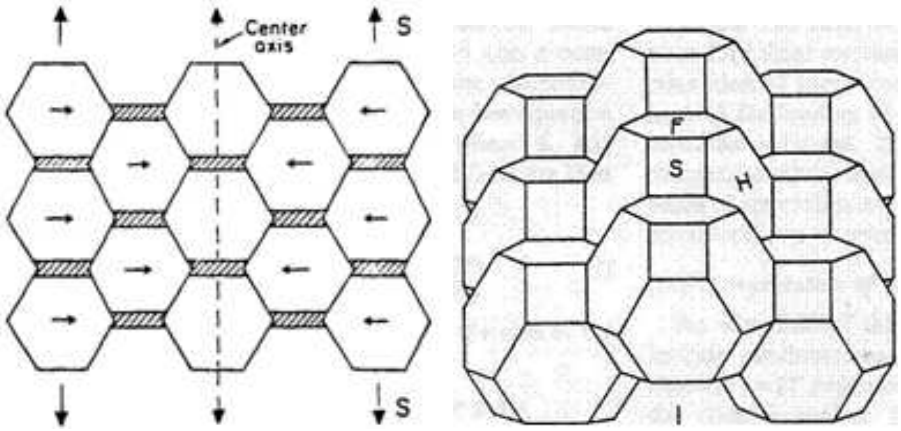

(a) 2D regular, repeating grain geometry.

(b) 3D regular, repeating grain geometry.

Figure 1.1: 2D and 3D regular, repeating grain geometries used to simplify microstructure scale models [1].

microstructural features, their properties and their influence on corrosion behavior. The study of corrosion in metals has resulted in models for the growth of corrosion pits by Harlow and Wei [20]. This has sparked an interest in the microstructural influence on fatigue and fracture. 2D models have been created by Rice [21], Anderson and Rice [1], and Raj and Ashby [22] to simulate the formation and growth of voids along grain boundaries and the resulting decohesion. Such work has also been done in 3D using truncated octahedron elements to represent individual grains. Cavitation models are then used between the elements to model high temperature creep [23]. This area of research, however, has been mostly constrained to effects due to creep at high temperatures since fracture processes in this regime have been observed to be dominated by intergranular fracture. It has also been restricted to regular, repeating grain structures such as 2D honeycombs and 3D truncated dodecahedra as shown in Figure 1.1.

Carranza and Haber [24] investigated intergranular fracture due to oxygen embrittlement, rather than high temperature creep, in 2D. In this work, grain bound-

aries perpendicular to the loading direction were modeled in a finite element mesh using interface elements controlled by a traction-displacement relationship. The surrounding elements followed an elastic-viscoplastic material model. The model was loaded under tension and a Mode I crack was started at one edge by releasing the interface element. As loading was applied, the interface element ahead of the crack tip began to decohere. The crack continues to incubate in Mode I for the length of the sample. This work was restricted to a single grain boundary loaded in Mode I.

Previous work conducted by this author and other members of the Cornell Fracture Group has also focused on crack nucleation at the polycrystal scale. In Iesulauro [3], previous 2D grain boundary decohesion simulations were expanded by introducing non-regular, non-repeating geometry and variation in internal properties. Figure 1.2 shows a crack that has nucleated along a grain boundary. The initial incubation of this crack has been controlled by the local geometry and texture. In the numerical simulations, the grain geometries were generated using the Voronoi tessellation technique. Grains and individual grain boundaries were assigned individual sets of parameters from a distribution of properties. Analyses were conducted under monotonic and cyclic loading to study how local geometry and property variation influenced crack incubation, nucleation, and MSCG. Additional features were incorporated in the pre-existing simulation code, FRANC2D/L [25], such as coupled cohesive zone models (CCZM), interface elements, automatic insertion of interface elements along grain boundaries and assignment of CCZM parameters, and visualization capabilities to accommodate polycrystal analyses. These initial analyses were then expanded by introducing sub-grain sized particles to the geometries [4]. These particles have been observed to be frequent nucleation sites due

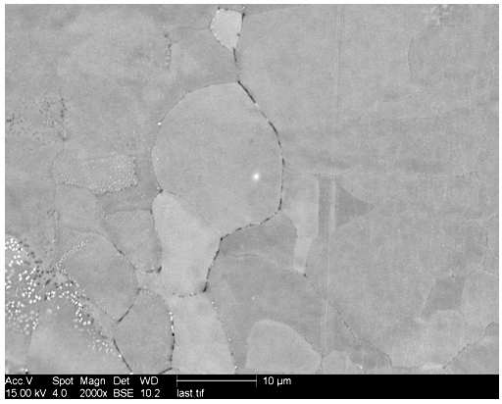

Figure 1.2: Micrograph provided by Alcoa Co. of a crack that has nucleated along a grain boundary. Incubation and MSCG has been influenced by the local geometry and texture in AA 7075-T6.

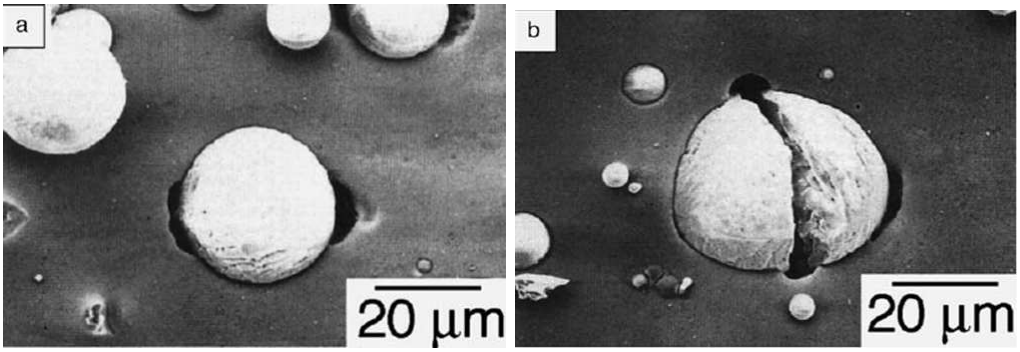

(a) Particle bedonding (b) Particle cracking

Figure 1.3: Continuous observation of microstructural degradation during tensile loading of AA 7075- T651 [2].

to the particle debonding or cracking and introducing a new stress concentration as shown in Figure 1.3 and 1.4 [2]. Ultimately, however, these analyses could only yield insight into the crack nucleation/incubation processes. The analyses were limited by 2D assumptions and the use of continuum material models.

Therefore, the existing 2D capabilities are expanded to 3D. This requires expanding the current implementations of the cohesive models and interface elements to 3D and other computational considerations due to the increased size of the models. This allows the use of more accurate constitutive models to represent grain

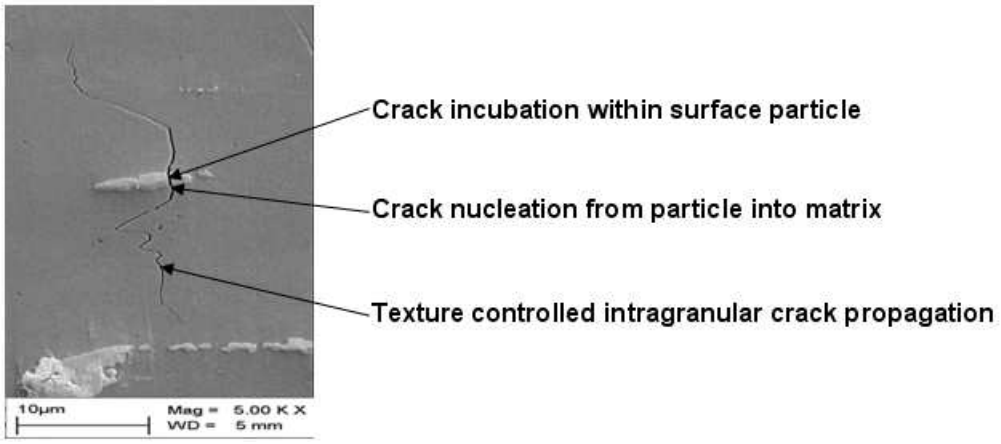

Figure 1.4: Micrograph provided by Alcoa Co. of a crack that has nucleated along a grain boundary. Incubation and MSCG has been influenced by the local geometry and texture.

behavior such as plasticity models that account for slip along preferred crystallographic planes within the grains.

1.2 3D Statistical Representations of Aluminum Polycrystals

Given the limitations of 2D polycrystal analyses, researchers are beginning to explore the potential of 3D analyses. The ever increasing computational resources available are also contributing to the ability to generate more complex samples and conduct more detailed and higher resolution analyses. Initial 3D polycrystal analyses included investigations of creep cavitation along grain boundaries. However, the geometry models were regular, repeating structures [1, 23, 26]. Extensive work has been conducted on texture evolution and capturing the plastic response at the grain level [27, 28]. Again, much of this work includes regular grain structures such as bricks and truncated octahedra. However, such work has shown the importance of using constitutive models that are sensitive to the crystallographic

response. Previous 2D analyses, conducted by this author, used continuum constitutive models for the grain behavior. Initial analyses using 3D Voronoi tessellations have been conducted by Zhao *et al.* [29], but used von Mises plasticity to capture the plasticity of the grain. Such models have no regard for preferred planes along which plastic slip will occur; therefore, grain orientation has no effect on the resulting stress response.

The research presented in this thesis moves beyond 2D to 3D non-regular,non-repeating grain geometries and introduces non-continuum constitutive models for grain behavior and 3D CCZM for grain boundary behavior, to capture the incubation/nucleation stages of the fatigue crack process. The resulting samples are more complex, have higher fidelity constitutive response, and higher resolution than previous 2D and 3D polycrystal analyses.

1.3 Multi-scale Approach

The continuum-level fatigue simulation work mentioned previously consists of modeling a component with finite elements utilizing one of various continuum material models and then inserting a crack and loading cyclically. This approach assumes the material is homogeneous and obscures the details occurring at smaller length-scales that precipitates fatigue crack incubation/nucleation/MSCG. The local material properties at the polycrystal scale are inhomogeneous resulting in a grain geometry and variation in the local stress/strain fields. These features determine when and where fatigue cracks nucleate and which ones grow to macro-cracks.

Just as the macroscopic response results from the polycrystal-scale features, properties of polycrystal features, such as grain boundaries, are in turn dependent on the atomic scale. As each length scale influences the next lower scale and is

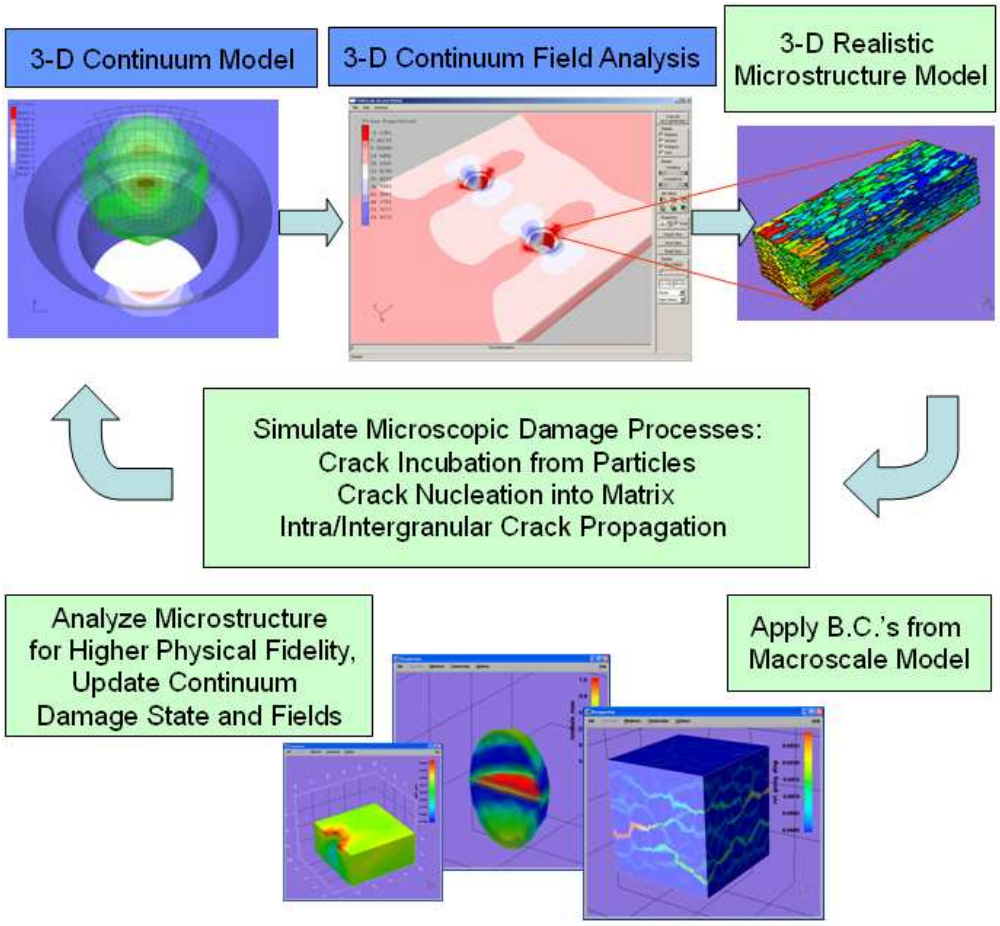

Figure 1.5: Overview of multi-scale approach to simulation of strength and life of a cracking structure.

informed by the previous higher scale, investigation of individual responses can benefit by using a loosely coupled multi-scale approach.

Figure 1.5 shows an overview of the multi-scale modeling simulation loop to determine the strength and life of a cracking structure. The loop begins with a 3D continuum model (upper left). A full-scale 3D analysis is conducted on an FE model of this component to automatically identify "hot spots" for crack nucleation (upper center). Next (upper right), a statistically accurate representative volume element (RVE) is automatically generated at the microstructural scale of the material. This model is located in an identified "hot spot" and has statisti-

cally accurate grain geometry and texture. The local stress/strain fields at the "hot spot" are applied to the microstructure model as boundary conditions. Moving downscale, an FEA is conducted on the RVE simulating the crack nucleation mechanics within a grain or grain boundary and the growth and coalescence of many such cracks leading to a microstructurally large crack (bottom). Finally, moving back upscale, the full-scale FE model is informed of the damage that has occurred at the lower length scale and re-evaluated. This process is repeated until all cracks have arrested or the component fails.

The 3D simulation capabilities and framework discussed herein were developed with microstructural and multi-scale modeling in mind. The framework consists of individual components for conducting specific tasks such as grain geometry generation, meshing, numerical analysis, and visualization. These components are all equipped with Web service interfaces so they may be connected to each other and other researcher's components via the Internet to conduct a full analysis. The framework is discussed and a multi-scale example is shown linking the polycrystal and atomic scales.

1.4 Thesis Outline

Previously, 2D non-deterministic analyses were conducted on statistical representations of polycrystal aluminum alloys. While this work provided insight into modeling metallic polycrystals and grain boundary damage mechanics, it was not able to capture the crystallographic influences on grain response or the through thickness variation. The research herein focuses on expanding the current 2D techniques and capabilities to 3D within a flexible and multi-scale framework to investigate incubation and nucleation processes in polycrystal aluminum alloys dominated by

grain boundary damage mechanics.

The following chapter summarizes the previous 2D work conducted and the analysis results. Chapter 3 discusses how the techniques and tools used in 2D are extended to 3D. This includes generating 3D geometries, issues encountered during meshing, extensions to the CCZM and interface elements, as well as computational considerations and visualization. The framework in which these capabilities are used is designed for multi-scale modeling with Web service interfaces available. Chapter 4 discusses how the current polycrystal scale models and simulations can be incorporated in a multi-scale analysis through the use of Web service interfaces. An example using the Web service interface to bridge the atomic and polycrystals scales is also shown.

A series of verification analyses are conducted on cubical grain geometries before conducting analyses with complex 3D geometries. Chapter 5 discusses the suite of tests conducted using a family of cubical grain polycrystal samples to verify the constitutive models being used and tests for mesh and numerical convergence issues. Chapters 6 and 7 discuss the results of analyses of 3D statistical representations of polycrystals under monotonic and cyclic loading, respectively. Finally, conclusions are summarized and future work discussed in Chapter 8.

Chapter 2

Summary of 2D Polycrystal Analyses

Previous research conducted by this author explored the polycrystal response and crack nucleation through grain boundary decohesion in 2D. Polycrystal geometry and mesh models were generated and grain and grain boundary properties were assigned. These samples were loaded monotonically and cyclically to observe the heterogeneous response of the polycrystal and to begin to understand the influences on when and where grain boundaries would decohere and nucleate cracks. The following models were generated using preprocessing tools designed using MATLAB [30, 31] and analyzed using FRANC2D/L [32, 3]. The manual for generating and analyzing 2D polycrystal samples is found in Appendix A.

2.1 Sample Generation

The 2D representation of the grain geometry can either match a single observed polycrystal sample or represent the average geometry seen over many samples. Statistical representations of the grain geometry are used. The polycrystal samples generated statistically match observations in terms of quantities such as average grain size and aspect ratio. However, samples do not exactly match any single observed geometry. For this work, the Voronoi tessellation technique [33, 34] is chosen as the method to create the grain geometries.

Voronoi tessellations begin from a random distribution of nuclei, or points. Chords are generated connecting pairs of nuclei. These chords are then perpendicularly bisected to create the edges of a polygon (Figure 2.1). Each nucleus then defines a polygon within which all points are closer to the nucleus than to

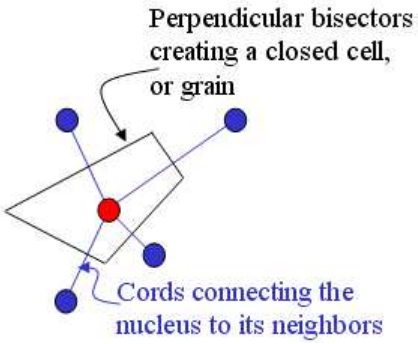

Figure 2.1: Generation of Voronoi cell.

any other [35]. This process best represents the initial forming of the grains from dendrite sites within a melt with isotropic growth rates [36].

This particular choice represents the initial polycrystal structure or annealed structure well. However, Voronoi tessellations do not capture the distortion of the grains due to mechanical processing, such as rolling. Since this work is done in 2D, the Voronoi tessellation technique provides good geometry with which to test modeling choices and software capabilities and make initial observations. For analysis, the geometries generated are meshed using a triangular advancing front meshing algorithm [37].

2.2 Grain Material Models and Property Assignment

Once the geometry of a polycrystal is in place, material properties are assigned to each grain. Current material model options in FRANC2D/L include elastic, isotropic; elastic, orthotropic; elastic-plastic, isotropic (von Mises); and elastic-plastic, orthotropic (Hill). See the FRANC2D/L User's Guide [25] for the necessary parameters for determining any of these models and James [32] for details concerning the plasticity implementations. For the chosen material model, each

grain is assigned an individual set of appropriate parameters. This produces a heterogeneous material sample.

2.3 Grain Boundary Representation

In a polycrystal, there are many mechanisms that can lead to the nucleation of micro-cracks. For example, fatigue can lead to the formation of slip bands within grains, which can lead to Stage I shear cracks. Also, a corrosive environment can lead to the failure of grain boundaries due to oxygen embrittlement. The previous and present polycrystal simulations focus on grain boundary decohesion as the primary source of localized damage. To allow decohesion to occur naturally, grain boundaries were modeled using coupled cohesive zone models (CCZM).

2.3.1 Grain Boundary Property Assignment

Grain boundaries naturally arise in polycrystals due to the lattice mismatch between adjacent grains. This region of disordered atoms behaves differently than the regular lattices of the adjacent grains. Therefore, the grain boundary is described with its own constitutive relationship, separate from the bulk grain material. A cohesive zone model is chosen to describe the strength and toughness of the grain boundaries. The cohesive zone model also serves as a criterion for nucleation of intergranular cracks.

The grain boundaries are allowed to decohere after reaching a critical normal, shear, or combined transmitted traction, thus gradually nucleating an intergranular crack. Once a critical opening/sliding is reached, a true crack has nucleated. An advantage of using such a model is that initial cracks are not arbitrarily introduced at the beginning of a simulation. Instead, cracks naturally occur due to

the heterogeneous stress field throughout the sample caused by the geometry and variations in properties. Cracking first begins along grain boundaries in areas with the highest stress concentrations.

2.3.2 Cohesive Zone Models

In theory, the stress at a crack tip in a linear and elastic material is singular. However, in practice materials, especially metals, have a yield stress at which they begin to deform plastically, negating the singularity. This leads to an area around the crack tip called the *crack tip plastic zone*. The stress in the plastic zone is limited by the yield stress. Several methods have been developed to determine the extent of the plastic zone. These include Irwin's plastic zone correction [38] and the strip yield models developed first by Dugdale [9] and Barenblatt [10].

Dugdale considered a fictitious crack tip a distance ρ ahead of the actual crack tip. The fictitious tip carries a compressive force equal to the yield stress that tends to close the crack. An application of this approach by Hillerborg [39, 40] is the *fictitious crack model* or the *cohesive zone model*. The cohesive zone model (CZM) assumes that the compressive force applied in the plastic zone follows a traction-displacement relationship. It is also assumed that this traction-displacement behavior can be considered a material property [41, 42].

In the present case, the damage represented by the displacement softening portion of the CZM is used to describe the decohesion of the grain boundaries leading to crack nucleation. Also, the area under the traction-displacement curve represents the critical energy release rate, G_c, necessary to nucleate a crack. The implementations available in FRANC2D/L [25], include independent normal and shear cohesive models as well as a coupled model added for this work. The normal

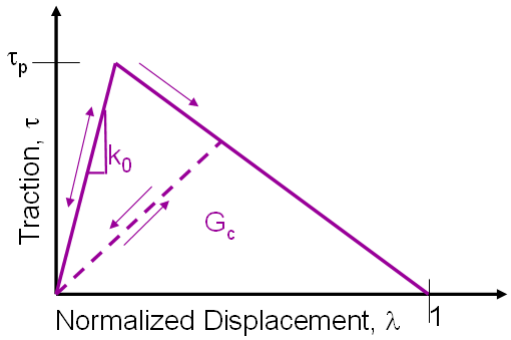

Figure 2.2: Coupled cohesive zone model

and shear models evaluate the transmitted traction independently of each other. In other words, the transmitted normal does not influence the amount of shear and vice versa. The coupled cohesive zone model (CCZM) implemented is adapted from the model developed by Tvergaard and Hutchinson [7], where the normal and shear components of the traction and displacement are combined into single measures, τ and λ, respectively (Figure 2.2), so that responses are coupled.

2.3.3 Coupled Cohesive Zone Model

Problems can arise with the segregated normal and shear models under mixed-mode loading. For example, since the shear and normal operate independently it is possible for shear forces to be transmitted across an interface while no normal traction is being transmitted due to large opening. This of course is physically incorrect. Since mixed mode loading is to be expected in polycrystal samples due to inclined grain boundaries, the following CCZM is implemented in the FRANC2D/L polycrystal simulations.

The CCZM begins from a traction potential, Φ.

$$\Phi(\delta_n, \delta_t) = \delta_n^c \int_\lambda \tau(\lambda')\mathrm{d}\lambda' \tag{2.1}$$

Φ is a function of the relative normal, δ_n, and tangential, δ_t, displacements between the faces of the grain boundary. λ is a non-dimensional separation measure for the relative opening and sliding defined by Eq. 2.2. The opening and sliding displacements, δ_n and δ_t, are measured at the mid-plane of the element and normalized to the relative critical displacement values, δ_n^c and δ_t^c, at which the separation is considered a true crack, or traction free surface, in pure Mode I and pure Mode II, respectively. The parameter β determines the ratio of shear to normal traction required to nucleate a crack. When the value of λ reaches 1 this indicates the complete decohesion of the grain boundary and nucleation of a crack.

$$\lambda = \left[\left(\frac{\delta_n}{\delta_n^c} \right)^2 + \beta \left(\frac{\delta_t}{\delta_t^c} \right)^2 \right]^{1/2} \tag{2.2}$$

For a given relative displacement between two grains the combined traction, τ, transmitted across the grain boundary can be determined from the CCZM. The combined traction can then be decomposed into normal, T_n, and shear, T_t, components by differentiating Φ with respect to δ_n and δ_t according to Eq. 2.3 and 2.4 respectively.

$$T_n = \frac{\partial \Phi}{\partial \delta_n} = \frac{\tau(\lambda)}{\lambda} \frac{\delta_n}{\delta_n^c} \tag{2.3}$$

$$T_t = \frac{\partial \Phi}{\partial \delta_t} = \beta \frac{\tau\left(\lambda\right)}{\lambda} \frac{\delta_n^c}{\delta_t^c} \frac{\delta_t}{\delta_t^c} \tag{2.4}$$

The CCZM parameters have the following physical implications. The initial *stiffness*, k_0, represents the initial elastic response of the grain boundary. Using a CCZM with an initially elastic response artificially introduces additional compliance to the sample. To minimize this unwanted artifact, k_0 must be set very high compared to E/h, where E is the Young's modulus of the grains and h is an average grain dimension. However, setting k_0 too high leads to numerical instability. The coupled value of τ_p relates to the peak normal strength, T_n^p, under pure Mode

I and peak shear strength, T_t^p, under pure Mode II according to Eq. 2.5 and 2.6 respectively. Whether plane stress or plane strain is assumed will vary the value of the coupled peak traction, τ_p, relative to the bulk yield stress.

$$T_p^n = \tau_p \tag{2.5}$$

$$T_p^t = \frac{\delta_n^c}{\beta \delta_t^c} \tau_p \tag{2.6}$$

In traditional continuum uses of CCZM, τ_p is considered to be three to five times the yield stress under plane strain, but only one to one and a half times the yield stress under plane stress. For the parametric study in Iesulauro [3], the value of τ_p is varied to observe the influence of the relative values. After the peak traction is reached, atomic bonds begin to break allowing the faces to separate. This post-peak portion of the traction-displacement curve simulates the softening of the grain boundary. At a specific distance the opposing faces no longer exert attractive forces on each other, resulting in a true crack. This corresponds to $\lambda = 1$.

2.3.4 Unloading of the Coupled Cohesive Zone Model

Since cyclic loading conditions are used in the polycrystal simulations, the unloading of the CCZM must be implemented. Two possible unloading paths considered are unloading according to the initial stiffness and unloading back to the origin. These two paths are shown in Figure 2.3. Both physical implications of the unloading paths and numerical difficulties are considered before the choice is made to unload to the origin.

Unloading according to the initial stiffness allows for permanent plastic de-

(a) Unloading according to the initial stiffness.

(b) Unloading back to the origin.

Figure 2.3: Possible unloading paths for the cohesive zone model.

formation in the grain boundary to occur. This reflects such theories as crack closure. However, this approach causes implementation problems. When the FRANC2D/L software calculates the stiffness matrix for the model, a tangent stiffness is determined for each element. For the interface elements used along grain boundaries the secant stiffness is calculated instead. The solution technique requires the stiffness matrix to be positive definite. Therefore, the negative slope of the softening portion of the curve is not acceptable. To compensate for this, the secant stiffness is calculated instead, which still captures the softening of the stiffness matrix. Keeping this in mind, it follows that unloading according to the initial stiffness would result in an increase in stiffness of the interface upon unloading and reloading.

Unloading back to the origin results in a fully closed interface. However, the interface instead sees damage by reloading along the unloading path which has a lower value than k_0. This also removes several difficulties that would be experienced in in implementing unloading following the initial stiffness, k_0. For this reason, unloading back to the origin is implemented.

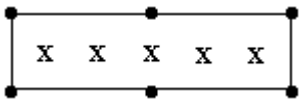

Figure 2.4: 6 noded interface elements and location of integration points.

2.3.5 Interface Elements

A convenient method for implementing the CZMs is through zero thickness interface or joint elements. The six-node interface element (Figure 2.4) implemented in FRANC2D/L creates traction forces as a function of the displacement prescribed by the CZM. The displaced location from the centerline of the element is determined at the nodal positions. From this, the relative displacements of node pairs are determined and interpolated to the Gauss integration points. At each of the integration points the traction is then computed from the specified CZM and integrated to determine the work equivalent nodal loads. The stiffness can also be determined from the CZM based on the relative displacement [43, 44].

2.4 Sub-Grain Sized Particles

Initial analyses [3] do not consider the discrete modeling of sub-grain sized particles. Particles below the size of the grains were considered to be smeared out and represented through the grain material properties. Subsequent work studies the influence of sub-grain sized particles on the polycrystal response [4].

Particle sizes are randomly distributed based on observed ranges. The particles are located inside individual grains and represented as n-sided polygons. Once the particles are geometrically inserted into the polycrystal geometry, the entire sample is meshed. The debonding of the particles from the matrix is again modeled using CCZMs. Particle debonding is observed to occur in aluminum alloys and acts as

sites for fatigue crack nucleation [45, 46]. The samples are loaded monotonically to observe the influence of the particles on the grain response and the particle debonding process.

2.5 Results

The tools discussed above for generating, meshing, analyzing, and visualizing 2D polycrystal samples with and without sub-grain sized particles are utilized to generate and analyze samples under monotonic and cyclic loading. The following summarizes the analyses conducted and the results.

2.5.1 Parametric Study

First, a parametric study is conducted on polycrystal samples without particles under monotonic loading. Multiple 0.5 mm samples consisting of 100 grains are generated and assigned different sets of grain and grain boundary properties. Analyses are conducted varying grain geometry, grain material models, grain properties, and grain boundary properties. Properties are assigned randomly from uniform distributions ranging ±5%, ±10%, or ±20%. Mean grain properties values are taken from bulk properties of AA 7075. The influence on failure path, stress patterns, and failure strain are observed.

Given various geometries with a distribution of grain material properties but with constant grain boundary properties, all samples fail at the same strain level with a through crack forming despite increasing variations in material properties. The path of the through cracks can be described as primarily Mode I.

Analyses are conducted using each of the available grain material models with variation in the properties assigned to each grain but with constant grain boundary

properties. Parameter sensitivity increases as anisotropy and plasticity are introduced. The analyses show plasticity in the samples especially near grain junctions which resulted in arresting crack growth. This indicated that assuming linear, elastic isotropic grains in future studies will not be sufficient. Material models capturing the true response of the grains, such as crystal plasticity models, must be utilized.

Additional analyses are conducted varying the grain boundary properties. Decreases in overall stress levels and failure strain are seen when property variation is increased to $\pm 20\%$. The mean value of the peak traction of the grain boundaries is also varied. As expected, when the mean peak traction is below the mean yield stress of the grains, decohesion of the grain boundaries leading to crack nucleation and propagation is seen rather than plastic deformation of the grains. For analyses where the mean yield stress is lower than the mean peak traction, the grains undergo plastic deformation while grain boundary decohesion is minimized or not seen at all.

2.5.2 Analyses Under Cyclic Loading

After concluding the parametric study, a single sample and property distribution is selected to analyze under cyclic loading. The geometry chosen is shown in Figure 2.6. The grains are assigned properties for the elastic-plastic, orthotropic (Hill) plasticity model. The samples are then loaded according to Figure 2.5 with the boundary conditions shown in Figure 2.6.

Figure 2.7 shows the deformed mesh, σ_{yy} stress contour, and the grain boundary opening for points 1, 3, and 7 of the loading history. Each subsequent cycle sees additional damage in the form of grain boundary opening and overall stress level.

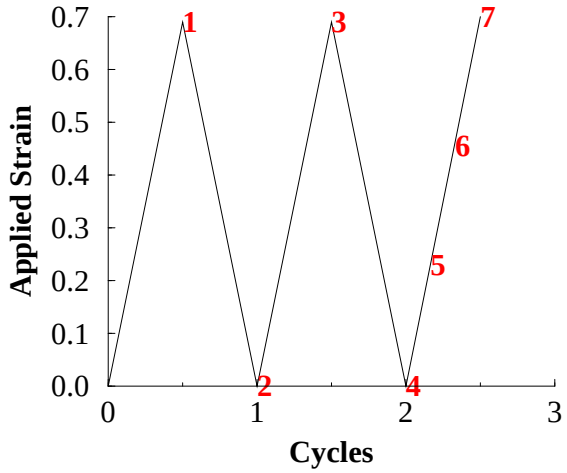

Figure 2.5: Fatigue Loading Spectrum [3].

For this sample the yield stress values are 500, 400, and 330 MPa ±5% for x, y, and z directions respectively. The σ_{yy} contours indicate that plastic yielding is occurring near the debonding grain boundaries.

This sample shows that the loading-unloading path of the CCZM does allow for damage to accumulate under cyclic loading. However, this example uses very few cycles. Additional analyses with longer loading histories will give insight into the true cyclic behavior of the CCZM and the polycrystal samples.

2.5.3 The Influence of Sub-grain Sized Particles

The influence of explicitly representing sub-grain sized particles was examined. Discussed here is a 15 grain sample measuring 0.5 mm square (Figure 2.8d). It contained a volume fraction of 2% particles with an average diameter of 8 μm. The grains were assigned properties for the elastic-plastic, isotropic (von Mises) plasticity model. The particles were assigned linear, elastic isotropic properties with a higher moduli than the surrounding grains. The particles are assumed to

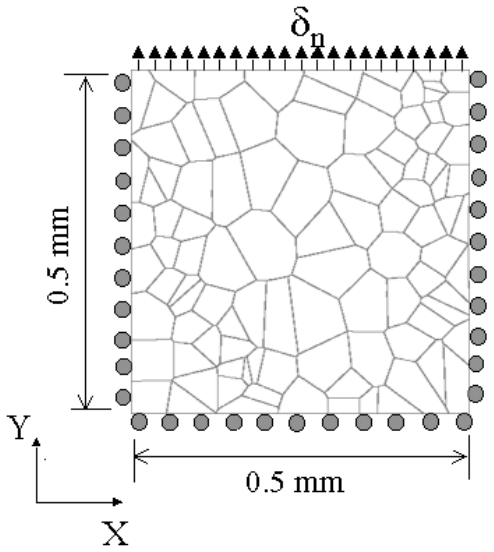

Figure 2.6: Grain geometry for fatigue crack nucleation simulation [3].

be harder than the grains and to behave in a brittle fashion.

The use of CCZMs as the grain/particle interface was shown to allow natural debonding of the particles from the surrounding grain. The particles also acted as stress concentrations within the grains themselves. Experimental observations have shown such particles to act as nucleation sites for fatigue cracks. Depending on the specific aluminum alloy and chemical make-up of the particle, the particles were observed to either fracture or debond from the grain. Both result in stress concentrations in the surrounding grain that cause cracks to nucleate. Further research is currently being conducted to replicate this work in 3D and to study how cracks propagate away from cracked or debonded particles through the surrounding grain [4].

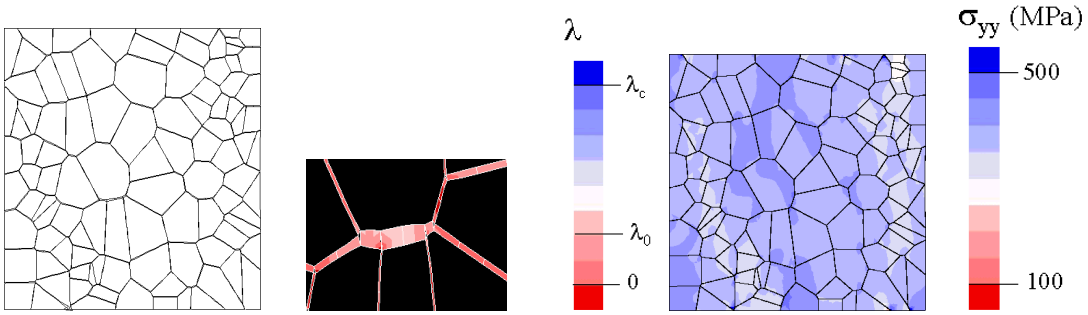

(a) Point 1 of loading history.

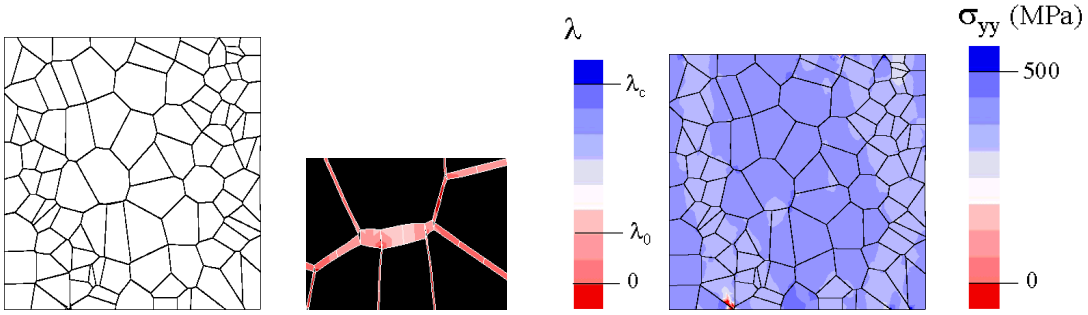

(b) Point 3 of loading history.

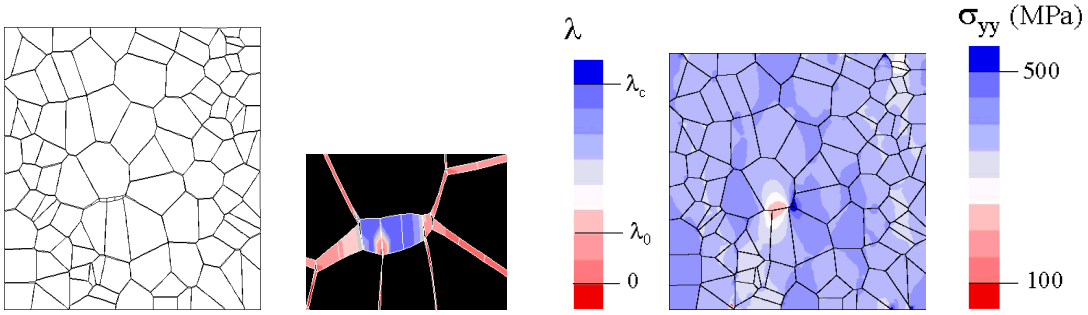

(c) Point 7 of loading history.

Figure 2.7: Deformation, grain boundary opening (λ), and stress in the Y-direction (σ_{yy}) seen at the peaks of the cyclic loading. Grain boundary opening shown for the grain boundaries circled in deformed mesh [3].

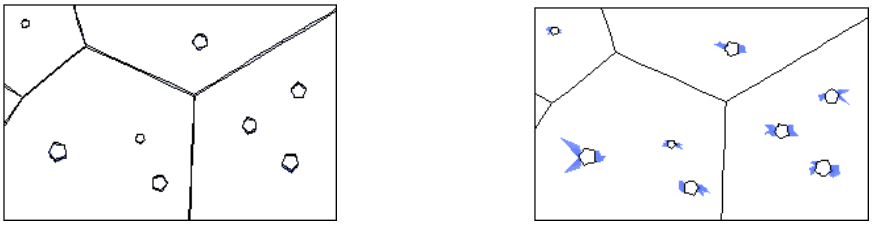

(a) 0.5% strain. σ_{yy} stress concentrations (right) around particles equal 0.40 GPa.

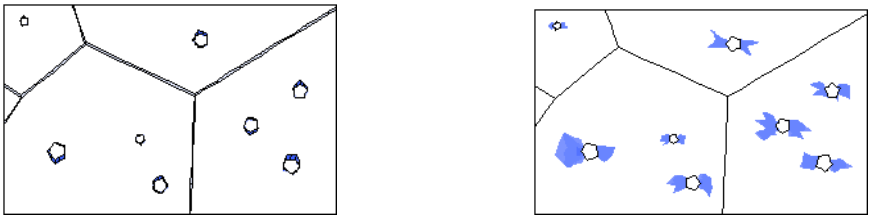

(b) 0.6% strain. σ_{yy} stress concentrations (right) around particles equal 0.48 GPa.

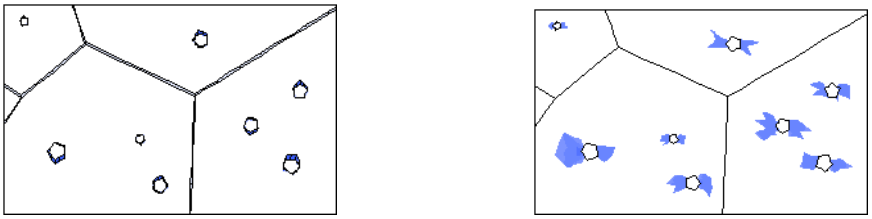

(c) 0.7% strain. σ_{yy} stress concentrations (right) around particles equal 0.56 GPa.

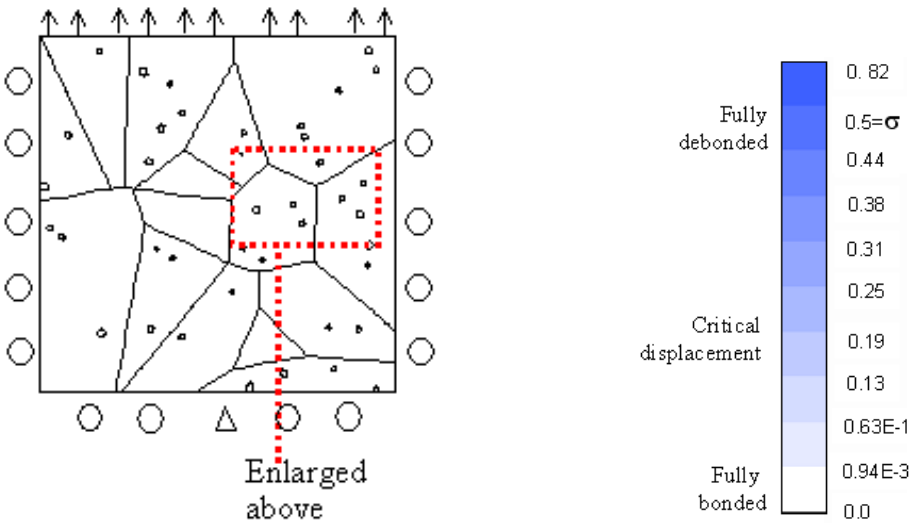

(d) Particle geometry and boundary conditions.

Figure 2.8: Cohesive opening and σ_{yy} contours under applied strain [4].

2.6 Summary

This research examines the need to look at smaller length scales to understand and describe the causes of fatigue crack incubation, nucleation, and MSCG. To this end, tools have been developed to create statistical polycrystal samples to represent polycrystalline metals and to simulate fatigue cracking due to grain boundary decohesion.

The sensitivity of the polycrystal response is observed by conducting a parametric study. Sensitivity to the variation of some material parameters is seen as parameters are assigned from wider distributions of values. It is observed that the elastic, isotropic material is the least sensitive to the range of values. Geometric effects dominate the response. The introduction of anisotropy increases the sensitivity to material property variation. Plasticity is also introduced through the von Mises and Hill material models. For both of these models, sensitivity is seen for the relative ranges of yield stress and the grain boundary strength. Here the results indicate that the relative mean values determine whether damage is dominated by plasticity or grain boundary decohesion. Also, in the case that the relative mean values are similar, the relative ranges determine whether plasticity or grain boundary decohesion is seen first.

To demonstrate the usefulness of these tools for studying fatigue crack incubation and nucleation, an example is shown. Decohesion of a grain boundary can be seen over a couple of cycles. For the final loading, the decohesion is artificially accelerated by straining the sample to the average macroscopic yield strain. At this point, the grain boundary completely decoheres resulting in localized nucleation of a crack. It is shown that additional decohesion does occur during the first two cycles; therefore, it can be expected that decohesion will continue over many

cycles, eventually resulting in the same response seen from applying the additional strain. The increase in strain also demonstrates how a small change in the strain level can greatly accelerate the damage process. This example also illustrates the post-processing feature that was added to FRANC2D/L to allow easy identification of decohering grain boundaries and the localized nucleation of true cracks.

To facilitate this analysis, the polycrystal geometry generation tool was augmented to include sub-grain sized particles. Analyses show the presence of particles creates stress concentrations within the grains. The use of cohesive grain-particle interfaces show how particles can decohere from the surrounding grain to form voids and possible crack nucleation sites within grains.

The addition of the CCZM, interface element, and visualization of grain boundary decohesion into FRANC2D/L and the preprocessing conducted in MATLAB, have resulted in a useful tool set with which to study the microstructural influences on fatigue cracking. Analyses highlight the need to correctly account for anisotropy and plasticity within the polycrystal sample. The representation of the grain material can be improved by replacing the simple continuum plasticity models with a crystal plasticity model. Analyses can also be improved by expanding the representation to 3D samples. The current tool set can be expanded for 3D with careful thought.

Chapter 3

Transition to 3D Simulations

Traditional fracture simulations have been conducted at the macroscopic scale. Continuum material descriptions and 2D simplifying assumptions work well at this scale. However, at the polycrystal scale, continuum models and 2D assumptions no longer adequately describe the physics being resolved. Continuum plasticity models such as the von Mises and Hill plasticity models assume the body acts isotropically or orthotropically without regard for preferred planes of plastic deformation resulting from microstructural features. Modeling at the polycrystal scale divides a body into discrete pieces with each having preferred planes along which slip can occur. The orientations of surrounding grains determine the stress and strain a given grain experiences and tries to accommodate. Therefore, accounting for each grain's orientation and tracking the active slip planes becomes important. Our previous 2D work assumes that an accurate picture of how a polycrystal responds can be drawn from a 2D slice. In typical continuum analyses, plane strain or stress assumptions are made to reduce the dimensions of a problem. However, at the polycrystal scale, assumptions about symmetry of the grain structure cannot generally be made. The aluminum polycrystals being considered herein do not exhibit a regular, repeating structure. Therefore, to more accurately model and analyze these polycrystals 3D models need to be used.

The previous 2D models were easily generated and meshed, required minimal memory to store, and utilized continuum material models. All analyses were conducted serially. Monotonic analyses conducted were completed quickly (5 to 30 minutes, depending on material model used, on a 2.4 GHz Xeon processor). Cyclic

loading analyses required up to 24 hours to complete. Transitioning to 3D models and analyses increases geometric, meshing, and material modeling complexity. The memory needed to store the models and resulting data is dramatically increased. Previously used visualization tools are inadequate for displaying and understanding results.

This chapter addresses how 3D geometries are created, improvements made to the existing 3D tetrahedral meshing capabilities to handle the complex geometries, and the 3D extensions made to the 2D interface element and CCZM implementations. Also discussed is the parallel solution package to be used, the use of SQL databases to manage the larger data sets, and how visualization of the models and results is done.

3.1 Generating 3D Polycrystal Geometries

For previous research, 2D grain geometries were generated using 2D Voronoi tessellations. This technique is again utilized for generating 3D geometries. The Voronoi tessellation procedure generates 3D convex polygonal cells of approximately equiaxed dimensions which are used to represent individual grains. This grain shape best describes an initial or annealed polycrystal structure without recrystallization (Figure 3.1) [5, 36]. However, this is not the structure seen, for instance, in aircraft fuselage panels and wing skins made from rolled sheets of aluminum alloys. The real microstructure exhibits pancake-shaped grains from rolling and variation in grain size due to recrystalization during rolling and heat treating (Figure 3.2) [5]. The Voronoi tessellation procedure gives an approximation of only the simplest geometry observed.

Techniques are being developed to generate more statistically realistic grain

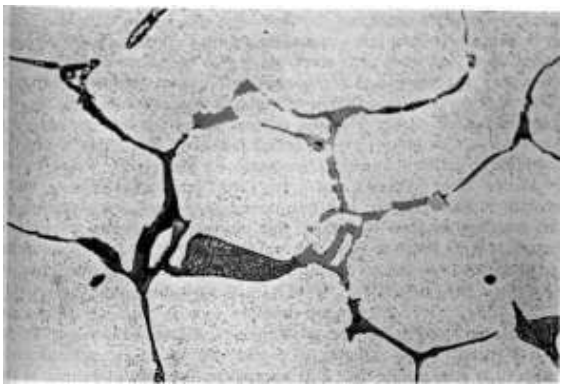

Figure 3.1: Micrograph of AA 7075, 445x magnification [5].

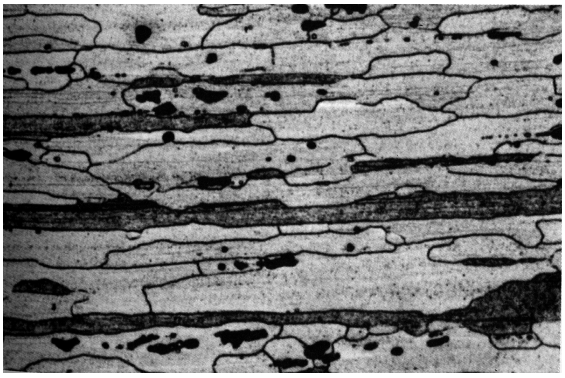

Figure 3.2: Microstructure of a AA 7075-T6 rolled sheet, 455x magnification [5].

structures for given processing histories. Figure 3.3 shows the steps for forming an irregular grain structure. First, an initial Voronoi tessellation is generated with cell sizes smaller than the observed grain size. Then, a set of ellipsoids is generated from the cell nuclei. From these ellipsoids a set of space filling ellipsoids is selected. The nuclei contained within each ellipsoid determines which cells will be joined to form a single grain. This allows cells along a preferred direction to be merged into grains. The resulting grain structure exhibits the elongated and more irregularly shaped grain structure seen in rolled sheets of aluminum alloys [6, 47]. Other techniques include 3D grain growth algorithms [29] and cellular automata approaches [48]. As in 2D, the relatively simple geometric form of the Voronoi tessellation allows for testing of capabilities such as meshing, data management, and solving before increasing the geometric complexity.

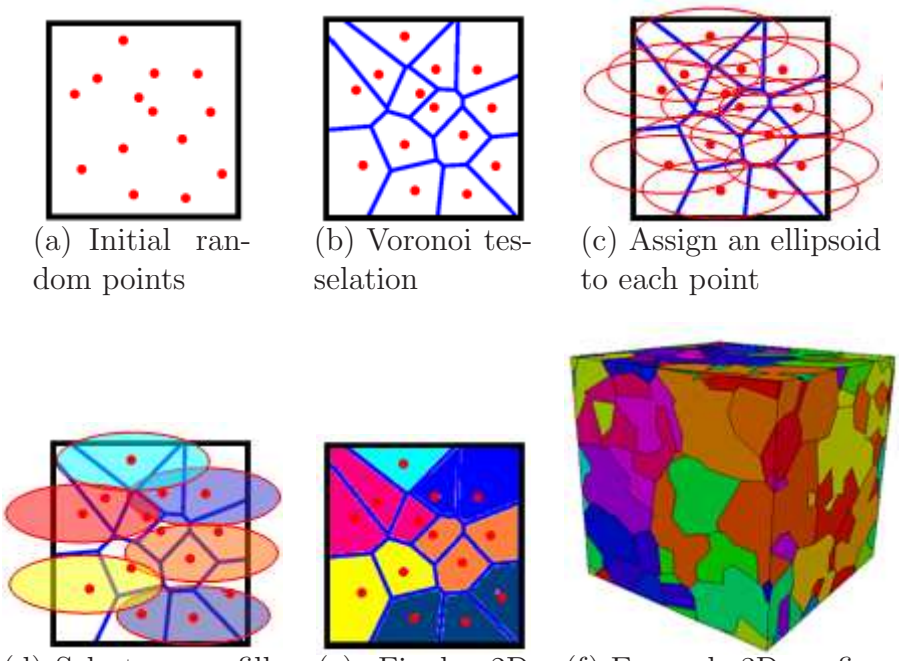

(a) Initial random points (b) Voronoi tesselation (c) Assign an ellipsoid to each point

(d) Select space filling set of ellipsoids (e) Final 2D configuration (f) Example 3D configuration

Figure 3.3: Alternate geometry generation technique through merging smaller Voronoi cells to form grains [6].

As discussed previously, Voronoi tessellations are generated from an initial set of points, or nuclei. Typically, Voronoi tessellations are created from a randomly generated set of points. However, this is not requires; any set of points can be used. Using various types of distributions to generate the set of points results in skewing the distribution of grain volumes to match experimental observations. For the purposes herein, sets of random points are used to generate grain geometries.

The Voronoi tessellation described above is unbounded. If the planes defining the convex hulls do not intersect other planes, then they continue to infinity, as seen in Figure 3.5a. However to be useful, the tessellations must be bounded. For the ease of applying boundary conditions, the tessellations used herein are bounded by a cube (Figure 3.5b). This requires additional steps to be taken. First, the set of initial points representing the grain centroids must fall within the bounding cube to guarantee the same number of grains in the resulting geometry. Any point falling on the boundary is either moved inward or disregarded. Next, the set of points is reflected across each face and boundary of the cube as shown in Figure 3.4. This results in 18 copies of the initial set of points being generated. After that, an initial tessellation is generated. By reflecting the initial points across the boundaries, mirror images of the tessellation are generated. This process results in generating cell or grain boundaries that align with the cube boundaries. Finally, all of the cells, or grains, that lie outside of the bounding cube are disregarded. This leaves only the grain geometry within the cube [49, 35].

3.2 Generating 3D Meshes

To conduct finite element analyses of the produced grain geometries, finite element meshes must be generated. Since each grain is assigned local material properties

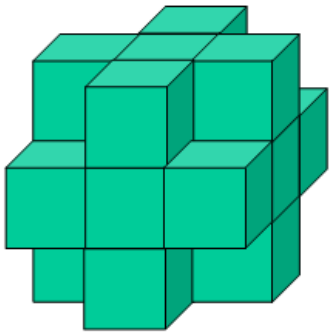

Figure 3.4: 18 copies of initial Voronoi nuclei used to create bounding cube.

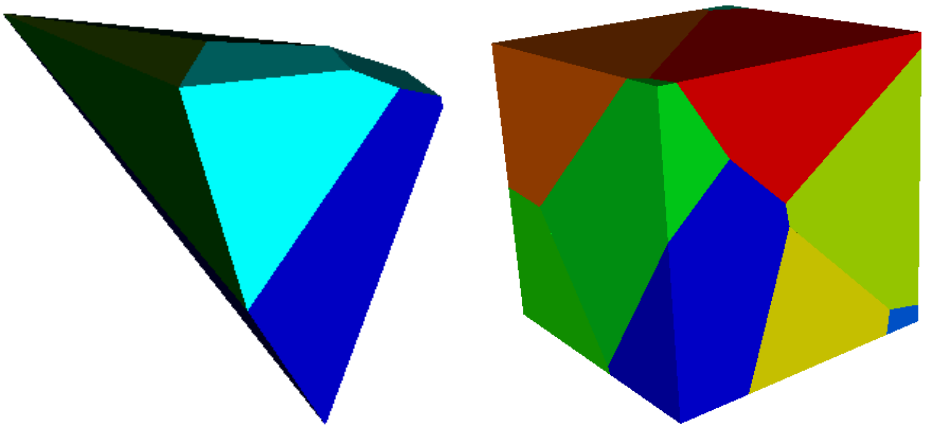

(a) Original, unbounded 10 grain Voronoi tessellation.

(b) 10 grain Voronoi tesselation bounded to a cube.

Figure 3.5: Unbounded and bounded 10 grain Voronoi tessellations using the same set of initial points.

and the grain boundaries are described separately, the mesh produced must respect and conform to these internal boundaries of the geometry. The mesh must be of sufficient quality to capture the desired mechanics without being overly refined, and therefore computationally expensive. In 2D, the mesh was generated by subdividing the grain boundary edges and then using an advancing front, triangular mesh generation algorithm to mesh each grain. This task was fairly trivial. However, replicating this process in 3D becomes more difficult.

A similar approached is used to generate a 3D mesh of the grain geometry. First, the edges defining the grains are subdivided. Next, the grain faces are meshed, as in 2D, using an advancing front triangular meshing algorithm. Finally, all of the faces defining a grain are assembled and an advancing front, tetrahedral meshing algorithm is utilized to generate the volume mesh for each grain [37]. Producing a valid mesh, let alone a quality mesh, is not trivial.

3.2.1 Geometric Issues for Meshing

The Voronoi tessellation process generates the structure dictated by its algorithm and the set of initial points chosen to represent grain centroids. The process can produce undesirable geometric entities for meshing. These include very short edges, sliver faces, and infinitesimal faces and grains. These can lead to the inability of the advancing front algorithm to find a surface or volume solution, the production of very poorly shaped elements, or the creation of an extremely refined mesh which can not be analyzed given available computational resources.

Although the Voronoi tessellation guarantees convexity, there are no guarantees about the minimum edge lengths or cell volumes. The edges within a tessellation can vary in length by many orders of magnitude. In a mesh, edges several orders

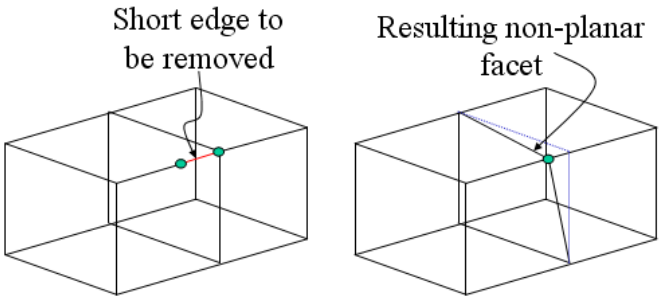

Figure 3.6: Removing short edges can result in making an originally planar facet non-planar.

of magnitude smaller than the largest edges are undesirable, especially when the edges are adjacent. Elements can end up with extremely small volume or with edge lengths possibly below machine precision or ill-formed. The shortest of these edges are therefore removed from the tessellation by merging the end-vertices into a single vertex located at the mid-point of the edge. All neighboring grains are updated to reflect the new geometry. For the samples discussed herein the minimum edge length is set to 5 μm. However, this process has the unintended consequence of possibly making the originally planar facets non-planar (Figure 3.6). Therefore, the surface mesher employed must be able to handle non-planar facets.

If the removed edge was part of a triangular facet, this facet is collapsed to an edge. Again the neighboring grain geometries are updated to reflect the presence of an edge rather than a facet. This results in removing the worst of the sliver facets present in the tessellation which should improve the chances of the surface and volume meshing process completing as well as improving mesh quality.

3.2.2 Mesh Refinement Control

Given the complex internal geometry of the Voronoi tessellation, control over mesh refinement is an issue. Ultimately, mesh refinement should be determined by the local geometry, i.e. finer near short edges and small facets and coarser near long edges and large facets with smooth transitions in between. Since the volume mesh is based on the surface mesh and the surface mesh is based on the edge subdivisions, the edge subdivisions must be made thoughtfully.

Each edge in the geometry must be subdivided; however, the neighboring edges connected to each end may vary widely in length compared to the current edge. Subdividing edges without consideration of their neighbors' length affects the quality of the resulting surface and volume mesh. To account for this variation, a local refinement measure is assigned to each vertex in the geometry based on the edges attached to it. Subdivisions are made along the edge starting from the vertices and moving inward along the edge. Initial subdivisions are based on the refinement measure of the appropriate vertex. Subsequent subdivisions are graded based on the ratio of the two refinement values to create a smooth transition along the edge. Adapting the subdivision size along an edge avoids ill-formed surface and volume elements due to large jumps in subdivision lengths and avoids over-refinement due to the presence of short edges in the geometry.

The refinement measure used here is the *characteristic element length* (CEL). The CEL determines the edge subdivision lengths and thus the edge length of the resulting surface triangles and volume tetrahedra. At each vertex, the minimum of the associated edge lengths and the global CEL set by the user as the maximum subdivision size, CEL_g, is stored as the local CEL value (Figure 3.7).

Once the local CEL values are determined, the edges are subdivided. First, the

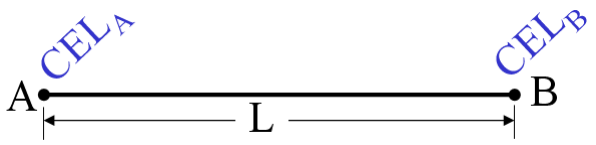

Figure 3.7: Each edge within the geometry is defined by two vertices. A local CEL value equal to the minimum of the adjacent edge lengths and the global CEL is stored at each vertex. These CEL values will be used to subdivide the edge for meshing.

edge is divided into two segments. Then, each segment is subdivided according to the CEL values contained in the vertices that define the segment. Simply dividing the edge in two equal segments can often lead to a large disparity in neighboring subdivision lengths at the mid-point as seen in Figure 3.8. This is likely if CEL_A and CEL_B are very different in magnitude and the edge is not sufficiently long to allow for enough gradation to occur. This can cause ill-formed surface and volume elements. Since the current focus is grain boundary decohesion, poor surface elements are undesirable. Instead, the edge is divided using a ratio of the CEL values, as shown in Figure 3.9. Using Eq. 3.1 and 3.2, the edge is divided into two segments, λ_0 and λ_1, where μ_0 is the $min(CEL_A, CEL_B)$ and μ_1 is the $max(CEL_A, CEL_B)$. The vertex with the smaller CEL is assigned to the larger portion of the edge to allow for additional gradation.

$$\lambda_0 = \frac{1}{\frac{\mu_0}{\mu_1} + 1} \tag{3.1}$$

$$\lambda_1 = 1 - \lambda_0 \tag{3.2}$$

Starting from each vertex an initial subdivision, δ_0, is made according to Eq. 3.3 where $\alpha_0 = 1.25$. Subsequent subdivisions are made according to Eq. 3.4. Each subsequent subdivision is a quarter larger than the previous, thus the subdivision size slowly increases along the length of the edge. However, at no time can δ_i exceed the user defined global CEL, CEL_g. This gradation provides smooth

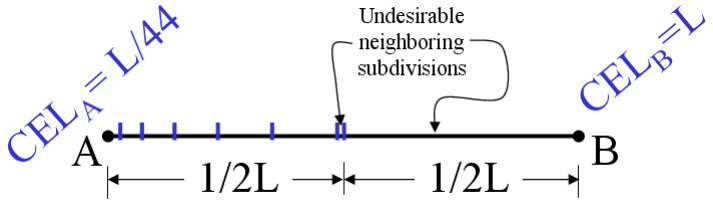

Figure 3.8: Subdivisions are created starting from each vertex and graduating across the edge. Dividing the edge in half can lead to an undesirable transition in subdivision lengths at the midpoint of the edge.

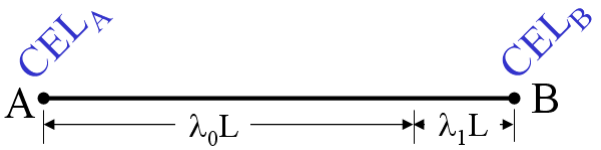

Figure 3.9: The edge is question is divided into two segments based on the CEL values stored at each vertex. This allows for more graduation along the edge minimizing the discrepancy in subdivision lengths when the segments meet together.

transitions from small to large elements and avoids over-refinement.

$$\delta_0 = \frac{\mu_0 \alpha_0}{L} \tag{3.3}$$

$$\delta_i = \frac{\mu_0 \alpha_i}{L} \quad \text{, where } \alpha_i = 1.25\alpha_{i-1} \tag{3.4}$$

Additional subdivisions are made along each segment until the next subdivision will exceed the length of the segment. If the remaining length of the current segment is less than δ_i, then the subdivision is terminated. The current segment is added to the remaining length and divided in half (Eq. 3.6). This is done to avoid very large or small segments being left when the subdivisions from each vertex meet.

$$\text{If:} \qquad l_0 L - \Delta_i \leq \delta_i \quad \text{, where} \quad \Delta_i = \sum_i \delta_i \tag{3.5}$$

$$\text{Then:} \qquad \delta_i = \frac{1 + \Delta_{i-1}}{2} \tag{3.6}$$

This process is repeated for each edge in the geometry. Once all edges are subdivided, surface and volume meshing can proceed. Given a high quality edge

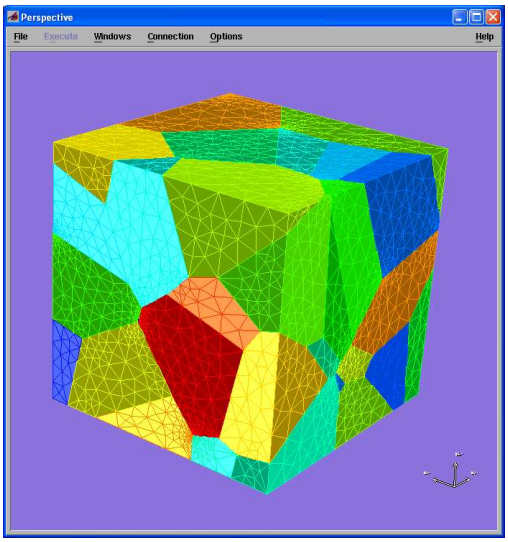

Figure 3.10: Finite element mesh for a 64 grain sample.

subdivision, the resulting surface and volume meshes have an increased probability of also being of high quality. Figure 3.10 shows a mesh generated for a 64 grain polycrystal using the meshing procedure described above.

3.3 Constitutive Models and Elements Implemented in FemLib

The solution framework used to conduct 3D simulations in this thesis consists of a parallel numerical solver package, PETSc [50], and a library containing element formulations and constitutive models, FemLib (unpublished in-house finite element library developed at the Cornell Fracture Group). PETSc has the capability of assembling a global stiffness matrix and force vector and then solving the resulting system of equations in parallel. However, it does not have internal knowledge of formulating individual elements or determining current material state. These functions are therefore carried out by FemLib. FemLib is designed such that element formulations and constitutive models are implemented separately and indepen-

dently. Constitutive models are implemented at the Gauss point level so that they may be used with any appropriate element type. This allows for maximum flexibility. The following describes the grain and grain boundary constitutive models implemented for the current research as well as the interface element formulation.

3.3.1 Grain Constitutive Models

FemLib currently has several constitutive models implemented. These include isotropic and orthotropic linear elasticity, von Mises plasticity, a classic rate-independent FCC crystal plasticity model [51], and a rate-dependent FCC crystal plasticity model [52]. In 2D, von Mises and Hill plasticity are utilized to investigate the extent of plasticity seen in the microstructure. These analyses show that plasticity is an important part of the polycrystal response under monotonic and cyclic loading (Section 2.5). However, at the polycrystal length scale, continuum plasticity does not properly account for the grain response. Therefore, crystal plasticity models are utilized for this research. These models account for the orientation of each grain and the slip along preferred slip planes resulting in more accurate representations of the local stress and strain fields. A classic rate-independent model along with a rate-dependent model developed by Maniatty *et al.* [52] are implemented in FemLib. The rate-dependent model requires the implementation of a mixed formulation quadratic element to be incorporated into the quasi-static framework used here. The element formulation and implementation are not discussed here. For details see Matous and Maniatty [52]. Both crystal plasticity models are investigated and results shown.

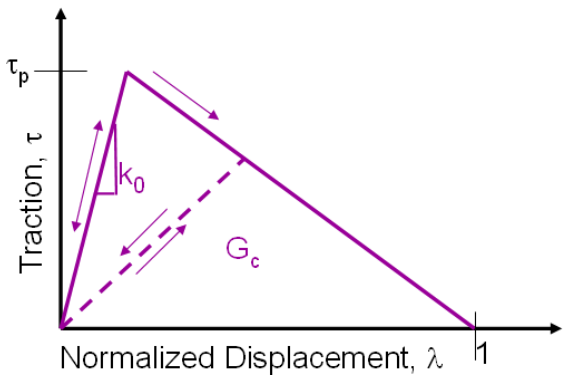

Figure 3.11: Tvergaard and Hutchinson bi-linear CCZM [7].

3.3.2 Bi-linear Cohesive Zone Model for Grain Boundary Representation

As in 2D, the grain boundary response is represented using coupled cohesive zone models (CCZM) implemented through interface elements. The extension to 3D of the Tvergaard and Hutchinson bi-linear CCZM previously used in 2D is discussed here [7].

The bi-linear CCZM shown in Figure 3.11 begins from a traction potential, Φ.

$$\Phi(\delta_n, \delta_t) = \delta_n^c \int_\lambda \tau(\lambda')\mathrm{d}\lambda' \tag{3.7}$$

Φ is a function of the relative normal, δ_n, and tangential, δ_t, displacement of the grain boundary. In 2D, δ_n and δ_t are straightforward as shown in Eq. 3.8 and 3.9. For 3D, a second tangential displacement is introduced (Section 3.3.4) thus replacing Eq. 3.8 and 3.9 with Eq. 3.10 and 3.11. λ is a non-dimensional displacement parameter combining the relative opening and sliding of the grain boundary defined by Eq. 3.12. The opening and sliding displacements, δ_n and δ_t, are normalized to the relative critical displacement values, δ_n^c and δ_t^c, at which the separation is considered a true crack in pure Mode I and pure Mode II, respectively.

The parameter β describes the ratio of shear to normal opening needed to nucleate a crack. When some combination of δ_n and δ_t results in the value of λ reaching or exceeding 1.0, this indicates the complete decohesion of the grain boundary and the formation of a true crack.

$$2D, \quad \delta_n = \delta_2 \tag{3.8}$$

$$\delta_t = \delta_1 \tag{3.9}$$

$$3D, \quad \delta_n = \delta_3 \tag{3.10}$$

$$\delta_t = |\delta_1 + \delta_2| \tag{3.11}$$

$$\lambda = \left[\left(\frac{\delta_n}{\delta_n^c} \right)^2 + \beta \left(\frac{\delta_t}{\delta_t^c} \right)^2 \right]^{\frac{1}{2}} \tag{3.12}$$

For a given relative displacement between two grains, the coupled traction transmitted across the grain boundary can be determined from the CCZM. The coupled traction can then be decomposed into the normal and two shear components by differentiating Φ with respect to δ_1, δ_2, and δ_3 as shown in Eq. 3.13 - 3.15.

$$T_3 = \frac{\partial \Phi}{\partial \delta_3} = \frac{\tau(\lambda)}{\lambda} \frac{\delta_3}{\delta_n^c} \tag{3.13}$$

$$T_1 = \frac{\partial \Phi}{\partial \delta_1} = \beta \frac{\tau(\lambda)}{\lambda} \frac{\delta_n^c}{\delta_t^c} \frac{\delta_1}{\delta_t^c} \tag{3.14}$$

$$T_2 = \frac{\partial \Phi}{\partial \delta_2} = \beta \frac{\tau(\lambda)}{\lambda} \frac{\delta_n^c}{\delta_t^c} \frac{\delta_2}{\delta_t^c} \tag{3.15}$$

To fully define the bi-linear CCZM, the initial stiffness, k_0, coupled peak traction, τ_p, and critical openings, δ_n^c and δ_t^c, must be defined. This CCZM has an initial elastic response which artificially introduces additional compliance to the sample. To minimize this unwanted artifact, k_0 must be set very high compared to E/h, where E is the Young's modulus of the grains and h is an average grain dimension. However, setting k_0 too high leads to numerical instability. The coupled

peak traction, τ_p, is the strength of the grain boundary. It can be decoupled into the peak normal, T_p^n, and shear, T_p^t, tractions under pure Mode I and pure Mode II according to Eq. 3.16 and 3.17, respectively.

$$T_p^n = \tau_p \tag{3.16}$$

$$T_p^t = \frac{\delta_n^c}{\beta \delta_t^c} \tau_p \tag{3.17}$$

With multiple competing paths for decohesion, even under monotonic loading, some grain boundaries may unload and reload. Under cyclic loading, the grain boundaries will also unload and reload. Therefore, the unloading and reloading behavior to be used with the CCZM must be considered. The behavior used herein is to unload elastically back to the origin and then reload along the unloading path as shown by the dashed line in Figure 3.11. If the CCZM has not previously reached the peak traction and begun to soften, then unloading/reloading retraces the initial elastic portion of the model. Once softening has begun, a new path is created from the location on the softening branch of the model back to the origin, as shown in Eq. 3.18. Reloading retraces this path until reaching the original model. This form of unloading/reloading returns the grain boundary to zero relative opening. Damage is indicated by the lower stiffness of the unloading/reloading path compared to k_0.

$$\text{while } \lambda < \lambda_{max} : \tau = \frac{\tau(\lambda_{max})}{\lambda_{max}} (\lambda - \lambda_{max}) \tag{3.18}$$

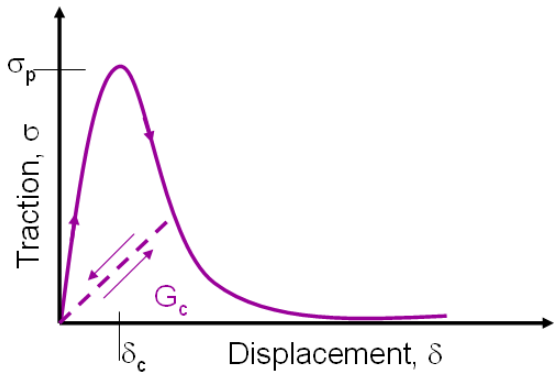

Figure 3.12: Smith and Ferrante exponential coupled cohesive zone model (CCZM).

3.3.3 Exponential Cohesive Zone Model for Grain Boundary Representation

The exponential CCZM of Smith and Ferrante [53], shown in Figure 3.12, also starts from a potential, ϕ.

$$\phi = e\sigma_c\delta_c\left[1 - \left(1 + \frac{\delta}{\delta_c}\right)e^{-\delta/\delta_c}\right] \tag{3.19}$$

where e is the e-number, σ_c is the peak coupled traction, δ_c is a characteristic opening displacement, and δ is the effective opening displacement. In this case, δ_c is not the opening at which cracking occurs, but instead the opening at which the peak traction is reached. The effective opening displacement, δ, is calculated by Eq. 3.20 and is not normalized by the critical opening as λ was for the bi-linear model. Again, the parameter β describes the ratio of shear to normal opening required for nucleation.

$$\delta = \sqrt{\beta^2\left(\delta_1^2 + \delta_2^2\right) + \delta_3^2} \tag{3.20}$$

The coupled traction is the derivative of the potential with respect to δ. Again, the traction can be decoupled by differentiating by each component of δ as shown

in Eq. 3.22 and 3.24.

$$\sigma = \frac{\partial \phi}{\partial \delta} = e\sigma_c \frac{\delta}{\delta_c} e^{-\delta/\delta_c} \tag{3.21}$$

$$\text{Normal: } S_3 = \frac{\delta_3}{\delta} e\sigma_c \frac{\delta}{\delta_c} e^{-\delta/\delta_c} \tag{3.22}$$

$$\text{Shear: } S_1 = \beta^2 \frac{\delta_1}{\delta} e\sigma_c \frac{\delta}{\delta_c} e^{-\delta/\delta_c} \tag{3.23}$$

$$S_2 = \beta^2 \frac{\delta_2}{\delta} e\sigma_c \frac{\delta}{\delta_c} e^{-\delta/\delta_c} \tag{3.24}$$

As long as δ is increasing, the model is loading and follows the equations above. Once δ decreases, unloading must be considered. Again, unloading is done elastically to the origin. Reloading follows the unloading case until rejoining and continuing to follow the curve as shown by the dashed line in Figure 3.12. Eq. 3.25 and 3.26 distinguish loading and unloading where δ_{max} is the maximum δ value reached thus far. Eq. 3.27 shows how σ is calculated under unloading/reloading.

$$\text{loading: } \dot{\delta} \geq 0 \text{ and } \delta \geq \delta_{max} \tag{3.25}$$

$$\text{unloading: } \dot{\delta} < 0 \text{ and } \delta < \delta_{max} \tag{3.26}$$

$$\sigma = \frac{\sigma(\delta_{max})}{\delta_{max}} (\delta - \delta_{max}) \tag{3.27}$$

3.3.4 The Interface Element in 3D and Its Implementation

A convenient method for implementing CCZMs is through a zero-thickness or volume interface element as seen in Figure 3.13. In 2D, a six-noded zero-thickness interface element was inserted between triangles along material interfaces or grain boundaries. The relative normal and shear displacements were calculated along the centerline of the element between pairs of nodes.

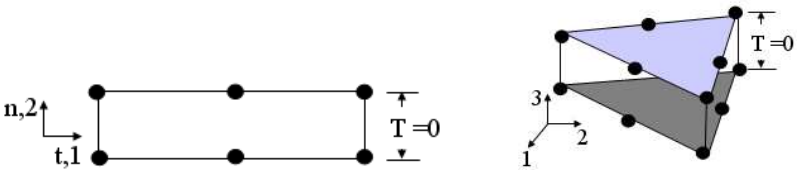

(a) 2D interface element

(b) 3D triangular interface element

Figure 3.13: 2D and 3D triangular interface elements.

This 2D implementation was extended to 3D. For use in tetrahedral element meshes, a triangular interface element was implemented. A similar extension was conducted to generate a quadrilateral interface element for use with brick elements, but is not discussed here. The linear triangular interface element is made up of two 3-noded triangular faces (6-noded for use with quadratic elements). Again, relative displacement is calculated between node pairs at the center plane of the element.

Material state is saved at the gauss points. The constitutive model is also evaluated at the gauss point level. This allows the constitutive models and element formulation to be coded separately. Therefore, the addition of new models and elements may be done easily.

3.4 Parallel Solution

The analysis process can be broken into two phases: element formulation and material state evaluation, and equation solution. The first phase requires element specific formulation and material state evaluation for stiffness and internal force. Element and material routines are contained within FemLib (a library of finite element routines). The additional elements and material models discussed in Section 3.3.4 are implemented within FemLib. FemLib can be used in conjunction with an

equation solver package to complete an analysis.

The equation solution phase is conducted using PETSc, the Portable, Extensible Toolkit for Scientific Computation [50]. PETSc provides optimized serial and parallel solver capabilities. Appropriate function calls are made to FemLib for material state information and element formulations. PETSc also provides options such as solver techniques, fixed and adaptive step controls, and linear and non-linear tolerances. Settings for these options are discussed further in Section 5.5.

3.5 Data Management Using SQL Database

FRANC2D/L, the software used for conducting 2D analyses, utilize files for importing the sample topology and mesh as well as storing intermediate and final results. Internally, data is stored in a relational database structure to facilitate fast data location. The use of a winged-edge database to store mesh and mesh dependent data speeds functionality such as local re-meshing, geometry updating for crack nucleation and propagation, and built-in pre- and post-processing [54, 16, 25].

With the current 3D samples and meshes sizes, data file size and data structure for pre- and post-processing need to be considered. Previously, 2D polycrystal samples were approximately 20,000 DOFs. The family of non-uniform polycrystals considered in Chapter 6 range from 133,098 DOFs for 64 grains to 3,117,048 for 1,000 grains. Storing the meshes as flat files requires 9.9 to 228.9 MB.

To handle the increase in data size and facilitate efficient data extraction, an external *relational database management system* (RDMS) is used [55]. Microsoft SQL Server 2000 [56] is used to manage the current samples. The RDMS serves as a backbone connecting each simulation phase from model creation through post-

processing. SQL Server can handle the large data capacity needed while providing fast and on-the-fly data queries and updating for pre- and post-processing and visualization [57, 58]. SQL provides an interface for executing stored procedures and on-the-fly queries on stored data. A stored procedure is a pre-defined function or procedure that the user has stored with a particular database schema. Given the speed of stored procedures and queries, any information that can be calculated from other stored data is not stored itself. This helps reduce the size of a given database. For example, given the surface mesh of the grains, the location and connectivity of the interface elements can be determined. Therefore, the interface elements do not need to be stored in the database. Specific input files for the solver can be produced with or without the interface elements and results data stored for both instances utilizing a singe database.

Utilizing an RDMS will impact the options for how to visualize the stored data. As discussed next, using SQL in conjunction with OpenDX [59] allows for real-time queries of the database to update the visualization.

3.6 Visualization

Visualization of the polycrystal samples, their surface and volume meshes, and results has been done utilizing OpenDX [59] in conjunction with Python [60] scripts and Microsoft SQL Server 2000 to create the PView tool. OpenDX, originally IBM Visualization Data Explorer, is a visual programming environment used to provide visual representations of data. OpenDX is used to generate an interactive user-interface from which Python scripts are used to compose and execute SQL queries of the appropriate database. This results in real-time query execution and visualization. For a more detailed description of linking OpenDX to SQL Server

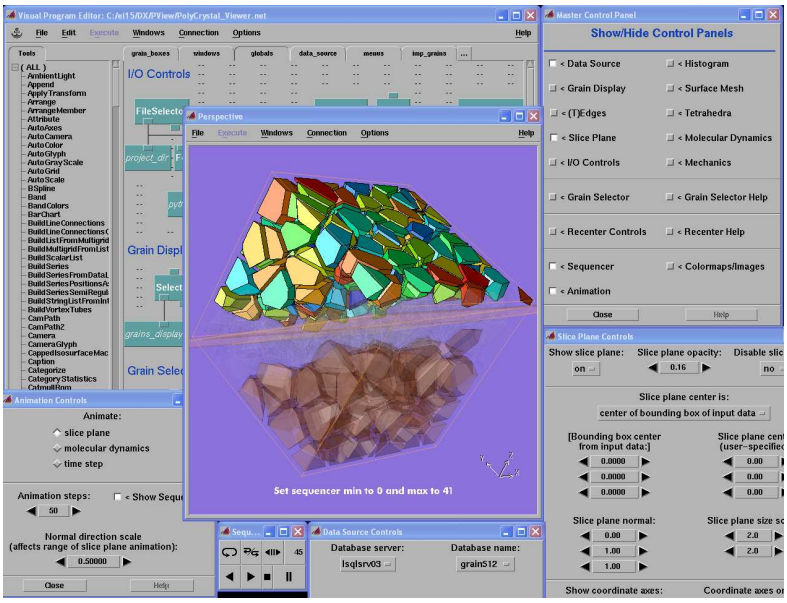

Figure 3.14: PView with OpenDX program and interactive control panels showing geometry inspection.

and the specific visualization options available in PView see Heber, *et al.* [58]. Figures 3.14 through 3.16 show the OpenDX visual program being executed as well as the interactive user control panels and resulting visualization. Inspection of the sample geometry, mesh, and results are available through PView. Figure 3.15 also shows a histogram of surface triangle shape measures, an additional form of data analysis available.

3.7 Summary

A description of methods for generating 3D statistical polycrystal samples is provided, including geometric representation, mesh control, and constitutive models for representing the grain and grain boundary responses. The techniques are adapted from existing 2D implementations. In the case of meshing, the existing 3D implementation is expanded to allow for better control due to the complex internal geometry. To efficiently conduct computational analyses, methods and tools

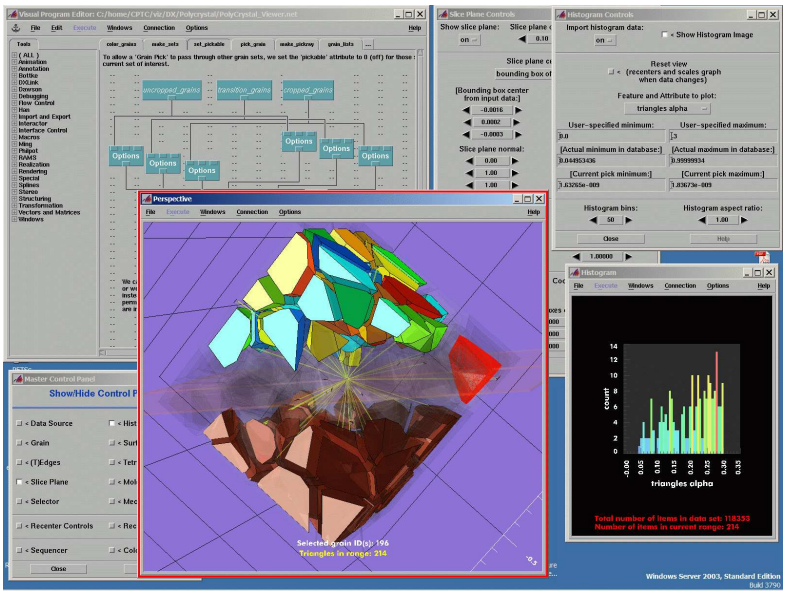

Figure 3.15: PView with OpenDX program and interactive control panels showing surface mesh inspection.

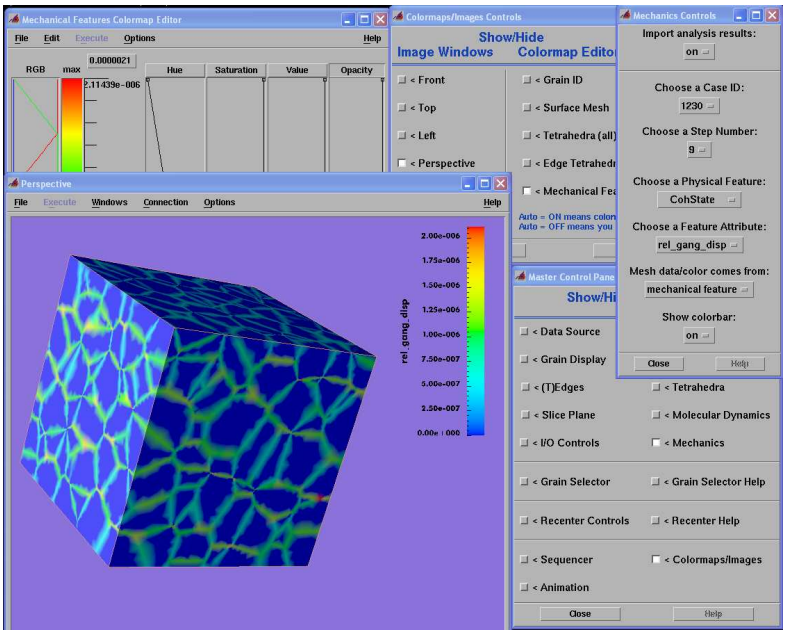

Figure 3.16: PView showing cohesive grain boundary results.

for parallel solution, data management, and visualization are also discussed. The tools discussed here are used to generate, analyze, and visualize 3D polycrystal samples used herein.

Chapter 4

Web Services and Multi-scale Modeling

4.1 Introduction

A polycrystal analysis requires a series of individual actions including generating a geometry, creating a finite element mesh, describing and assigning material properties, conducting an analysis, and post-processing the results. The previous chapter discussed the requirements for these actions. Some actions, such as 3D geometry generation and meshing, are extensions of existing code. However, the existing modified codes are independent from each other. Individual actions, such as meshing a 3D sample with multiple internal regions, are necessary for the current work but are also useful to other researchers. Therefore, a component-based framework is developed for compiling the necessary actions to generate and analyze a polycrystal sample. The alternative is to gather all the required actions into a single monolithic software package requiring re-coding and porting existing software to utilize a single data format, language, and software platform. A component-based framework increases the re-use of existing code while minimizing re-coding and porting. The resulting components may also be utilized by other researchers within the Cornell Fracture Group or collaborators worldwide without using the entire polycrystal generation and analysis process or having to extract the desired section of code to insert it into another software package.

Given the small and transient nature of graduate research groups, packaging, distributing, and maintaining software for collaborators can be burdensome, especially given the diverse platforms being used. Compilation for each system and distributing updates can take time and resources that are not available. There-

fore, to avoid these problems, the polycrystal components are implemented as Web services. Each component has a defined interface and data exchange format. Collaborators can log into a web page or utilize a simple client interface program and access the most up-to-date components running at Cornell. This eliminates the problems of porting and recompiling code for various systems, maintaining different software versions, and notifying collaborators of updates and fixes. Valuable research time and resources can be utilized solving the next research problem rather than porting code between physically distributed collaborators. A more in-depth discussion and example of using Web services to conduct loosely coupled analyses can be found in [61] and [62].

Section 4.2 describes the Polycrystal Generator, a client program designed to guide the user through accessing the components for generating grain geometry, meshing, as well as describing and assigning material properties and boundary conditions. The Polycrystal Generator itself contains no functionality: the client constructs calls to the appropriate Web services based on user input. The communication is submitted across the Internet to the specific Web service which executes the component. The client program is only aware of the defined Web service interface and data exchange format for each component. The data exchange format is defined using XML [63]. Rather than sending large sets of data back across the Internet, resulting data is stored in XML documents within the XMLRepository located at Cornell. The user, using the Polycrystal Generator, can query the stored data, execute other Web services utilizing stored data, and retrieve all or only desired portions of stored data.

Collaborators are able to utilize the current component capabilities via the Web service interfaces. Other researchers have also made their components available for

the current research as Web services. In particular, Overlapping Finite Element and Molecular Dynamics (OFEMD) is a molecular dynamics component which extracts a portion of a finite element mesh to be filled with atoms and analyzed, has been made available by Coffman from the Cornell University Physics Department. Details of OFEMD are available at [64] and [65]. To facilitate multi-scale analyses, the Polycrystal Client includes an interface to the OFEMD Web service.

Details of the Polycrystal Generator are discussed in Section 4.2. Section 4.3 shows an example problem using the Web service components to conduct multi-scale analyses of a particle on a grain boundary. In this example, OFEMD is utilized to produce CCZM input data for a polycrystal-scale model in order to improve the physical fidelity of the polycrystal scale analysis.

4.2 Details of the Polycrystal Generator

The Polycrystal Generator is a client program designed to gather input from a user and execute Web services calls to specific components. It is also capable of submitting and retrieving data to and from the XMLRepository. It does not have any functionality per se, but instead provides a linking between independently created web services. Because there is a defined interface and data format for each Web service, the client program does not need to be updated when the component is modified. This keeps those using the client from worrying about the internal workings of the components.

A snap-shot of the Polycrystal Generator is shown in Figure 4.1. The tabs across the top of the window each represent a component or Web service. The tabs help guide a user through the steps of generating a polycrystal sample for analysis. To begin, the user selects the Geometry Tab shown in Figure 4.1. The

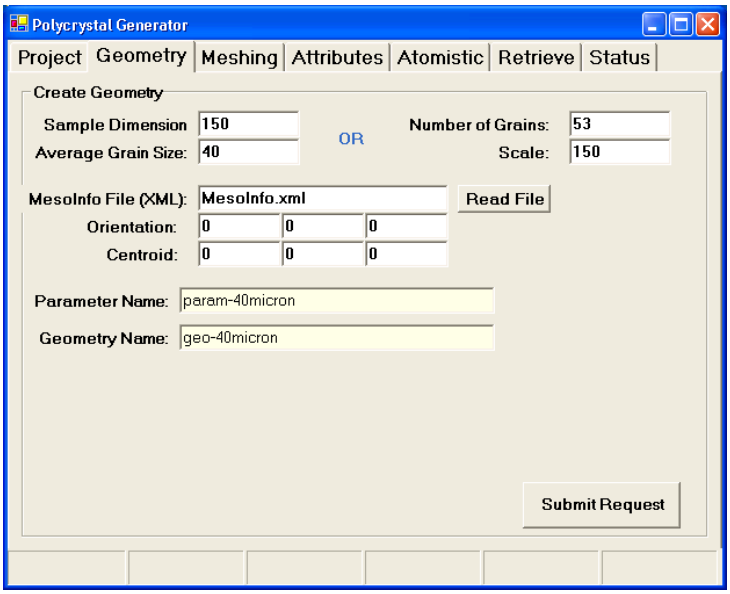

Figure 4.1: Geometry Tab of the Polycrystal Client. This tab collects information for generating a 3D Voronoi grain geometry using the *gen_poly* Web service.

Geometry Tab asks the user for specifics for generating the geometry. The user may enter the number of grains to be generated and the scale of the bounding cube, or the sample dimension and average grain size from which a number of grains is calculated.

Figure 4.2 illustrates what happens behind the scenes after the user clicks "Submit Request." The set of input parameters is placed in an XML document and the document is submitted over the Internet to the XMLRepository. Any XML document in the repository can be queried for specific information or retrieved in whole. When a document is submitted to the XMLRepository it is assigned a UUID, a universal unique identifier. This UUID is returned to the client. Using this UUID, the parameters are retrieved and submitted to the *gen_poly* Web service. *Gen_poly* generates the 3D Voronoi tessellations and returns the geometry in an XML document to the XMLRepository. Again, this submission results in a UUID being produced and returned to the client. A user is unlikely to remember a

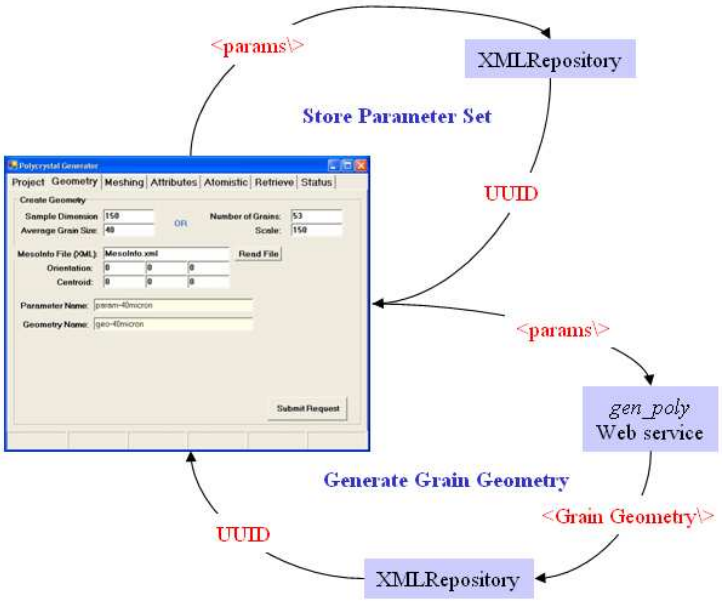

Figure 4.2: Behind the scenes details of the Geometry Tab, including storing the parameter set and then generating the grain geometry. Red text indicates data being transmitted across the Internet. Purple boxes indicate components being used.

randomly generated 128-bit number, the native form of a UUID, so the client allows the user to pair an easier to remember name with each UUID. The client displays this user-specified name while using the UUID behind the scenes. The user specified name or UUID is listed on the Retrieve Tab (Figure 4.3). From this tab the user may retrieve the geometry or any other document from the XMLRepository.

Additional features on the Geometry Tab include applying orientation and location information, as well as immediate retrieval of the geometry. The user may enter coordinates at which to center the polycrystal, other than the origin, and specify an orientation for the cube. This information can also be extracted from an XML document. The user can also elect to have the geometry retrieved automatically from the XMLRepository. The client can store the returned geometry as an XML document or have the client strip off the XML tags.

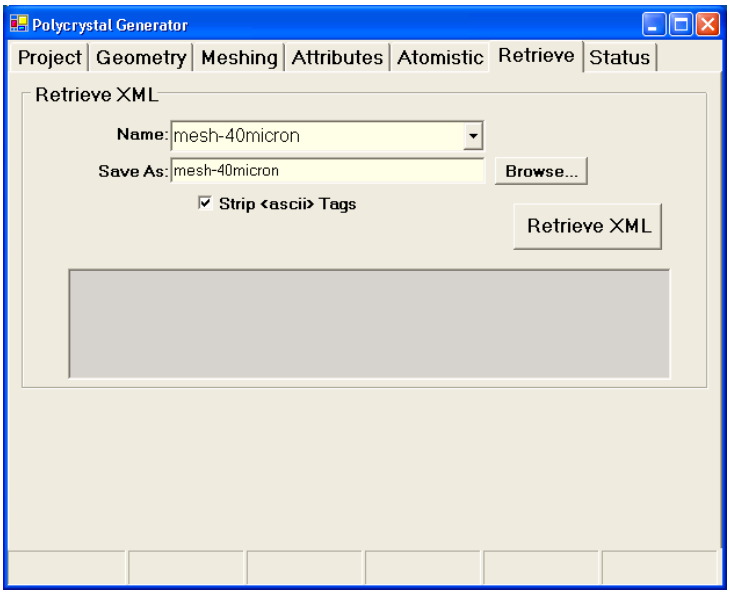

Figure 4.3: Retrieve Tab of the Polycrystal Client. This tab allows the user to retrieve a document from the XMLrepository.

Next, the user can select the Meshing Tab and generate a FE mesh for a geometry. Figure 4.4 shows the Meshing Tab. To begin, the user indicates a geometry to be meshed. Since each component accessed through the Polycrystal Generator is independent of one another, the geometry to be meshed is not required to have been generated using *gen_poly*. As long as the geometry is described in the expected XML format it can be submitted to the meshing component *PolyMesh*. Next, the user may also choose to specify meshing parameters. Default values are used if the user chooses not to specify parameters. When the user clicks "Submit Request" the following actions occur, as shown in Figure 4.5. First, if the geometry resides on the user's local machine or network resource, it is submitted to the XMLRepository and a UUID returned to the client. If the geometry was generated using the Geometry Tab, the geometry is retrieved using the associated UUID. Next, the meshing parameters are expressed in an XML fragment. This fragment and the geometry are submitted to the *PolyMesh* Web service, which generates a mesh as

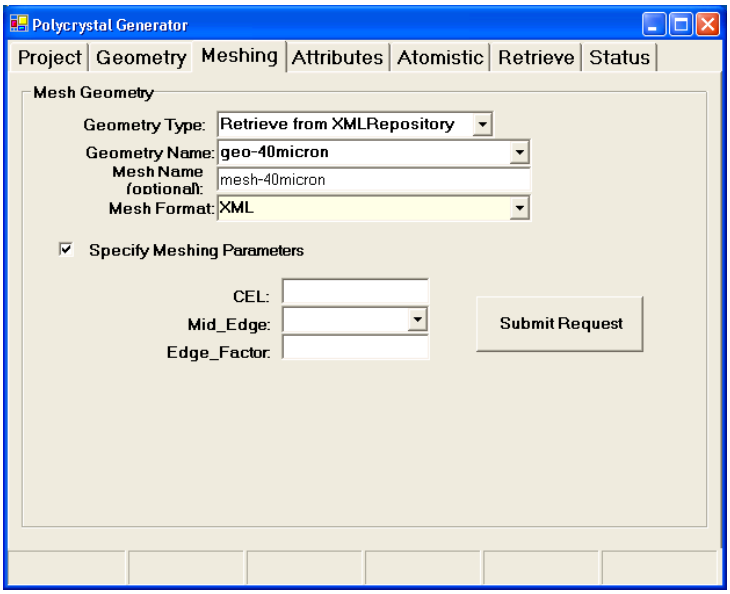

Figure 4.4: Mesh Tab of the Polycrystal Client. This tab collects information for generating a 3D tetrahedral mesh using the PolyMesh Web service.

previously described. The resulting mesh is written out in an XML document. This document is submitted to the XMLRepository and the resulting UUID is returned to the client. Again, the user can select a more memorable name to be paired with the UUID. The geometry and mesh are stored as separate documents within the XMLRepository. Therefore, multiple meshes can be generated for a single geometry. At analysis time, a specific geometry and corresponding FE mesh are selected from the repository.

As mentioned previously, an analysis requires a model to be more than just a geometry and a finite element mesh. It must also include material properties assigned to regions and boundary conditions assigned to finite element entities. This additional information is referred to as *attributes*. The Attributes Tab (Figure 4.6 and 4.7) allows the user to make these additional specifications which are stored in an XML document. This tab has sub-tabs for Grain Material, Grain Boundary Models, and Boundary Conditions, all of which tie to the geometry specified at

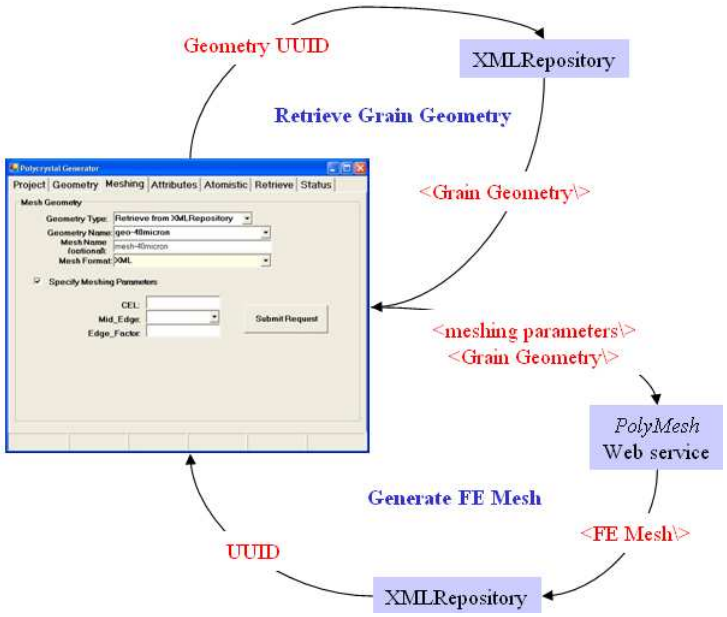

Figure 4.5: Behind the scenes details of the Meshing Tab, including retrieving a stored grain geometry and then generating the mesh. Red text indicates data being transmitted across the Internet. Purple boxes indicate components being used.

the top of the tab. Multiple sets of attributes can be created for each geometry. A single set of attributes is matched with the geometry and mesh at analysis time.

The Grain Material sub-tab (Figure 4.6) lists the different constitutive models available through FemLib to describe the grain response. The user selects one of the material models and then assigns appropriate parameter values. At the polycrystal scale, the sample is no longer homogeneous. It is expected that material parameters and orientations vary from grain to grain. This tab provides different distribution functions to be applied to the parameter values. Each grain is then automatically assigned parameter values from the distribution selected by the user.

The Grain Boundary sub-tab lists the different cohesive zone models available through FemLib to be assigned to the grain boundaries. Again, variation can be introduced to the parameter values from grain boundary to grain boundary. Actual values are selected from the distribution determined by the user and assigned to

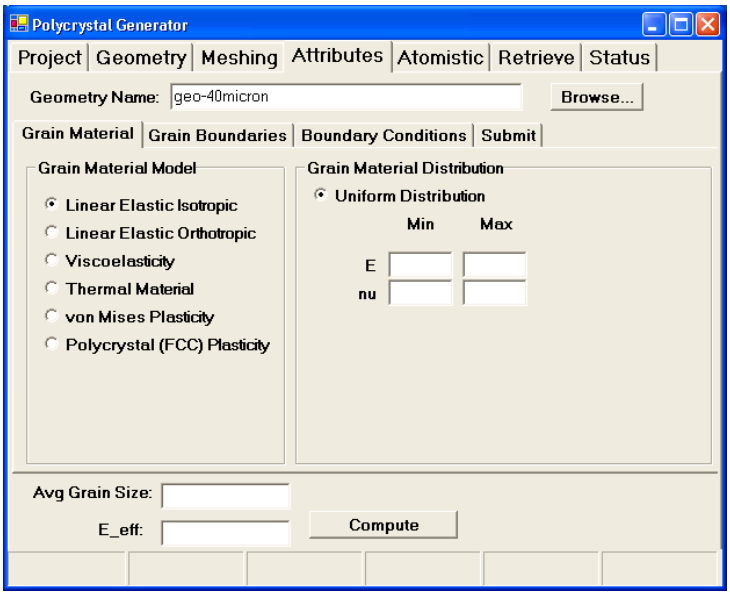

Figure 4.6: Attributes Tab of the Polycrystal Client, grain material sub-tab. This tab allows the user to specify material models and property distributions as well as boundary conditions through a series of sub-tabs.

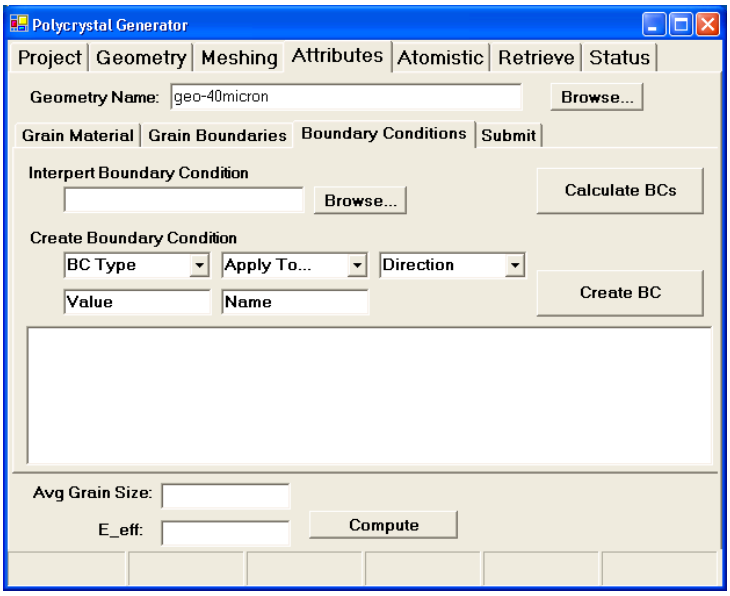

Figure 4.7: Attributes Tab of the Polycrystal Client, boundary conditions sub-tab. This tab allows the user to specify material models and property distributions as well as boundary conditions through a series of sub-tabs.

each grain boundary.

Finally, the Boundary Conditions sub-tab, shown in Figure 4.7, allows the user to specify displacements or tractions to be assigned to the sample. The user selects topological entities (faces, edges, vertices, etc.) for boundary condition assignment, rather than mesh entities. The mesh produced by *PolyMesh* includes a mapping between the topology and the mesh so boundary conditions are automatically transferred to the appropriate mesh entities.

The user may go to the Status Tab, shown in Figure 4.8, at any time while using the Polycrystal Generator. This tab displays any UUIDs, or their corresponding names, that have been generated during the current session. The user can select a specific UUID, or corresponding name, and click on "Status" to check the current status of the UUID. Return values include EXECUTING, SUCCESSFUL, FAILED, or NOT ACTIVE. It can take several minutes to several hours to generate large geometries and meshes. Requests are submitted asynchronously, allowing the client program to be free to continue with other activities while the request is being processed. The Status tab allows the user to check on previous requests.

After creating several XML documents now stored in the XMLRepository, the user may wish to close the Polycrystal Generator. This raises the question of storing the created UUIDs and corresponding names so that the documents may be retrieved later. The Project Tab is used for this purpose (Figure 4.9). While the Polycrystal Generator is open the UUIDs created, the associated type of document (parameter set, geometry, mesh, or attributes) and user specified name are stored internally and displayed on the Project Tab. However, when the Polycrystal Generator is closed this information is lost. The user may chose to store this infor-

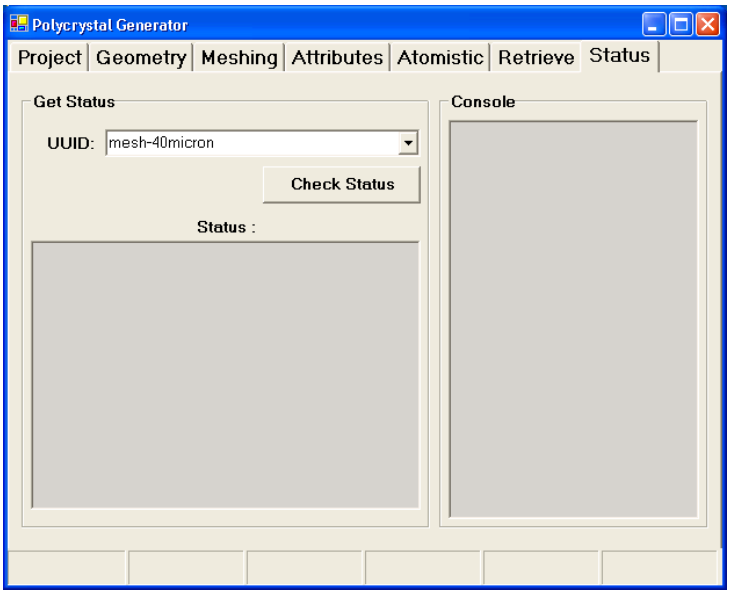

Figure 4.8: Status Tab of the Polycrystal Client. This tab allows the user to check the current status of a request.

mation locally in an XML document at any time. Then, in a subsequent session, the user may load the stored document to retrieve the stored UUIDs.

So far, the Geometry, Meshing, and Attributes Tabs have been described for generating polycrystal samples. The Project and Status Tabs have been discussed for tracking the generated UUIDs and the progress of individual requests. This leaves one last tab in the Polycrystal Generator: the Atomistic Tab (Figure 4.10). This tab is a link to the OFEMD Web service. This component can extract a section of or an entire geometry and corresponding mesh from the XMLRepository. The mesh is filled with atoms and a molecular dynamics (MD) analysis conducted. Most often, a single location within the geometry is selected to be analyzed using MD, due to the large computational effort required. The user may select a geometric feature, such as a section of a grain boundary or triple junction. Then the user chooses to fill a defined region, such as cylinder or sphere, encompassing the specified feature. Additional parameters are defined, and this input information is

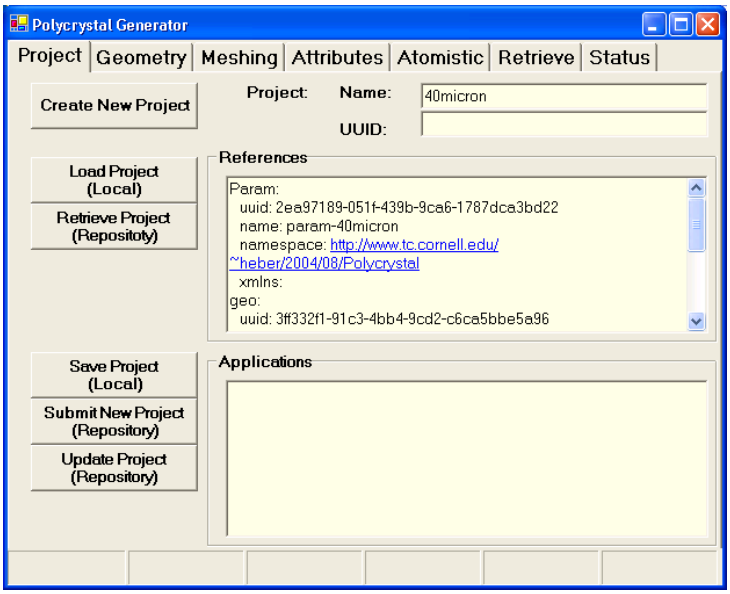

Figure 4.9: Project Tab of the Polycrystal Client. This tab tracks current UUIDs generated by other tabs as well as their type and user specified name.

submitted to the OFEMD Web service. The results of such analyses can be useful for generating and conducting polycrystal-scale finite element analyses. Therefore, this tab is included to encourage the use of this component for atomistic-scale analyses in conjunction with polycrystal-scale analyses. This capability facilitates loosely-coupled multi-scale analyses.

4.3 Multi-scale Modeling: Linking Scales

Focusing on the microstructure scale can give insight into how a material responds and help in discovering and learning to model the underlying physics. However, performing this activity in isolation has limited value and potential. Further, decreasing the length scale in a simulation can expose the underlying physics at play and give insight into the influence and values of modeling parameters. Results and insights gained from the polycrystal scale can be fed to the continuum scale to increase the resolution of the continuum scale analysis and reintroduce the

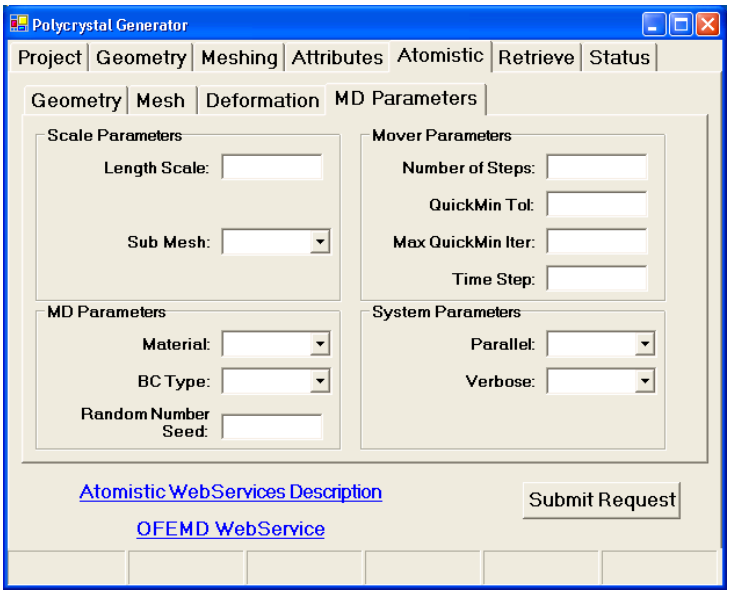

Figure 4.10: Atomistic Tab of the Polycrystal Client. This tab gathers information including which geometry and mesh to retrieve from the XMLRepository to conduct an atomistic simulation.

statistics lost by homogenization.

The approach to multi-scale modeling taken here is *not* to try to introduce the capabilities to analyze all length scales into a single monolithic code. Incorporating continuum mechanics, computational geometry, meshing, parallel solving techniques, and molecular dynamics into a single, integrated code would be a daunting challenge. Capabilities for conducting these tasks are already available within existing software designed by the Cornell Fracture Group or from collaborators. Therefore, a component based framework is adopted. This approach allows for extensive re-use of existing code and the continued development of new or alternative components that can easily be introduced. Given the available components, a user can layout a simulation flow to generate a sample and conduct the desired analysis. Analyses can be done in isolation or in conjunction with analyses at other length scales. For example, as shown previously in Figure 1.5 the results of a continuum scale analysis can indicate the location of interest for generating a

polycrystal sample as well as the boundary conditions to be imposed. The results of the polycrystal analysis can inform the continuum analysis of possible material degradation or crack nucleation. This creates a loosely coupled multi-scale analysis. The following is an example of linking the atomic and polycrystal scales in a multi-scale analysis. Analyses conducted at the atomic scale determine parameters to be used for the CCZM at the polycrystal scale. This coupling increases the physical fidelity of the polycrystal scale analysis by giving a foundation for parameter values not currently available from experimentation.

4.3.1 Linking the Polycrystal and Atomistic Scales

As discussed previously, the Polycrystal Generator components and Web service interface can be utilized to build a multi-scale analysis. The Polycrystal Generator provides a link to an atomistic component, OFEMD, not created by the Cornell Fracture Group, through its Web service interface. The following will demonstrate how a polycrystal-scale sample is generated, extracted and analyzed by OFEMD, and how pertinent information from the atomistic-scale is used as input to the polycrystal-scale analysis. This example will show how using the multi-scale approach can improve the fidelity of higher scale analysis. In this case, the atomistic scale analysis will provide input data that is not currently available through experimentation.

First, a simplified model of a particle on a grain boundary is generated. Figure 4.11 shows the sample of a cubical section of a grain boundary containing a cubical particle. A geometric description of the sample is generated and then submitted to the XMLRepository using the Polycrystal Generator. The geometry is meshed using the Polycrystal Generator and submitted to the XMLRepository. The sample

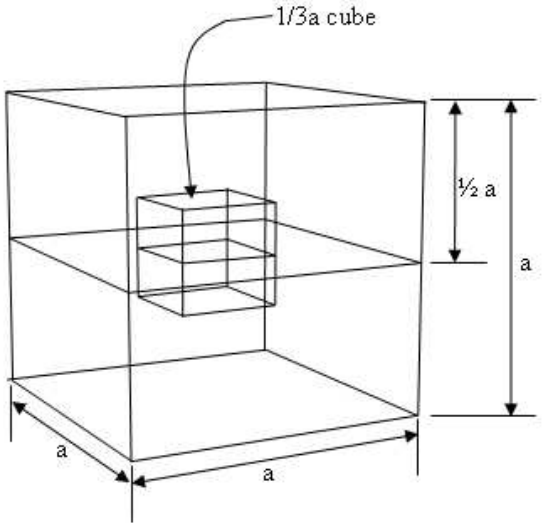

Figure 4.11: Particle on a grain boundary simplified geometry.

geometry is extracted from the XMLRepository by the atomistic component and molecular dynamics (MD) analyses are conducted on the entire sample to observe the sample's overall response and extract grain material properties. Analyses are also conducted on each interface present in the sample, extracting the cohesive response. Finite element grain material models and parameters are determined to approximate the atomistic results. Bi-linear CCZM parameters are determined from the cohesive responses calculated by the MD. Finite element analyses are then conducted and compared to the MD analyses.

MD simulations are carried out on the entire sample to observe the response under loading. The sample geometry is retrieved from the XMLRepository and scaled to a = 30 and 60 $\mathring{A}$. Then each region is assigned an orientation. Finally, the Stillinger-Weber potential is chosen to represent the bulk material. The sample is analyzed three separate times using three variations of the Stillinger-Weber potential for silicon. First, the original form of the potential is used which approximates anisotropic, linear elasticity. Next, the modified Stillinger-Weber is used.

Table 4.1: Elastic Constants from Stillinger-Weber potentials.

Potential	C_{11} (GPa)	C_{12} (GPa)	C_{44} (GPa)
Stillinger-Weber	69.7407	35.1974	51.9968
modified Stillinger-Weber	92.7696	23.687	83.3707
isotropic Stillinger-Weber	116.7793	11.6779	105.1014

This version of the potential approximates orthotropic, linear elasticity. Finally, the Stillinger-Weber potential is further modified to approximate isotropic, linear elasticity. From each analysis the elastic constants can be extracted. Table 4.1 shows the extracted elastic constants. Results from the orthotropic and isotropic versions of Stillinger-Weber are compared to FE results later in this section.

Next, analyses are conducted in which each interface within the sample is modeled to determine the cohesive response. Figure 4.12 identifies all of the interfaces present in the sample. For each interface, an atomic sample, such as seen in Figure 4.13 for Interface 14, is generated. To generate each sample, first the orientations present on each side of the interface are determined. Then, boxes of approximately 60x45x5 $\AA$ are filled with atoms at the determined orientations. Finally, the boxes are joined and an annealing simulation is conducted to produce the lowest energy interfaces. This process produces the MD sample of the interface. Boundary conditions are applied to the outer layer of atoms (the darker atoms in Figure 4.13). The surfaces perpendicular to the grain boundary are constrained to in-plane motion only. The surfaces parallel to the grain boundary are displaced. The traction-displacement relationship is measured at each increment of displacement. The resulting traction-displacement relationships are shown in Figure 4.14. These

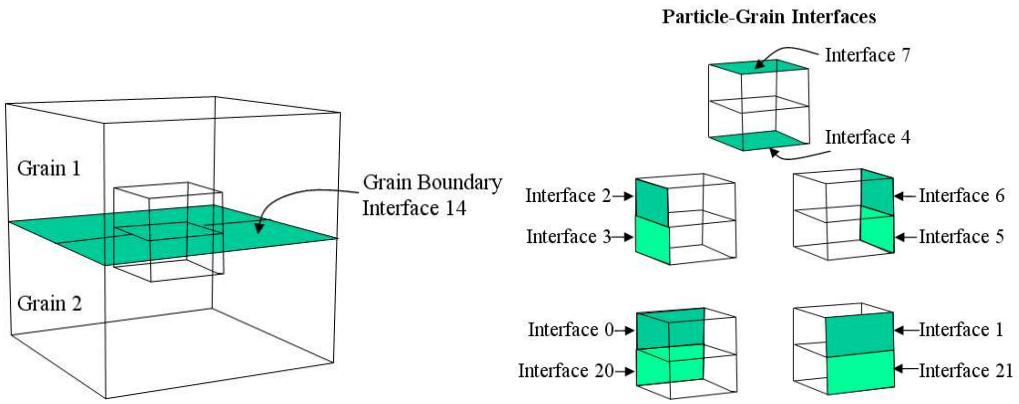

Figure 4.12: Labeled grain boundary and particle-grain interfaces.

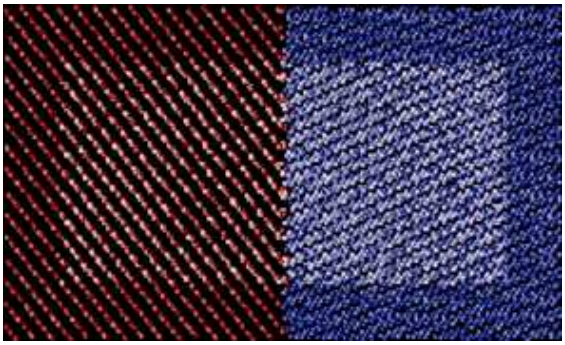

Figure 4.13: Atomic sample of Interface 14.

relationships are approximated by bi-linear curves and used to specify the cohesive zone models for the FE analyses at the polycrystal scale.

FE analyses are conducted using the geometry and finite element mesh stored in the XMLRepository. The grain and interface parameters are determined from the corresponding MD simulation before equivalent FE analyses can be conducted. First, equivalent grain material models and parameters are chosen. As previously mentioned, the results using the modified Stillinger-Weber potential are compared to the FE results using orthotropic, linear elasticity while the isotropic Stillinger-Weber potential is compared to isotropic, linear elasticity. The input form of the material parameters uses Young's modulus and Poisson's ratio rather than the

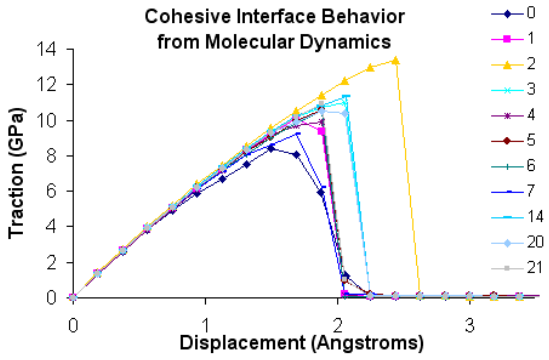

Figure 4.14: Traction-displacement relationships determined through molecular dynamic simulations for each of the 11 interfaces present in the sample using the Isotropic Stillinger-Weber potential.

elastic matrix constants, C_{ii}, extracted from the MD analyses. Equation 4.1 is used to convert the elastic constants to the necessary input parameters. For the isotropic case, Eq. 4.1 becomes Eq. 4.2. E and ν are determined from Eq. 4.3 and 4.4. For the orthotropic case, Eq. 4.1 becomes Eq. 4.5. Silicon has a cubic lattice structure making single crystal silicon isotropic. Therefore, E_1,E_2, and E_3 are set equal to each other as are ν_{12}, ν_{23}, and ν_{13} and G_{12}, G_{23}, and G_{13}. These parameters are calculated using Eq. 4.7 through 4.9 and the elastic constants from the modified Stillinger-Weber potential. Table 4.2 shows the converted parameters used to conduct FE analyses.

$$\sigma = [C]\epsilon \tag{4.1}$$

$$\begin{pmatrix} \sigma_{xx} \\ \sigma_{yy} \\ \sigma_{zz} \\ \sigma_{yz} \\ \sigma_{zx} \\ \sigma_{xy} \end{pmatrix} = \frac{E}{(1+\nu)(1-2\nu)} \begin{bmatrix} 1-\nu & \nu & \nu & 0 & 0 & 0 \\ \nu & 1-\nu & \nu & 0 & 0 & 0 \\ \nu & \nu & 1-\nu & 0 & 0 & 0 \\ 0 & 0 & 0 & 1-2\nu & 0 & 0 \\ 0 & 0 & 0 & 0 & 1-2\nu & 0 \\ 0 & 0 & 0 & 0 & 0 & 1-2\nu \end{bmatrix} \begin{pmatrix} \epsilon_{xx} \\ \epsilon_{yy} \\ \epsilon_{zz} \\ \epsilon_{yz} \\ \epsilon_{zx} \\ \epsilon_{xy} \end{pmatrix} \tag{4.2}$$

$$E = \frac{C_{11}(1+\nu)(1-2\nu)}{(1-\nu)} \tag{4.3}$$

$$\nu = \frac{C_{12}}{(C_{11}+C_{12})} = \frac{(C_{11}-C_{44})}{(2C_{11}-C_{44})} = \frac{C_{12}}{(2C_{12}-C_{44})} \tag{4.4}$$

$$\begin{pmatrix} \sigma_{xx} \\ \sigma_{yy} \\ \sigma_{zz} \\ \sigma_{yz} \\ \sigma_{zx} \\ \sigma_{xy} \end{pmatrix} = \begin{bmatrix} \frac{1-\nu_{yz}\nu_{zy}}{E_yE_z\Delta} & \frac{\nu_{yx}+\nu_{zx}\nu_{yz}}{E_yE_z\Delta} & \frac{\nu_{zx}+\nu_{yx}\nu_{zy}}{E_yE_z\Delta} & 0 & 0 & 0 \\ \frac{\nu_{xy}+\nu_{xz}\nu_{zy}}{E_zE_x\Delta} & \frac{1-\nu_{zx}\nu_{xz}}{E_zE_x\Delta} & \frac{\nu_{zy}+\nu_{zx}\nu_{xy}}{E_zE_x\Delta} & 0 & 0 & 0 \\ \frac{\nu_{xz}+\nu_{xy}\nu_{yz}}{E_xE_y\Delta} & \frac{\nu_{yz}+\nu_{xz}\nu_{yx}}{E_xE_y\Delta} & \frac{1-\nu_{xy}\nu_{yx}}{E_xE_y\Delta} & 0 & 0 & 0 \\ 0 & 0 & 0 & 2G_{yz} & 0 & 0 \\ 0 & 0 & 0 & 0 & 2G_{zx} & 0 \\ 0 & 0 & 0 & 0 & 0 & 12G_{xy} \end{bmatrix} \begin{pmatrix} \epsilon_{xx} \\ \epsilon_{yy} \\ \epsilon_{zz} \\ \epsilon_{yz} \\ \epsilon_{zx} \\ \epsilon_{xy} \end{pmatrix} \tag{4.5}$$

$$\text{where, } \Delta = \frac{1-\nu_{xy}\nu_{yx}-\nu_{yz}\nu_{zy}-\nu_{zx}\nu_{xz}-2\nu_{xy}\nu_{yz}\nu_{zx}}{E_xE_yE_z} \tag{4.6}$$

$$E = \frac{C_{11}(1-3\nu^2-2\nu^3)}{(1-\nu^2)} \tag{4.7}$$

$$\nu = \left(\frac{C_{11}}{C_{12}}+1\right)^{-1} \tag{4.8}$$

$$G = \frac{1}{2}C_{44} \tag{4.9}$$

Next, the cohesive behavior shown in Figure 4.14 is translated to bi-linear cohesive zone laws. For each interface, the maximum traction reached is assigned to the peak traction for each interface and the critical opening is determined to be the opening at which the traction becomes constant under additional displacement. Figure 4.15 shows the cohesive behavior captured by the MD simulation and the corresponding bi-linear CCZM for Interface 14, the grain boundary. Tables 4.3 and 4.4 show the bi-linear CCZM parameters for each interface for the modified and isotropic analyses, respectively.

The cohesive responses shown in Figure 4.14 and resulting CCZMs are visually different than those discussed previously in Chapter 3. The current CCZM exhibit

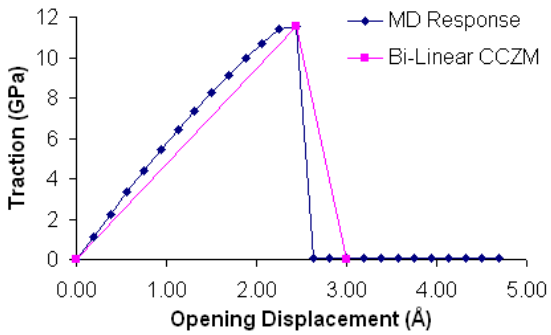

Figure 4.15: Traction-displacement relationships determined through molecular dynamic simulations using the Isotropic Stillinger-Weber potential and the corresponding bi-linear cohesive model generated for Interface 14.

Table 4.2: Grain Material Parameter Values

Isotropic, Linear, Elastic Grain Material		
E		ν
114.656 GPa		0.0909
Orthotropic, Linear, Elastic Grain Material		
E_1,E_2,E_3	ν_{12},ν_{23},ν_{13}	G_{12},G_{23},G_{13}
83.5 GPa	0.2	41.68 GPa

Table 4.3: Bi-Linear CCZM Parameter Values for Orthotropic Grains

Interface	τ_p (GPa)	k_0 (GPa)	δ_n^c,δ_t^c	β
0	9.31	12.08	2.44E-01	1
1	10.6	13.53	2.63E-01	1
2	12.0	13.87	2.82E-01	1
3	12.1	15.55	3.38E-01	1
4	10.4	13.28	2.63E-01	1
5	11.6	13.41	2.82E-01	1
6	10.6	13.29	2.82E-01	1
7	11.1	13.91	2.82E-01	1
14	11.5	13.29	2.82E-01	1
20	11.8	15.43	3.19E-01	1
21	11.6	14.26	3.00E-01	1

Table 4.4: Bi-Linear CCZM Parameter Values for Isotropic Grains

Interface	τ_p (GPa)	k_0 (GPa)	δ_n^c,δ_t^c ($\mathring{A}$)	β
0	8.33	13.62	2.44E-01	1
1	10.1	13.45	2.25E-01	1
2	13.4	15.49	2.82E-01	1
3	11.0	13.03	2.44E-01	1
4	9.93	12.89	2.44E-01	1
5	10.6	13.76	2.44E-01	1
6	10.5	12.57	2.25E-01	1
7	9.25	13.36	2.44E-01	1
14	11.3	13.39	2.44E-01	1
20	10.5	13.63	2.44E-01	1
21	10.9	14.15	2.44E-01	1

a shallower initial slope and steep softening branch. The steeper and therefore shorter softening branch is indicative of brittle failure, which is expected in silicon. The shallower initial slope results in the value of k_0 being only slightly higher than E/h for the neighboring grains. The grain property values extracted from the MD simulations result in E/h values of 7.66 GPa/AA and 5.56 GPa/AA for isotropic and orthotropic grains respectively using an h of 15 AA. These values are only slightly higher than the k_0 values reported in Tables 4.4 and 4.3. The higher value of k_0 with respect to E/h allows the overall elastic response of the sample to mainly come from the grains rather than the elastic opening of the grain boundaries. However, the cohesive responses extracted from the atomic models do incorporate a portion of the sample's overall elastic response. Therefore, the CCZM used for this example has a lower *stiffness* and more brittle response than discussed previously.

FE analyses are conducted for the sample scaled to 30 and 60 $\mathring{A}$ using the material parameters determined above. The boundary conditions applied for the FE analyses are shown in Figure 4.16. Both the MD and FE analyses are strained to 30%.

4.3.2 Modified Stillinger-Weber versus Orthotropic, Linear Elastic FE

Figure 4.17 shows snap-shots of the MD analysis for 30 AA sample. The atomic sample is initially annealed to relax the interfaces to the lowest energy state before straining to 30%. The color of each atom indicates the displacement away from its natural lattice position. Blue indicates the natural lattice position while red indicates the farthest displacement. In Figure 4.17a the interfaces present are

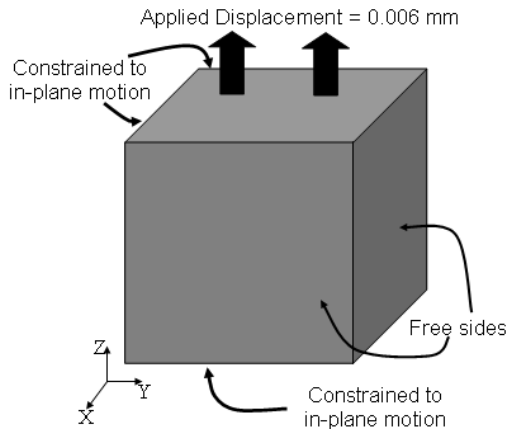

Figure 4.16: Simple tension boundary conditions.

highlighted by the non-blue atoms. The non-blue atoms at 0% strain indicate the displaced atoms along the interfaces. The first 20% strain results in the sample stretching. At 25% strain the grain boundary is breaking. The left side of the sample has not completely separated while the blue atoms to the right of the particle indicate that separation has occurred allowing the atoms on either side of the grain boundary to relax to their natural positions. By 30% strain the entire grain boundary has separated and the particle has cracked through the center. The orientations of the two grains do not form a perfect interface; therefore, the boundary is not necessarily symmetric and does not separate uniformly. The specific placement of the particle along the interface also attributes to the lack of symmetry.

The orthotropic, linear elastic FE analysis uses the grain material parameters and cohesive parameters extracted from MD simulations described previously. Figure 4.18 shows the relative opening of the interfaces in the loading direction. A slight variation in the color contour is seen across the grain boundary. This variation corresponds to the non-uniform separation seen in the MD analysis. Figure

4.19 shows the corresponding displaced shape of the FE model. The displaced shape shows a slight bowing of the grain boundary near the edge of the sample, again indicating that the surface does not separate uniformly. The sides of the particle also bow, indicating some separation of the particle from the grains near the grain boundary.

The MD and FE analyses show qualitative agreement in how the interfaces open. However, the results quantitatively disagree with respect to the amount of separation along the grain boundary. By 30% strain the MD simulation has formed a through crack while the maximum λ value in the FE simulation is only 0.61. A value of $\lambda \geq 1.0$ is needed to indicate full separation of the interface. The cohesive responses determined by the MD analyses all showed brittle responses. This is seen by the steep softening portions of the cohesive responses shown in Figure 4.14. As seen in Figure 4.15, converting the cohesive response extracted from the MD simulation to a bi-linear CCZM results in slight lowering of k_0 and a less brittle softening response. These discrepancies may account for some of the differences seen in the opening response of the grain boundary. The FE model also does not include interface elements along the centerline of the particle. Therefore, cracking of the particle is not included. This likely also hinders the opening of the grain boundary.

4.3.3 Isotropic Stillinger-Weber versus Isotropic, Linear Elastic FE

Again, MD and FE analyses are conducted, straining the sample to 30%. For this comparison the MD analysis utilizes the isotropic Stillinger-Weber potential. The FE analysis utilizes isotropic, linear elastic parameters and the CCZM parameters

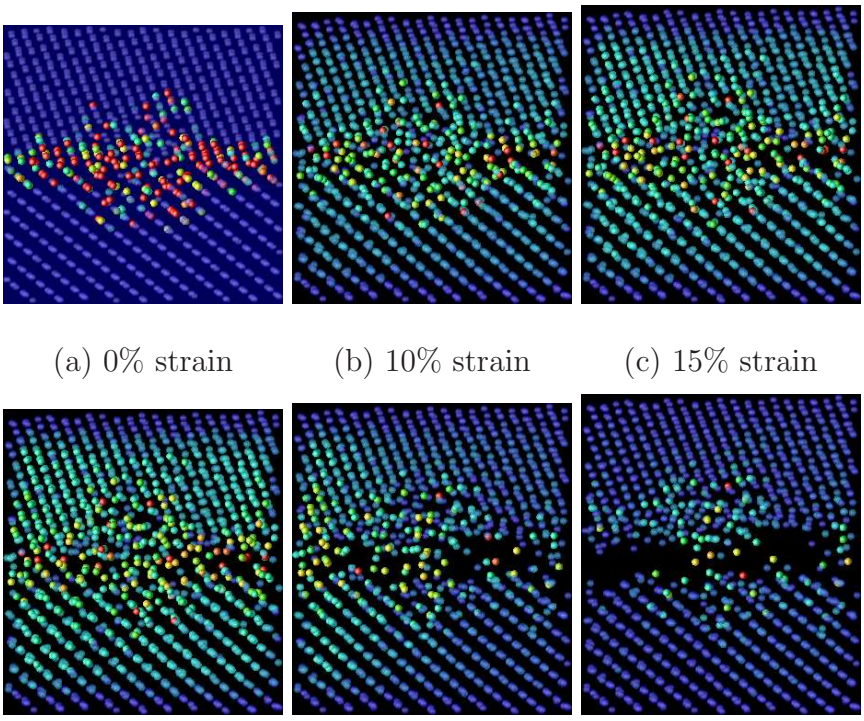

(a) 0% strain (b) 10% strain (c) 15% strain

(d) 20% strain (e) 25% strain (f) 30% strain

Figure 4.17: MD results for the 30 $\mathring{A}$ sample using the modified Stillinger-Weber potential.

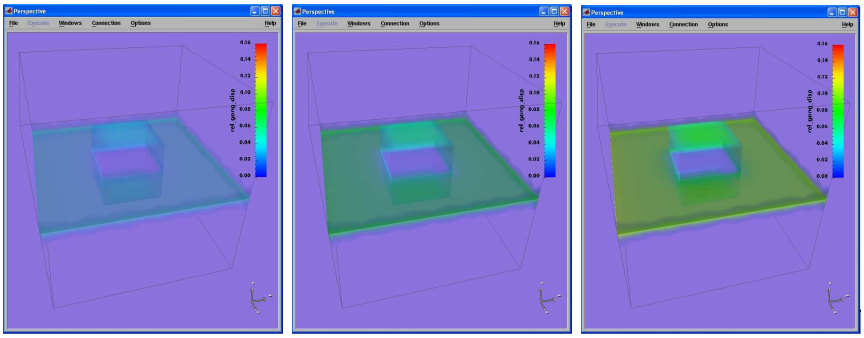

(a) 10% strain (b) 15% strain (c) 20% strain

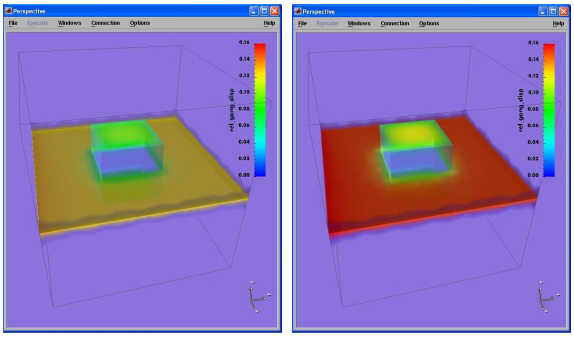

(d) 25% strain (e) 30% strain

Figure 4.18: Interface opening in the loading direction for the 30 $\mathring{A}$ FE analysis with orthotropic, linear elasticity.

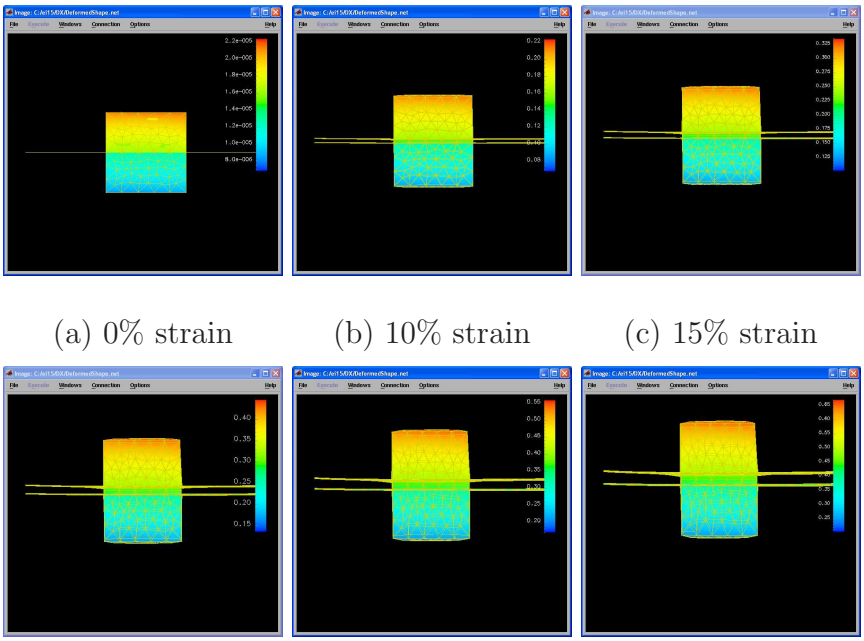

(a) 0% strain (b) 10% strain (c) 15% strain

(d) 20% strain (e) 25% strain (f) 30% strain

Figure 4.19: Deformed shape for the 30 $\mathring{A}$ FE analysis with orthotropic, linear elasticity.

corresponding to the MD analyses of the interfaces using the isotropic potential.

Figure 4.20 shows snap-shots of the MD analysis of the 30 $\mathring{A}$ sample. As seen previously, the MD analysis shows non-symmetric and non-uniform separation of the grain boundary. Full separation of the grain boundary and cracking of the particle is reached sooner than with the modified Stillinger-Weber potential.

Figure 4.21 shows the relative opening of the interfaces in the loading direction from the FE analysis using linear, elastic isotropic grains and corresponding CCZMs. This analysis does not result in the color contour variation seen across the grain boundary for orthotropic, linear elasticity. The isotropic, linear elastic FE model does not account for grain orientation. Therefore, the FE analysis is modeling perfect interfaces which are not present in the atomic sample. The perfect grain boundary interface being modeled by the FE material model should separate

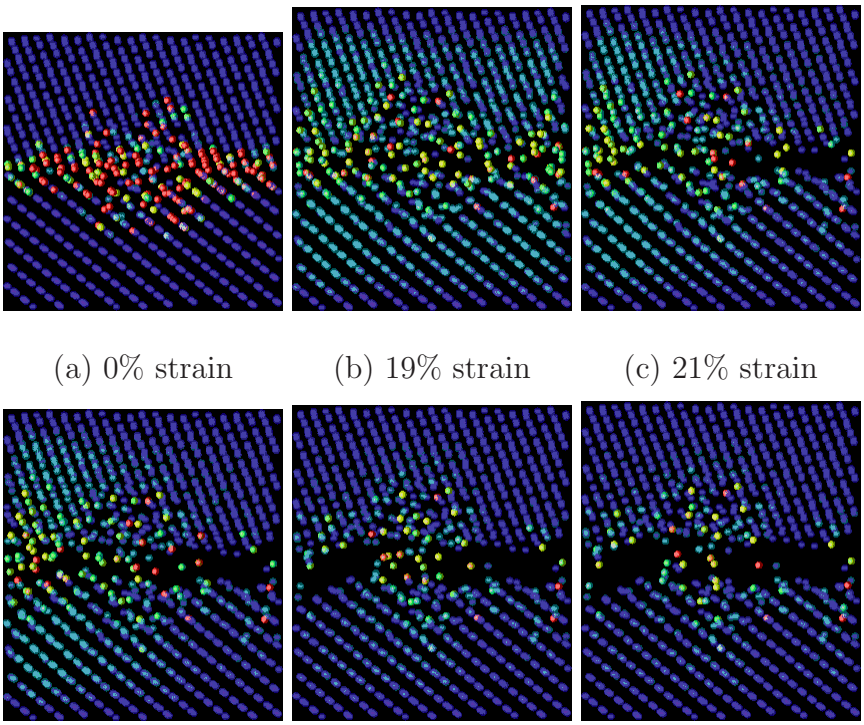

(a) 0% strain (b) 19% strain (c) 21% strain

(d) 25% strain (e) 27% strain (f) 30% strain

Figure 4.20: MD results for the 30 $\mathring{A}$ sample using the isotropic Stillinger-Weber potential.

uniformly across the interface with variation only present where the grain boundary intersects the particle. This result indicates that the orthotropic, linear elastic model is more appropriate for the given sample. Figure 4.22 also does not show the bowing for the corresponding displaced shape. Instead, the grain boundary only pinches shut slightly where the grain boundary intersects the particle.

The maximum λ value seen for this analysis is 0.7, which is higher than that seen in the previous analysis. However, it again is lower than the full separation seen by the MD analysis. Again, not allowing the particle to crack as seen in the MD analysis contributes to the lower opening.

The above analyses utilized the multi-scale framework to conduct higher fidelity FE polycrystal analyses. The results of the modified and isotropic Stillinger-Weber

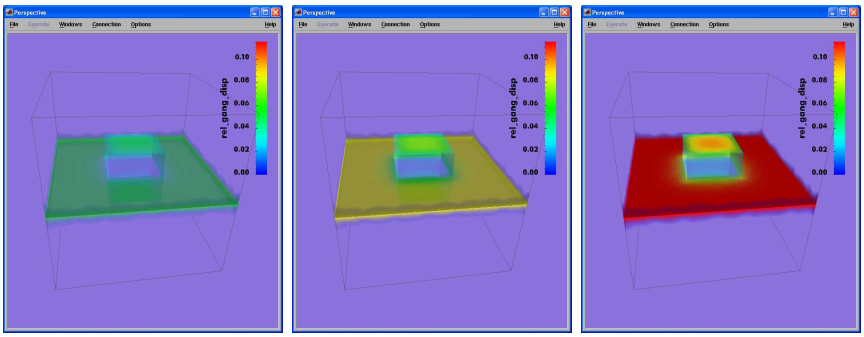

(a) 10% strain (b) 19% strain (c) 20% strain

Figure 4.21: Interface opening in the loading direction for the 30 $\mathring{A}$ FE analysis with isotropic, linear elasticity.

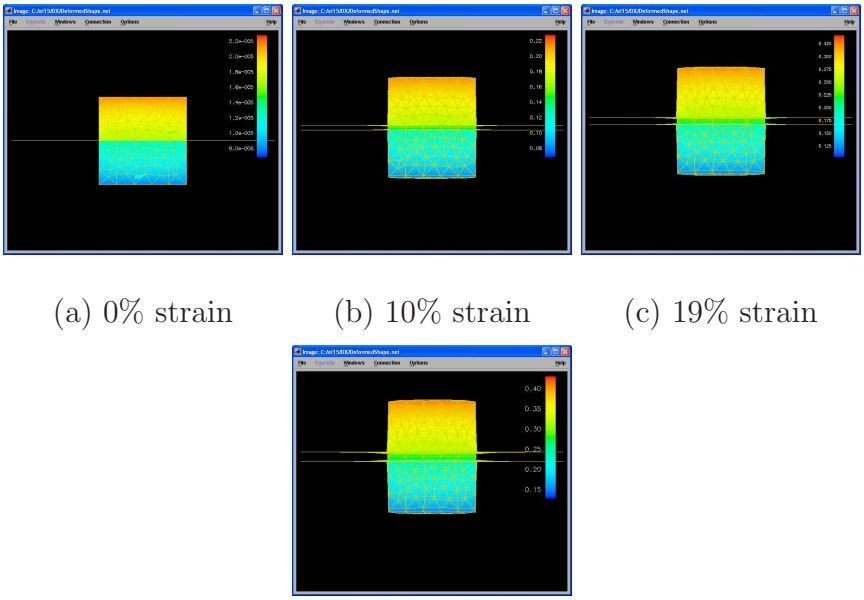

(a) 0% strain (b) 10% strain (c) 19% strain

(d) 20% strain

Figure 4.22: Deformed shape for the 30 $\mathring{A}$ FE analysis with isotropic, linear elasticity.

potentials where also compared to the orthotropic and isotropic, linear elastic FE analyses, respectively. The orthotropic, linear elastic FE analysis was determined to be more appropriate for the given sample being analyzed. The MD analyses of the interfaces present in the sample increased the fidelity of the FE results. Variation in the CCZM parameters from interface to interface was determined by the MD analyses. In previous polycrystal analyses conducted by this author, cohesive parameters were randomly selected from a uniform distribution of values. Parameter variation was not based on the specific orientation mis-match across an interface. The mean values of the uniform distributions were varied without any connection to the true mean interface properties for a given material.

4.4 Summary

The polycrystal components discussed in this chapter will be used to generate samples and conduct analyses herein. Individual components accessed through the Polycrystal Generator can also be utilized for other purposes or be replaced with new or alternative options. The Web service interface implemented allows for simplified collaboration with other researchers. As shown, data generated by the Polycrystal Generator and stored in the XMLRepository is able to be utilized by outside components and researchers. This interaction can lead to the building of multi-scale analyses. The analyses shown demonstrate how different scales can interact and be used to enhance each other.

Parameters for CCZMs can not currently be obtained experimentally at the grain scale. However, as shown by example, information gathered at the atomic-scale can be used by FE analysis to study grain boundary behavior. The polycrystal analyses discussed can in turn be utilized by continuum-scale models.

Chapter 5

Verification using 3D Polycrystals with Regular Grains

A common technique employed when trying to incorporate lower length scale responses and information into larger scale analyses is the use of a *representative volume element*, RVE. An RVE is assumed to be a minimum volume of material that is large enough to reliably capture key physics occurring at the current scale. Often, this volume is assumed to repeat in all directions infinitely creating a periodic structure, thus modeling an entire body while representing only a small fraction of its volume. An RVE can be used whether it is directly embedded within a larger scale analysis or is being used to infer information from a lower length scale.

Important properties may not be captured if too small of a sample is analyzed. Any conclusions drawn from such an analysis may not be accurate. Also, the boundary conditions applied to the sample will affect the internal response. Therefore, it is important to model and analyze a large enough volume to leave a central portion of the sample unaffected by boundary effects. These considerations lead to the following questions:

1. What is the minimum size of an RVE of an aluminum-like material without inclusions?

2. What is the largest sample that can be analyzed before becoming computationally intractable?

The answer to question 1 will determine the interpretation of question 2. If the minimum size of the RVE is small, then we want to know how large an analysis can

be conducted. Large can indicate a larger sample size or more complexity within the same sample size resulting in a larger computation. If the minimum size is very large, we want to know if we can indeed analyze a single RVE.

To answer these questions, a series of numerical experiments are conducted, beginning with a family of polycrystals with regular grains. Using these samples, the constitutive model implementations are verified, appropriate modeling and algorithmic parameters are determined, and the influence that variation in grain material properties, texture, and boundary conditions have on the global response is evaluated. Based on the results of this study, a family of Voronoi grain geometries is generated and used in Chapter 6 to further investigate the change in global response due to grain geometry and internal material variation. Results from both studies are used to answer questions 1 and 2, above.

5.1 Constitutive Model Verification using Polycrystals with Cubical Grains

A family of polycrystal samples consisting of 0.05 mm cubical grains is used to verify the polycrystal response. 0.05 mm is an average grain dimension experimentally observed in samples of AA 7075. Samples referenced herein include 64, 216, 512, and 1000 cubical grains (Figure 5.1). For each sample, the grain size remains constant, thus increasing the overall size of the sample as the number of grains increases. The overall dimensions of the samples are 0.2, 0.3, 0.4, and 0.5 mm on a side, respectively.

Samples without cohesive grain boundaries are analyzed to verify expected results using different material models, determine optimal computational solution

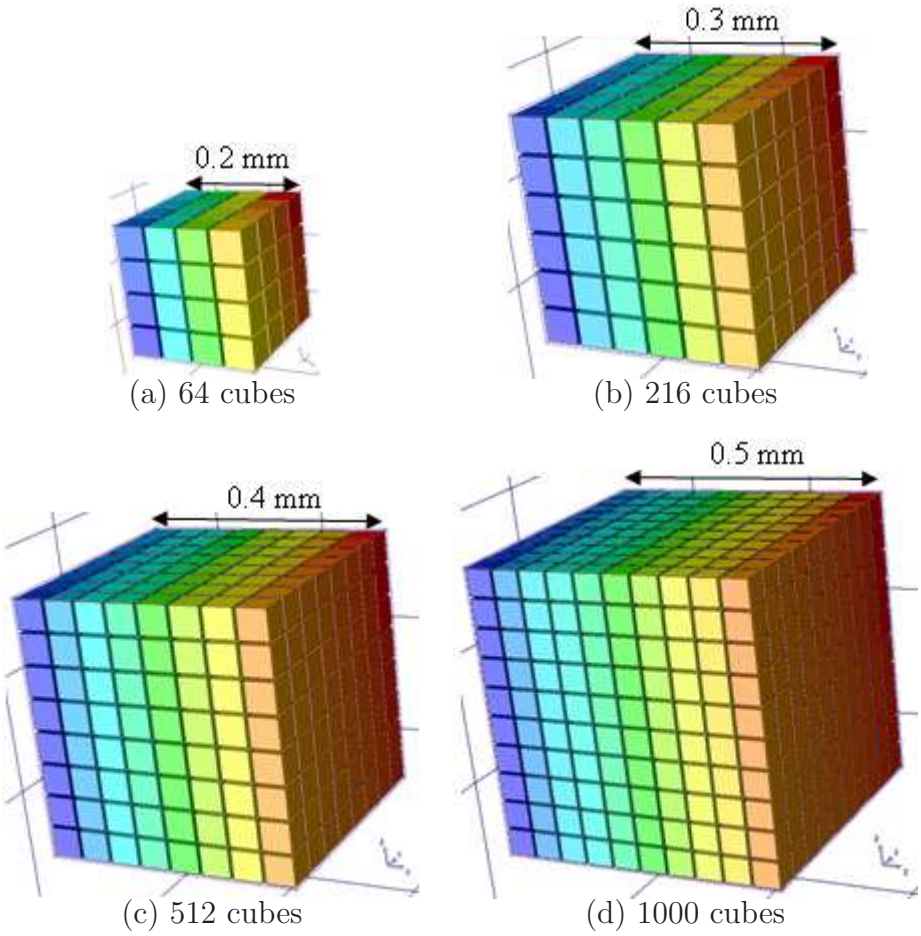

(a) 64 cubes (b) 216 cubes

(c) 512 cubes (d) 1000 cubes

Figure 5.1: Regular polycrystal samples using 50 μm cubical grains.

parameters, and investigate self-consistency. Next, cohesive grain boundaries are placed between all grains. These samples are used to verify the cohesive zone model and interface element implementations as well as investigate the influence of the presence of cohesive zones on mesh convergence, determine appropriate optimal computational solution parameters, and check for self-consistency. The response of each sample is compared to an analytic solution where applicable.

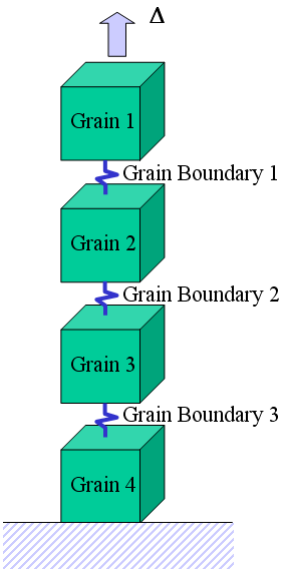

Figure 5.2: Simplified model of grains and grain boundaries as a series of elastic blocks and springs.

5.2 Verification Problem Definition

Verification of the polycrystal's response is based on simplifying the problem to a series of columns of elastic blocks connected by springs, as shown in Figure 5.2, and subjected to an applied displacement. A column can be made as high as the height of the numerical sample and repeated to recreate the cubical grain sample. Each block is assigned the same Young's modulus, E_{gr}, as the corresponding grain. The initial height of the grains/blocks is represented by L. The springs connecting the blocks are given the same stiffness, k, and peak traction, τ_p, as the corresponding grain boundaries. As long as the grains and grain boundaries remain linear elastic, the stress and displacement of the column can be calculated analytically. The total displacement, Δ, is the summation of the elongation of the grains and of the opening of the grain boundaries (Eq. 5.1). Assuming that all grains and grain boundaries have the same respective properties, the stress in the column will be constant (Eq. 5.2) under applied displacement boundary conditions. Given the

stress in the blocks, σ_{gr}, and the stress in the springs, τ_{gb}, the elongation of the grains, δ_{gr}, and opening of the grain boundaries, δ_{gb}, is calculated using Eq. 5.3 and 5.4. The elongation in terms of the stress is then substituted into Eq. 5.1 resulting in Eq. 5.5.

$$\Delta = \sum_i \delta_{gr}^{(i)} + \sum_j \delta_{gb}^{(j)} \tag{5.1}$$

$$\sigma = \sigma_{gr}^{(1)} = \sigma_{gr}^{(2)} = \sigma_{gr}^{(i)} = \tau_{gb}^{(1)} = \tau_{gb}^{(j)} \tag{5.2}$$

$$\delta_{gr}^{(i)} = \frac{PL}{AE_{gr}^{(i)}} = \frac{\sigma L}{E_{gr}^{(i)}} \tag{5.3}$$

$$\delta_{gb}^{(j)} = \frac{\tau_{gb}^{(j)}}{k^{(j)}} = \frac{\sigma}{k^{(j)}} \tag{5.4}$$

$$\Delta = \sum_i \frac{\sigma L}{E^{(i)}} + \sum_j \frac{\sigma}{k^{(j)}} \tag{5.5}$$

As long as the blocks and springs remain linear elastic, the load versus displacement, or response, curve is calculated using the above equations. However, once the springs reach their peak traction they soften, resulting in a non-linear problem. To continue tracking the softening portion of the response curve, the above calculation is carried out by incrementally increasing the spring opening and using the resulting traction to determine the total elongation in the blocks. Given that the springs have reached their peak traction, the stress in the column reduces. Thus the blocks begin to contract. Given that the stress in the column is a constant, all of the springs want to continue to open the same amount. While it is possible to continue this analysis by hand, this is a numerically unstable situation. Once the peak traction of the springs is reached, the numerical solver has difficultly tracking the globally softening behavior with all grain boundaries softening simultaneously. To stabilize the analysis, the center spring is weakened slightly by reducing its peak traction by 2%. This causes the center spring to soften before the other springs, thus concentrating the opening to a single spring. As the weakened spring softens,

Table 5.1: Grain Material and Grain Boundary Property Values

Linear, Elastic Isotropic Grain Material				
E			ν	
75,600 MPa			0.0	
Bi-Linear CCZM				
k_0	τ_p	δ_n^c	δ_t^c	β
22.5 GPa	450 MPa	0.005 mm	0.005 mm	1.0

the other springs and blocks contract accordingly. The column still softens but in a manner that the solver can track.

The grains and grain boundaries are assigned the linear, elastic isotropic grain properties and bi-linear coupled cohesive zone model (CCZM) properties shown in Table 5.1. Grain property values are based on the bulk properties of AA 7075. The analytic solution does not consider the response of the column in transverse directions. Therefore, to match the analytic solution as closely as possible the grains are assigned a Poisson's ratio of 0.0. The center four grain boundaries on the center plane of each sample are assigned a peak traction of 441 MPa, 98% of the peak traction,τ_p, assigned to the other grain boundaries (Figure 5.3). The samples are loaded in uniaxial tension, as shown in Figure 5.4, to an applied displacement of 0.006 mm or 3% strain for the 64 cubical grain sample. This displacement is greater than the critical normal displacement, δ_n^c, and therefore is enough to cause softening and failure due to a through crack along the center plane of the sample. Failure is noted by zero load being carried by the sample.

This analysis utilizes the adaptive step control feature within the PETSc solver. This feature automatically increases/decreases the step size to aid in convergence.

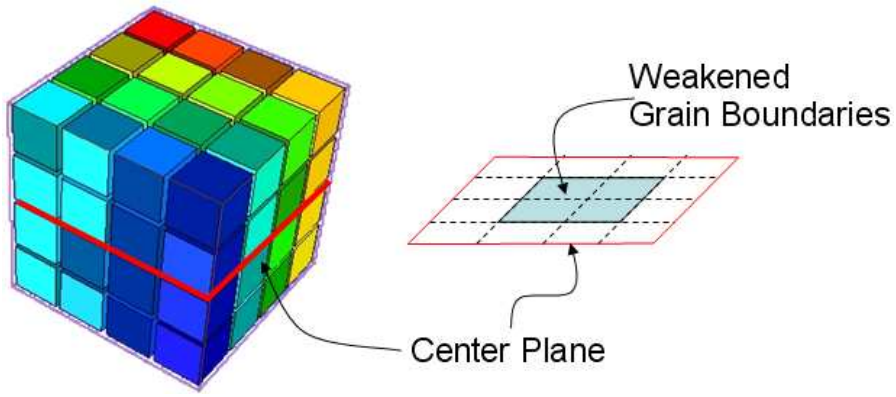

Figure 5.3: Weakened grain boundaries in the middle of the center plane of sample.

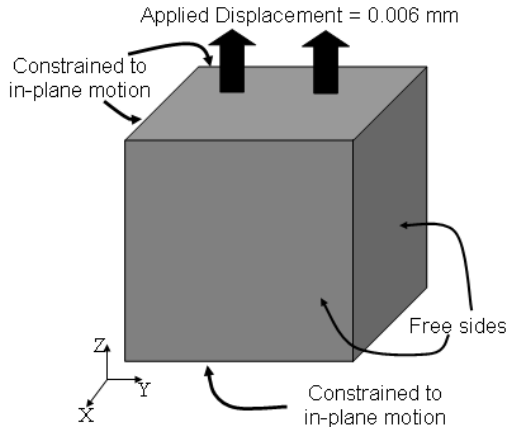

Figure 5.4: Simple tension boundary conditions.

If four steps in a row converge in less than four Newton iterations, the step size is increased. If a step takes more than 32 iterations to converge, the size of the next step is decreased. If a step does not converge, the step size is decreased and retried. After four consecutive step size reductions without convergence, the analysis is terminated. The user may specify the maximum step size to be used, which the adaptive step controller cannot exceed, as well as the size of the first step taken.

For the current analyses, the maximum step size is set to 0.005 μm. The method used to determine this maximum step size is discussed in Section 5.5. Due

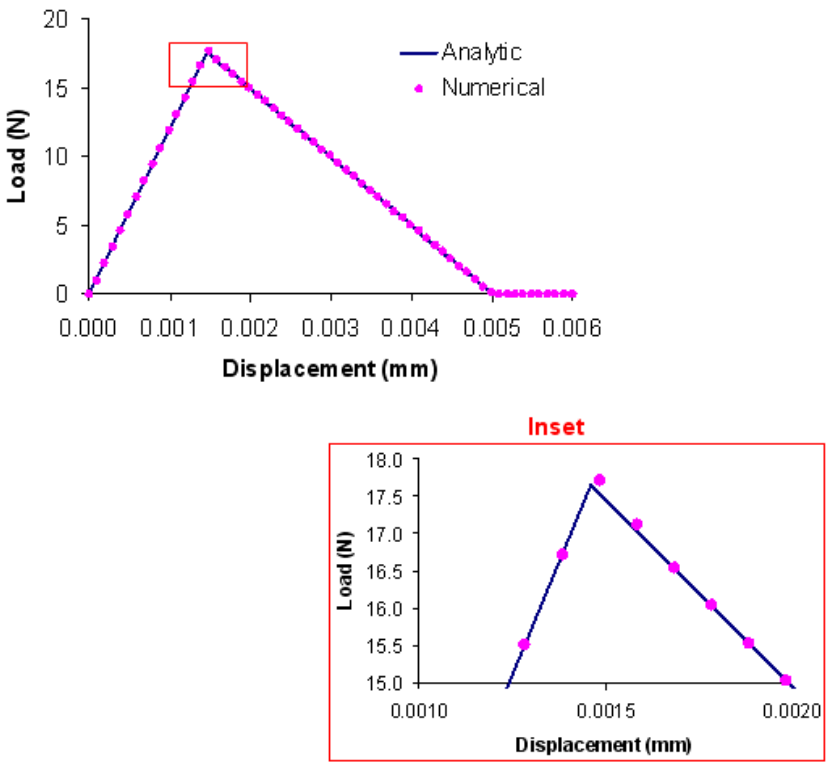

Figure 5.5: Analytic and numeric displacement versus load curves for the 64 cubical grain sample under uniaxial tension.

to the global softening expected, the *trust region* technique is used instead of the default *line search* technique. Figure 5.5 shows the numerical and corresponding analytic solution for the 64 cubical grain models. Results for the larger samples are discussed in Section 5.7.

The numerical results for the 64 cubical grain sample closely match the analytic solution (Figure 5.5). Minor deviation of 0.37% is seen at the peak of the response curve as the solver tries to follow the sharp change in global stiffness. The number of Newton iterations required for convergence increases the onset of global softening, due to the solution becoming non-linear. This non-linearity becomes more pronounced as the sample size increases.

5.3 Effects of Mesh Refinement on Verification

The influence of mesh refinement on the accuracy of the numerical solution as it pertains to capturing the cohesive response is investigated. To capture correctly the cohesive response, the size of the elements in the cohesive zone should be below the *intrinsic cohesive length*. The intrinsic cohesive length, Δ_{int}, is computed according to Eq. 5.6 [66, 67], where E is the Young's modulus of the grains, τ_p is the peak traction of the CCZM, and ϕ corresponds to the energy of fracture. For the bi-linear CCZM, ϕ is determined by Eq. 5.7. With the properties shown in Table 5.1, $\Delta_{int} = 0.164$ mm.

$$\Delta_{int} = \frac{\pi \phi E}{8\tau_p^2} \tag{5.6}$$

$$\phi = \frac{1}{2}\tau_p \delta_c \tag{5.7}$$

For the 64 cubical grain sample, a coarse and fine mesh is investigated. The coarse mesh is generated using a global characteristic element length, CEL (Section 3.2.2), of 0.025 mm, half the edge length of a grain. The fine mesh's global CEL corresponds to one third the grain edge length or 0.0166 mm. Both mesh models are shown in Figure 5.6. The global CEL determines the largest edge sub-division made before meshing. These CEL values result in a maximum mesh edge length on the grain surfaces of 0.0256 mm and 0.0180 mm for the coarse and fine meshes, respectively. This shows that both meshes have a maximum element size below the intrinsic cohesive length of the CCZM, Δ_{int}, and therefore should be adequate. The Voronoi grain geometries used in Chapter 6 are more geometrically complex then the current cubical samples. The maximum mesh edge length is expected to be smaller than those calculated above. This implies that grain geometry not the constitutive model determines the necessary level of mesh refinement. Therefore,

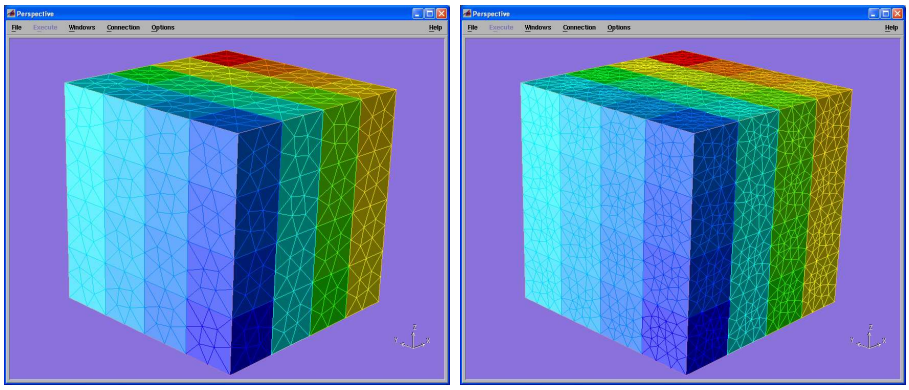

(a) Coarse mesh. (b) Fine mesh.

Figure 5.6: Coarse and fine mesh models for the 64 cubical grain sample.

both mesh models are analyzed and their results compared to determine how well they each resolve the global response and to compare solution times in anticipation that more complex grain geometries may require even finer mesh resolution.

Figure 5.7 shows the response curves for both meshes as well as the analytic solution. Both numerical solutions match the analytic solution as well as each other, resulting in the data points overlapping. This indicates mesh convergence has been reached. Therefore, the coarser mesh is of adequate refinement and is used on additional cubical grain samples. Previous results reported in this chapter utilized the coarse mesh.

5.4 Effects of Element Order on Computational Requirements

Analyses are repeated for the 64 cubical grain sample with the coarse mesh using linear and quadratic order elements. Figure 5.8 shows the resulting response curves using linear, elastic grains with bi-linear cohesive grain boundaries. As expected for the current constant strain scenario, the results for linear and quadratic order

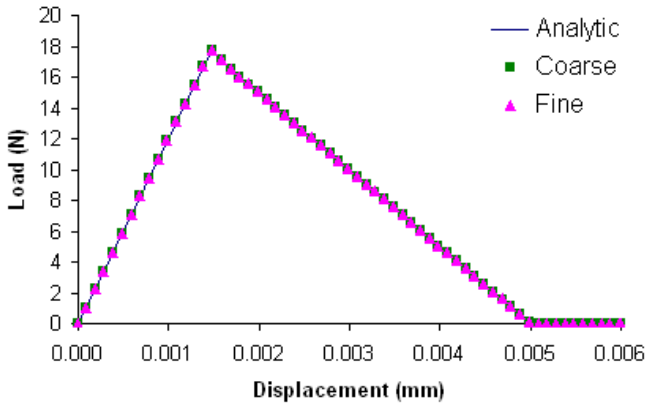

Figure 5.7: Analytic and numeric displacement versus load curves for the 64 cubical grain sample with coarse and fine mesh models.

Table 5.2: Rate-Independent FCC Crystal Plasticity Property Values

E (MPa)	ν	g_0 (MPa)	h_0 (MPa)	(ϕ, θ, ω)
75,600	0.34	228	400	$(0-2\pi, 0-\pi, 0-2\pi)$

elements match. Again, analyses are repeated using the classic rate-independent crystal plasticity model for the grains. Material property values for the rate-independent crystal plasticity model are shown in Table 5.2. Figure 5.9 shows the resulting response curves for both linear and quadratic element orders. Again, the response curves for both element orders match.

The use of quadratic order elements increases the number of DOFs present in a mesh model. This increase in mesh nodes naturally increases the computational resources necessary to conduct an analysis. Table 5.3 shows the number of DOFs for the 64 cubical grain sample using linear and quadratic order elements. Analyses in this chapter are conducted utilizing the ADMM cluster at the Cornell Theory Center. The cluster is composed of 170 nodes, each containing two 3.6 GHz Intel Xeon EM64T processors, 4 GB of RAM, 292 GB disk, and running the Windows

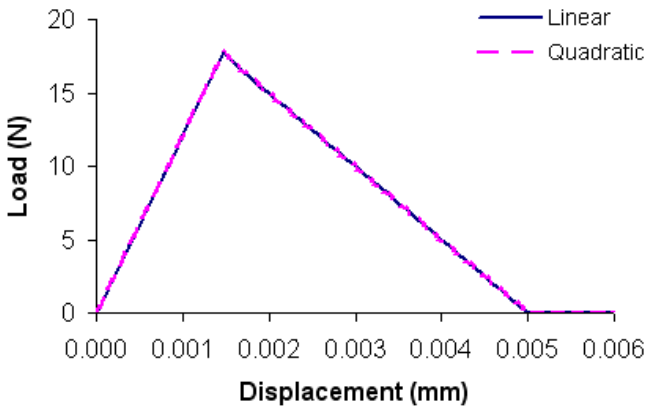

Figure 5.8: Load versus displacement curves for the 64 cubical grain sample with linear, elastic grains and bi-linear grain boundaries using linear and quadratic elements.

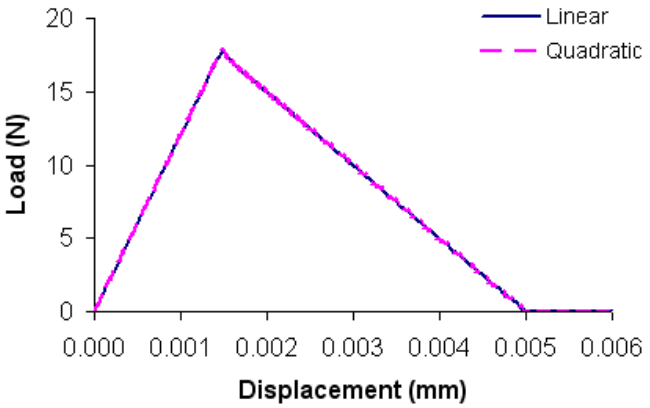

Figure 5.9: Load versus displacement curves for the 64 cubical grain sample with rate-independent plastic grains and bi-linear grain boundaries using linear and quadratic elements.

Table 5.3: Data size and solution data for linear and quadratic analyses of 64 cubical grain sample with linear, elastic grains and cohesive grain boundaries.

Model	No. DOF	Linear Elastic		Rate-Independent Plastic	
		No. Steps	Time (min)	No. Steps	Time (min)
Linear	6,219	602	72.27	602	123.27
Quadratic	60,051	602	462.66	882	1,086.73

Server 2003 operating system. The nodes are connected via Gigabit Ethernet. The table shows that using quadratic elements increases the solution time by a factor of 6.4 for linear, elastic isotropic grains and 8.8 for rate-independent crystal plastic grains. A comparison of computation time with linear and quadratic order elements is not shown for the rate-dependent crystal plasticity model. As discussed in Section 3.3.3, this model requires a mixed-formulation quadratic element; since a linear formulation is not available this comparison could not be made.

The samples analyzed here are geometrically simple compared to Voronoi grain geometries. The number of elements is expected to increase as the geometric complexity increases. Therefore, the increase in number of DOFs and computation time should be taken into account before conducting analyses with quadratic order elements.

5.5 Determining Optimal Computational Solution Parameters

Optimal computational solution parameters are now investigated to determine solver technique and step refinement. The solution framework utilized for the current analyses offers two solution techniques, *line search* and *trust region*. Due

to the global softening seen in the response curve when utilizing the cohesive grain boundaries, the trust region technique must be used. The line search technique is unable to follow the sharp transition to the negative global stiffness.

After determining the suitable solver technique, step refinement is investigated. As discussed previously, adaptive step control is utilized for the current analyses. This varies the size of the next step based on the previous step's convergence. Controlling the maximum step size gives the user the ability to trade-off accuracy and computation time. The adaptive step controller quickly increases the step size during the initial linear elastic response of the sample. Using too large of a maximum step size increases the error and difficulty finding the softening solution at the global peak. Several step sizes are investigated to determine which minimizes the number of steps taken while still yielding an accurate solution.

Figure 5.10 shows the load versus displacement curves for the bi-linear cohesive model for three step sizes. Each analysis has a linear solver tolerance of 1e-50 and a nonlinear tolerance of 5e-3. The largest step size, 0.010 μm, requires the fewest steps (302) and least computation time (35 minutes); however, error is introduced when softening begins. While this analysis eventually resolves the error, this should be considered when attempting future analyses. Decreasing the maximum step size to 0.005 μm and 0.001 μm increases the computation time to 69 and 300 minutes, respectively. Significant decreases in error introduced at softening are also seen. The maximum step size of 0.005 μm decreases the error without under estimating the softening point while only doubling the solution time. Decreasing the step size to 0.001 μm increased the computation time by a factor of 10. Using a smaller nonlinear tolerance in conjunction with the largest step size, 0.010 μm results in resolving the global peak better but also results in convergence problems during

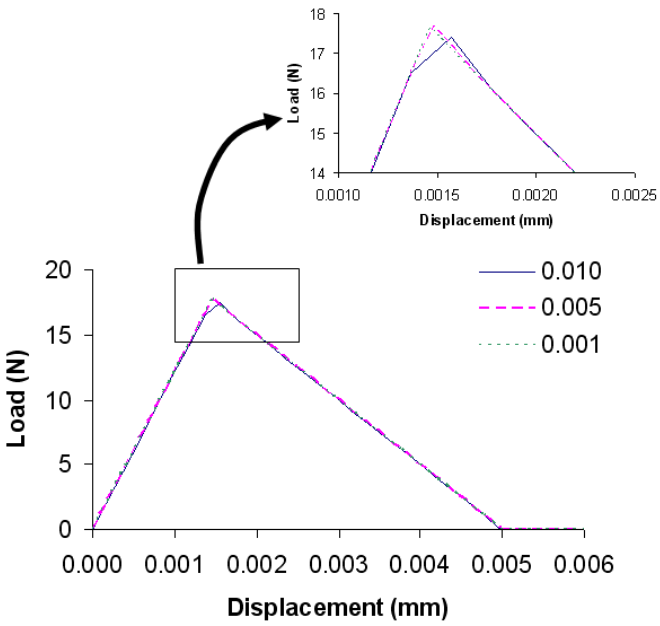

Figure 5.10: Load versus displacement curves for the 64 cubical grain sample using 0.010, 0.005, and 0.001 μm maximum step sizes.

the global softening. Therefore, a maximum step size of 0.005 μm is used with the tolerances listed above in following analyses.

5.6 Investigation of an Exponential CCZM

The above verifications were attempted using the bi-linear CCZM. An energetically equivalent set of parameters is chosen for the exponential model of Smith and Ferrante [53] discussed in Section 3.3.3. Eq. 5.8 shows the exponential CCZM where e is the e-number, δ is the current coupled opening along the grain boundary, σ_c is the peak traction, and δ_c is the characteristic opening. A set of energetically equivalent parameters is determined by setting σ_c equal to the peak traction of the bi-linear model, τ_p, and then modifying δ_c until the areas under each curve, and thus the energy for fracture, are the same. The final parameters for the exponential model are shown in Table 5.4. Note that the critical opening for the bi-linear model

Table 5.4: Energetically Equivalent Exponential CCZM Properties

σ_c	δ_c	β
450 MPa	0.00095 mm	1.0

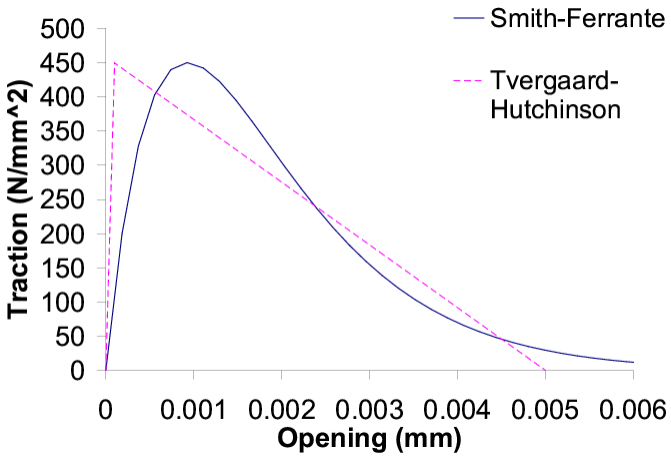

Figure 5.11: Energy equivalent bi-linear and exponential CCZM.

refers to the opening at which the traction becomes zero, nucleating a crack, while the characteristic opening for the exponential model refers to the opening at which softening begins. The equivalent CCZM models are shown in Figure 5.11. The bi-linear model is plotted using the coupled opening rather than normalized λ so the models can be directly compared. For the exponential model, an opening of 6.5 μm is chosen as the opening at which a crack nucleates.

$$\sigma = \frac{\partial \phi}{\partial \delta} = e\sigma_c \frac{\delta}{\delta_c} e^{-\delta/\delta_c} \tag{5.8}$$

The exponential model is generally expected to have less numerical difficulties due to its smooth shape and lower initial stiffness. Traditional uses of exponential cohesive models include investigating a single failure path such as the double cantilever beam specimen shown in Figure 5.12. However, the cubical grain polycrystal samples present multiple competing failure paths with loading and unloading oc-

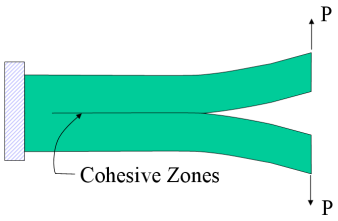

Figure 5.12: Traditional application of cohesive zone models for a cantilevered beam specimen with a single failure path.

curring simultaneously which may cause problems for the exponential model. The strategy in Section 5.5, weakening the center plane to concentrate the damage, results in one plane of grain boundaries softening and continuing to open while the others close, unloading, to maintain equilibrium. For the bi-linear model, the global response exhibited softening under this scenario. The analytic solution for the energetically equivalent exponential cohesive zone model results in the global load versus displacement curve exhibiting snap-back behavior.

Figure 5.13 shows the analytic results for a single column of four blocks connected by springs and subjected to an applied displacement in three scenarios. First, all springs follow the previous bi-linear model with the center spring weakened by 2%. Second, only the center spring is activated and follows the energetically equivalent exponential model. Finally, all the springs are activated following the exponential model with the center spring having a σ_c of 441 MPA, or 2% weaker than the other springs. For this scenario, the stronger grain boundaries do not reach the peak traction before unloading. Therefore, these springs retrace the loading path back to the origin. When only one exponential spring is active (Exponential-1), the solution exhibits global softening as seen in previous analyses. Once the other springs are activated (Exponential-All), although they are stronger than the central spring and do not soften, the global behavior shows snap-back. This is due to the comparative stiffnesses before and after reaching the peak trac-

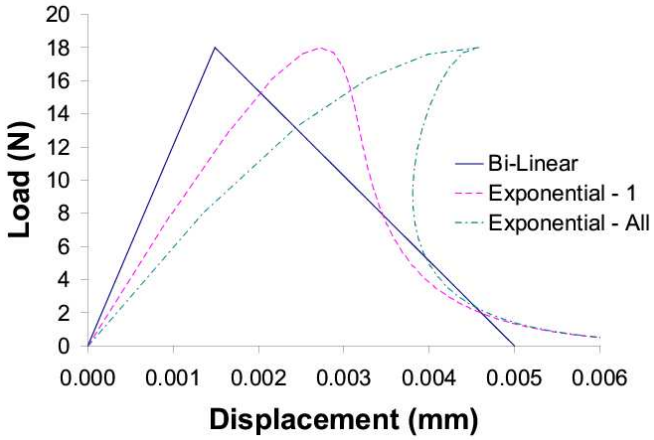

Figure 5.13: Analytic results using bi-linear and exponential CCZMs.

tion of the exponential model. The relatively slow contraction of the unloading springs does not release enough strain energy remain stable. The same scenario would result from a bi-linear CCZM with a softening slope of similar magnitude to or steeper than the initial slope.

Explicitly capturing the snap-back behavior is not the focus of this research. Instead, the focus is to monitor when and where grain boundaries soften and decohere. Therefore, numerical analyses of the cubical samples are performed using the exponential model to determine if the current solver can converge to the final configuration using the trust region technique without implementing additional features to track the snap-back path. If this is not possible, then future analyses in this thesis will not utilize the exponential model.

For the simple case of 64 cubical grains with the center plane of grain boundaries weakened by 2%, the solver is able to find an equilibrium solution consistent with the analytic results without explicitly following the snap-back path (Figure 5.14). Since the solver does not contain an arc-length method or use dynamics for following the snap-back portion of the curve, the numerical results simply snap-

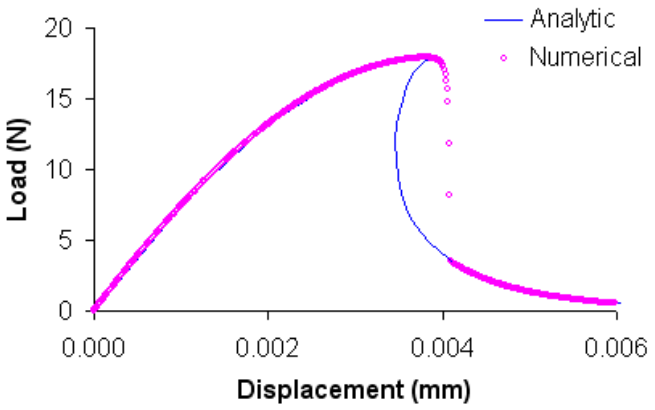

Figure 5.14: Analytic and numeric displacement versus load curve for the 64 cubical grain sample under uniaxial tension using the exponential CCZM.

through to the next portion of the curve with a positive displacement increment. Since this case completed successfully the exponential model is considered in future chapters. However, if the increase in geometric complexity or material variation prevents the solver from successfully tracking the analytic solution, the exponential model will be dropped.

5.7 Problems Increasing Sample Size

Results thus far have been reported for the 64 cubical grain sample. Before continuing to samples with increased geometric complexity, analyses are conducted on the larger cubical grain samples to identify problems due to the increasing sample size.

First, analyses are conducted on the larger samples with linear, elastic grains, bi-linear cohesive grain boundaries, and the entire center plane of grain boundaries weakened by 2%. This mirrors the analysis conducted on the 64 cubical grain sample in Section 5.2. Figures 5.15 through 5.18 show the response curves and analytic solutions. The response of the 64 cubical grain sample is repeated here

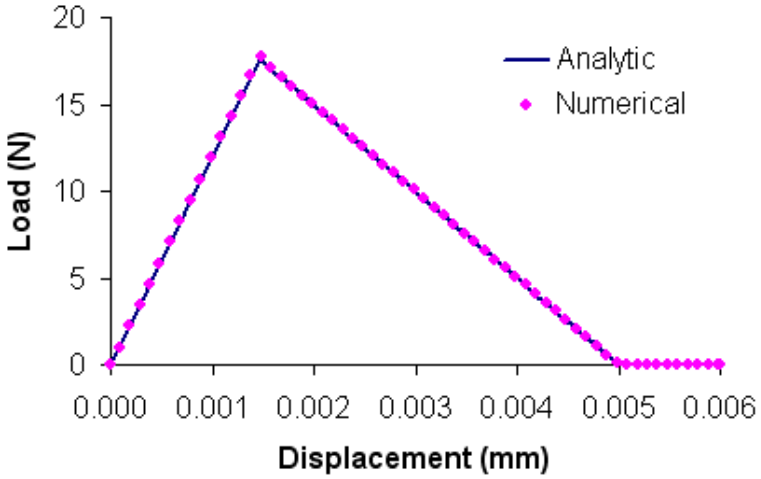

Figure 5.15: Analytic and numeric displacement versus load curve for the 64 cubical grain sample under uniaxial tension.

for ease of comparison. As the number of grains in the sample increases, the peak load of the response curve increases and shifts to the right. This results in a more brittle behavior. Traction required to softening the weakened grain boundaries remains constant. However, the increase in the area over which the displacement increases results in an increase in the peak load. As the sample size increases additional layers of grains and grain boundaries are present in the loading direction. This increases the summation of the elongation of the grains and opening of the grain boundaries; therefore, increasing the global displacement at which softening occurs. This also results in a less ductile softening response. The increase in the steepness of the softening slope results in additional error as the solver tries to traverse the peak. A maximum step of 0.005 μm was used for all analyses. Previous investigation into the maximum step size showed that an step size of 0.01 μm could be used; however, with increasing sample size the larger step size allowed too much error when global softening began. The solver was unable to resolve this error and return to the analytic solution path.

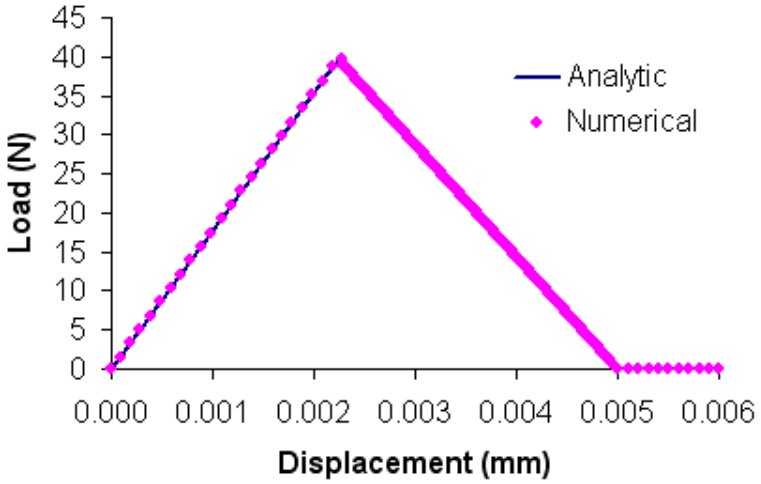

Figure 5.16: Analytic and numeric displacement versus load curve for the 216 cubical grain sample under uniaxial tension.

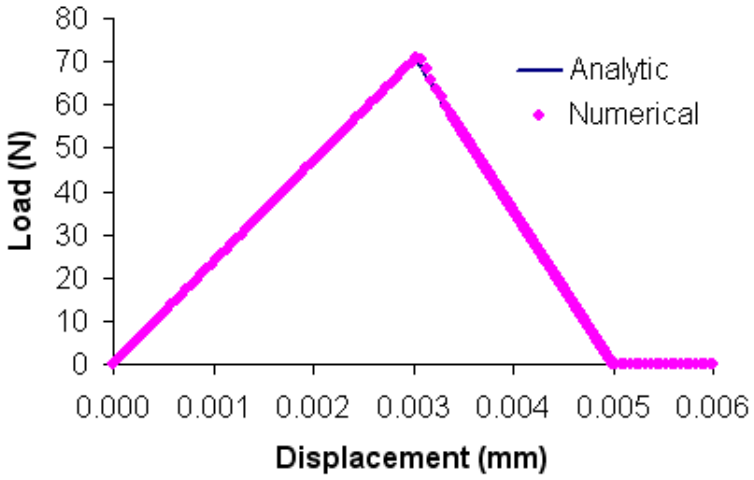

Figure 5.17: Analytic and numeric displacement versus load curve for the 512 cubical grain sample under uniaxial tension.

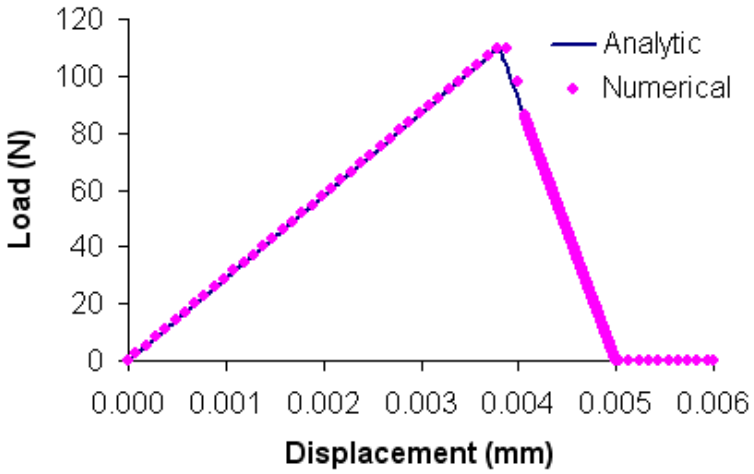

Figure 5.18: Analytic and numeric displacement versus load curve for the 1000 cubical grain sample under uniaxial tension.

The increasing sample size highlights the impact of the adaptive step controller. For all samples, the adaptive step controller reduces the step size once the solution becomes nonlinear. For the 64 cubical grain sample, the step size remains constant but the number of Newton iterations per step increases. The 1000 cubical grain sample experiences a decrease in step size size from 0.01 μm to 0.000156 μm which is visible in the graphs shown. The increase in sample size and adaptive decrease in step size impacts the number of steps taken and the solution time. Table 5.5 shows the number of steps and solution time for each analysis. Also shown are the number of DOF and the number of processors used. Again, analyses are conducted using the ADMM cluster at the Cornell Theory Center. The 1000 cubical grain sample took 10.67 days of wall clock time to complete on four processors. The times shown should be considered when attempting more complex analyses.

Next, the bi-linear cohesive grain boundaries are replaced with the exponential CCZM. As seen previously, the 64 cubical grain sample underwent snap-back which is not explicitly captured by the solver. The solver is able to find an equilib-

Table 5.5: Number of analyses steps and computational time for various sized samples of cubical grain samples.

Sample Size	No. DOF	No. Processors	No. Steps	Time (mins)
64	10,512	1	602	72.26
216	35,154	1	17,200	14,403.1
512	84,270	2	3,042	5671.1
1000	163,803	4	4,497	15,358.7

rium solution by snap-through. This behavior is expected with the larger samples. Figures 5.19(a) through 5.19(d) show the analytic and numerical solution for the 64 through 1000 cubical grain samples. Again the 64 cubical grain result is repeated here for ease of comparison. Each analytic solution exhibits the snap-back behavior. The 216 cubical grain sample initial has difficulty finding the expected solution but ultimately snaps-through. For the 512 and 1000 cubical grain samples, the solver finds alternative equilibrium solutions. Figure 5.20 shows the final displaced shape of the cohesive grain boundaries in the 512 cubical grain sample. In both cases, grain boundaries along the exterior begin to open rather than focusing the opening along the center plane. Due to the snap-back expected and inability to capture the expected solution, the exponential cohesive zone model is not considered hereafter.

5.8 Investigation of Variation of Model Parameters on Effective Response and Self-Consistency

A key question for this research concerns the impact of variation in internal properties and geometry on the circumstances of crack nucleation. The current cubical

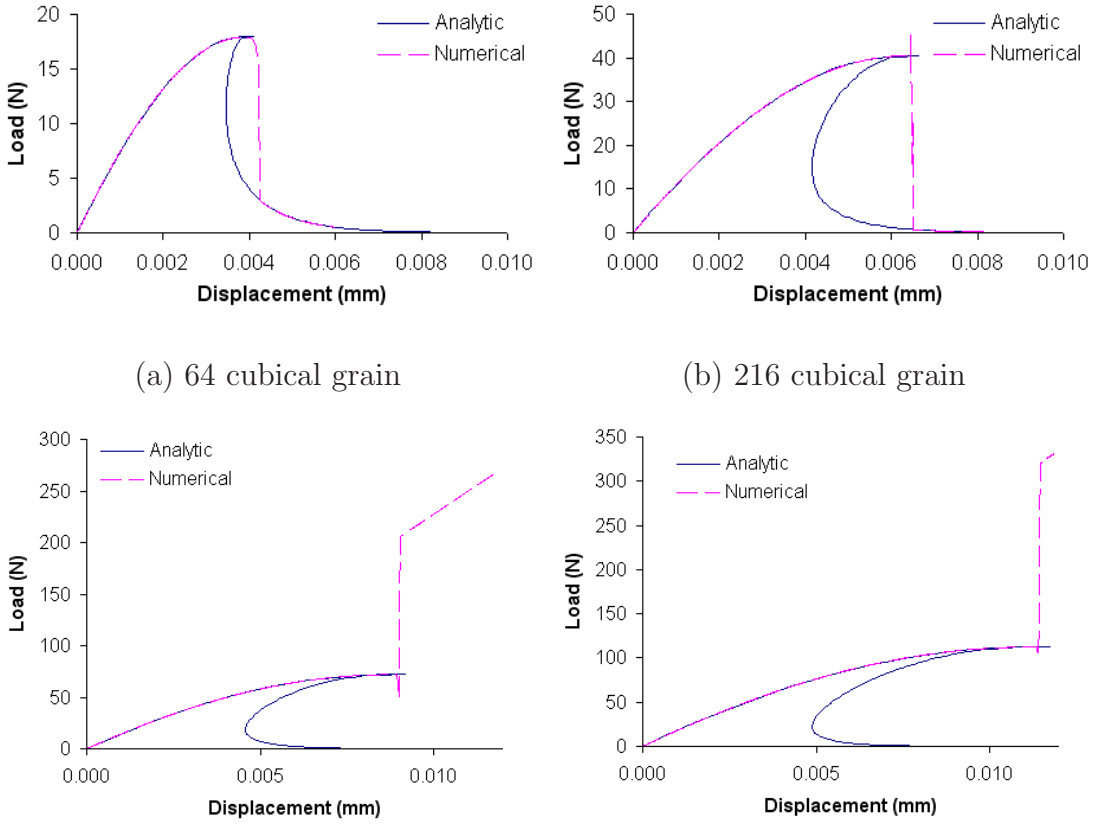

(a) 64 cubical grain

(b) 216 cubical grain

(c) 512 cubical grain

(d) 1000 cubical grain

Figure 5.19: Load versus displacement for cubical grain samples with exponential cohesive grain boundaries.

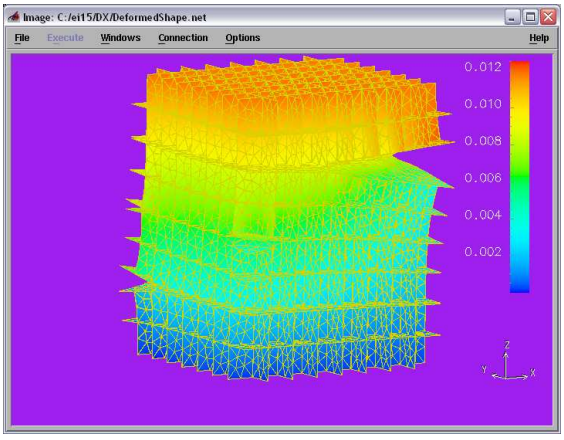

Figure 5.20: Displaced shape of model with exponential cohesive grain boundaries for the 512 cubical grain sample.

Table 5.6: Grain Material Property Distributions

Linear, Elastic Isotropic Grain Material				
E			ν	
75,600 MPa ± 10%			0.34	
Rate-Independent FCC Crystal Plasticity				
E (MPa)	ν	g_0 (MPa)	h_0 (MPa)	(ϕ, θ, ω)
75,600±10%	0.34	228±10%	400±10%	$(0-2\pi, 0-\pi, 0-2\pi)$

grain samples can be used to begin this investigation. The regular geometry of these samples means any variation in the response curve can be linked directly to the variation in internal properties rather than variation in internal geometry. The added influence of grain geometry is examined in Chapter 6.

To begin this investigation, the 64 cubical grain sample is used with linear,elastic isotropic grains without cohesive grain boundaries. Each grain of the sample is assigned randomly selected properties from the uniform distributions shown in Table 5.6. Random1-4 are four different samplings from the property distributions. Table 5.7 shows the resulting average Young's modulus for each instance, the effective Young's modulus for the 64 cubical grain sample, and the variation from the mean value. The variation between the average Young's modulus of the grains, E_{gr}, and the effective Young's modulus of the samples, E_{eff}, is below 0.15%. This low variation shows that sampling the current distributions can produce a self-consistent polycrystal sample.

Next, bi-linear cohesive grain boundaries are added to the 64 cubical grain sample. The presence of the cohesive grain boundaries without an initially rigid response is expected to reduce the effective stiffness of the sample. Following the

Table 5.7: Effective Young's Moduli for 64 cubical grain sample with linear, elastic grains and without cohesive grain boundaries

Instance	Average E_{gr} (MPa)	E_{eff} (MPa)	Difference (%)
Random1	75,546	75,431	0.15
Random2	75,678	75,612	0.09
Random3	76,906	76,826	0.10
Random4	75,665	75,597	0.09

simple analysis of the column of blocks connected by springs shows that E_{eff} can be estimated by Eq. 5.9 [68], where E_{gr} is the Young's modulus of the grains, k_i is the initial uncoupled stiffness of the cohesive model, and h_i is the spacing between cohesive boundaries. Using an E_{gr} equal to 75,600 MPa, k_i equal to 4.5e9 MPa, and h_i equal to the grain dimension 5e-5 m, the resulting E_{eff} is estimated to be 56,586 MPa.

$$E_{eff} = E_{gr}\left[1 - \frac{1}{1 + \frac{k_i h_i}{E_{gr}}}\right] \tag{5.9}$$

For these analyses, the same four instances of random grain properties are used and uniform grain boundaries are assigned properties as before from Table 5.1. The center four grain boundaries are again weakened by 2%. Figure 5.21 shows the response curves for all of random instances of E_{gr} as well as the uniform sample. Differences in the separate instances are barely detectable. The variation in E_{gr} results in the difference in initial global stiffness as well as the softening of the transition at the peak load. These differences can be seen in Figure 5.22 which zooms in on the peak of the response curves. Table 5.8 shows the average E_{gr}, E_{eff}, maximum load carried, and applied displacement at which softening occurred for each instance. For all instances, the resulting E_{eff} is slightly higher than the value estimated above. Random1, 2, and 4 are within 0.17% of the E_{eff}

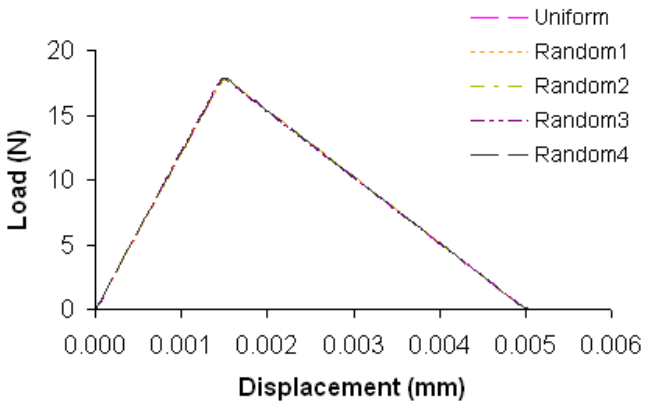

Figure 5.21: Load versus displacement curves for the 64 cubical grain sample using uniform and random grain properties.

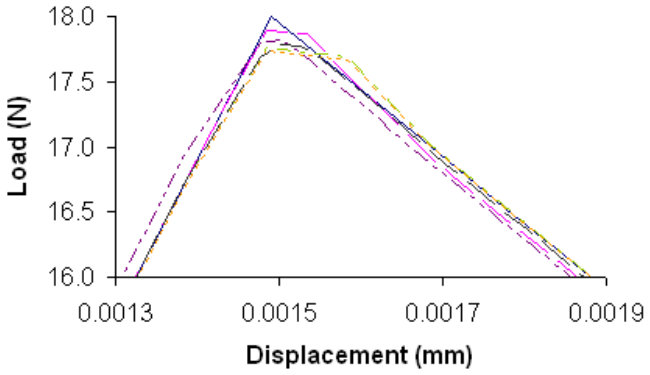

Figure 5.22: Load versus displacement curves for the 64 cubical grain sample using uniform and random grain properties.

for the uniform sample. The Random3 instance has the largest deviation from the average E_{gr} at 1.73% resulting in 1.23% variation in E_{eff}.

Each instance has the same grain boundary properties; therefore, the difference in initial softening is due to the variation in grain properties and not the presence of the initial flaw. The strain at which softening is first detected varies by only 1.2%. The maximum load carried in each instances varies by 0.05 N, or 0.83%. As seen in Figure 5.22, the variation in E_{gr} not only lowers the peak load but also results in smoothing of the transition at softening. Since all grain boundaries are

Table 5.8: Effective Young's moduli for 64 cubical grain samples with linear, elastic grains and cohesive grain boundaries

Sample	Average E_{gr} (MPa)	E_{eff} (MPa)	Maximum Load (MPa)	Softening Displacement (mm)
Uniform	75,600	60,400	17.887	0.001485
Random1	75,546	60,300	17.739	0.001485
Random2	75,678	60,371	17.785	0.001484
Random3	76,906	61,140	17.825	0.001502
Random4	75,665	60,363	17.789	0.001502

assigned the same critical opening, each instance fails at the same displacement.

This initial result indicates that a 64 cubical grain sample could be an RVE since internal property variation does not noticeably alter the global response of the sample. The sample is large enough that variations in the grain properties do not affect the overall response of the sample.

Next, analyses are conducted on the cubical grain sample without cohesive grain boundaries. Properties and orientations are selected from the distributions shown in Table 5.6. These analyses will be conducted for linear, elastic isotropic grains which do not account for orientation or for the rate-independent FCC crystal plasticity model. The samples will be loaded under the simple tension boundary conditions described earlier. The resulting effective Young's moduli are shown in Table 5.7.

Without cohesive grain boundaries present, there is mild variation in the resulting effective Young's moduli of the samples. This variation is minor enough to consider these samples self-consistent.

5.9 Summary and Conclusions

Before beginning to analyze complex 3D polycrystals, a series of analyses are conducted using polycrystal samples with cubical grains for verification and initial study. The grain and grain boundary models are verified and mesh refinement, element order, and computational solution parameters investigated. Further the exponential CCZM, flaw area, sample size, and the introduction of internal variation are investigated.

Local internal geometry provides enough mesh refinement to capture the cohesive response. The increase in computational time is noted due to the increase in DOFs when using quadratic order elements over linear order. Optimal computational solution parameters are determined and used herein. The exponential CCZM is ruled out for future investigations due to the presence of snap-back and the solver's inability to consistently find the expected solution.

Analyses are conducted on samples up to 1,000 cubical grains. These analyses contained over 160,000 DOFs and required four processors for almost 11 days of wall clock time. Samples were partitioned to yield 40,000 to 50,000 equations per processor. The majority of computation time for these analyses is spent formulating the elements and evaluating the material state rather than actually solving the equations. Therefore using more processors will provide minimal speed up. Given the available computational resources, samples of this size are able to be analyzed in a reasonable amount of time. As the geometric complexity increases, so will the number of DOFs. Therefore, it can not be automatically assumed that a more complex 1,000 grain sample is guaranteed to be tractable. This is tested in the next chapter.

The bulk response of the 64 cubical grain sample shows minimal deviation

between different instances of internal properties. This indicates the 64 cubical grain sample size can be the minimum size of an RVE. In the next chapter geometric variation can change this answer to Question 1 posed in the introduction. Given the small size indicated so far for an RVE, Question 2 is interpreted to be "how many RVE's can be encapsulated in a single sample?", or "alternatively as how much more detail (i.e. sub-grain size particles, more accurate grain material model, etc) can be added to the current RVE?" These initial analyses show that 1,000 cubical grain sample with simple grain material models can be analyses in relatively short time. However, increasing material model and geometric complexity will likely require more time and/or processors, making such samples less practical to analyze.

Chapter 6

Grain Boundary Decohesion in Statistical 3D Polycrystals

The individual components invoked to generate a complete polycrystal sample are discussed in previous chapters of this thesis. The 3D *coupled cohesive model zone* (CCZM) and interface element implementation have been verified and computational solution parameters have been determined. This chapter focuses on how these tools are used to generate a statistical set of polycrystal samples and the parametric study conducted on these samples. Section 6.1 describes how a statistical set of polycrystal grain geometries for different sized samples is created. Section 6.2 describes how the samples are completed by assigning grain and grain boundary properties from distributions of properties. Boundary conditions and loading are discussed in Section 6.3. The computational resources necessary are discussed in Section 6.4. Finally, Section 6.5 discusses the parametric space explored and the observations made concerning the influence of different internal variations on polycrystal response, including when, where, and if cracks nucleate through grain boundary decohesion.

6.1 Statistical 3D Geometry Generation

Artificial polycrystal geometries are generated using the *gen_poly* Web service available through the Geometry Tab in the Polycrystal Generator (Section 4.2). For each desired number of grains two sets of initial points, and thus tessellations, are generated. To utilize the analyses discussed in Chapter 5 to the greatest extent,

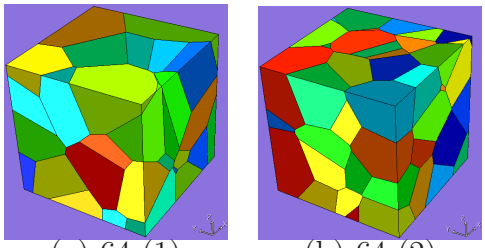

(a) 64 (1) (b) 64 (2)

Figure 6.1: Artificial 64 grain polycrystals generated using the Polycrystal Generator, with an average grain size of 50 mum and overall dimension of 0.2 mm.

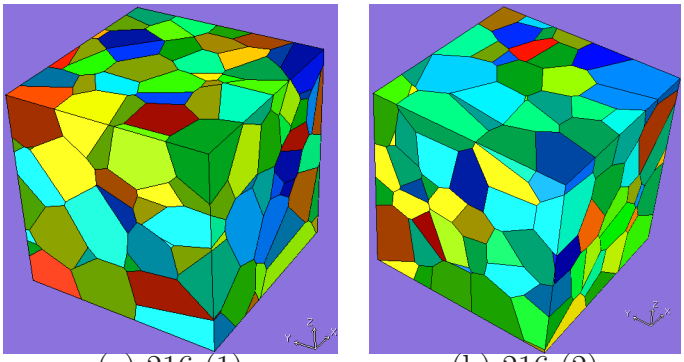

(a) 216 (1) (b) 216 (2)

Figure 6.2: Artificial 216 grain polycrystals generated using the Polycrystal Generator, with an average grain size of 50 mum and overall dimension of 0.3 mm.

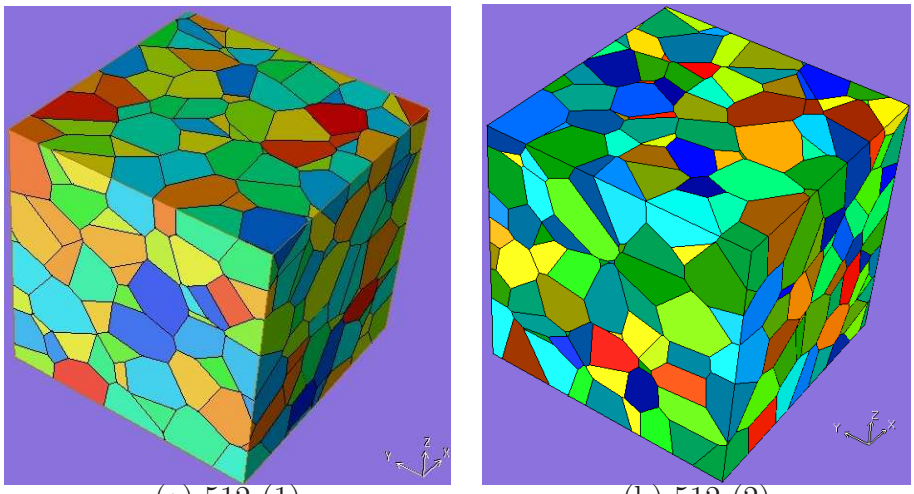

(a) 512 (1) (b) 512 (2)

Figure 6.3: Artificial 512 grain polycrystals generated using the Polycrystal Generator, with an average grain size of 50 mum and overall dimension of 0.4 mm.

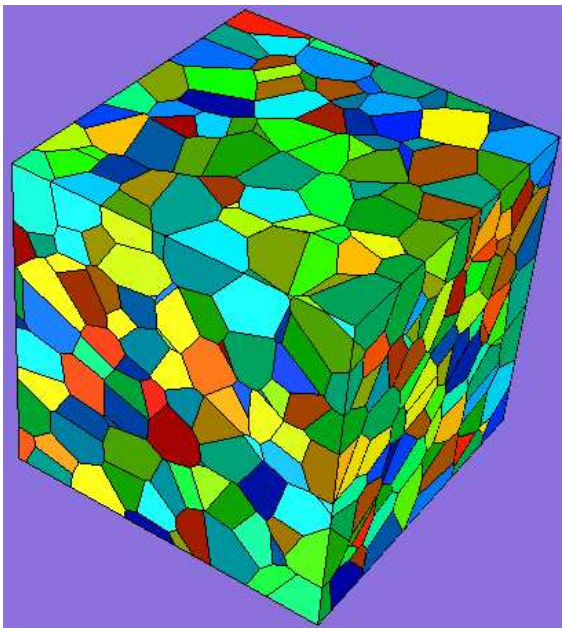

Figure 6.4: Artifical 1,000 grain polycrystal generated using the Polycrystal Generator, with an average grain size of 50 mum and overall dimension of 0.5 mm.

artificial grain geometries are generated for 64, 216, 512, and 1000 grains. Figures 6.1 through 6.4 show the samples of the grain geometries generated for each sample size which are used in subsequent analyses.

6.2 Introducing Variation in Constitutive Parameters

The next step is to assign material models and parameters to grains and grain boundaries. To study the influence of variation in grain geometry, grain properties, orientations, and grain boundary properties, each sample is analyzed using a series of property assignments.

Each grain geometry is analyzed with and without cohesive grain boundaries. For each grain geometry, individual instances are created using combinations of uniform or random grain properties and orientations. These combinations are extended with uniform or random grain boundary properties. Tables 6.1 through

Table 6.1: Linear, elastic isotropic grain material properties.

E	ν
75,600±10% MPa	0.34

Table 6.2: Rate-independent FCC crystal plastic grains material properties.

E (MPa)	ν	g_0 (MPa)	h_0 (MPa)	(ϕ, θ, ω)
75,600±10%	0.34	228±10%	400±10%	(ϕ, θ, ω)

6.4 show the grain and grain boundary property distributions used. The mean grain property values shown are bulk properties of AA 7075. For uniform property assignment, all grains or grain boundaries are assigned the mean value listed. Random properties are sampled from the uniform distributions of values indicated. Grain orientations are described using Euler angles (ϕ, ω, θ). All grains are either assigned the $(0°, 0°, 0°)$ or randomly sampled angles assuming ϕ and θ range from $0 to 2\pi$ and ω ranges from $0 to \pi$.

6.3 Description of Boundary Conditions and Loading

Samples are constrained according to one of two sets of boundary conditions. The first set results in uniaxial tension as shown in Figure 6.5(a). This most closely approximates a tension test as it would be carried out in the laboratory on a test

Table 6.3: Rate-dependent FCC crystal plastic grains material properties.

m	g_0 (MPa)	$\dot{\gamma}_0$ (s^{-1})	G_0 (MPa)	g_{s0} (MPa)	$\dot{\gamma}_s$ $(s^{-1}$)	ω
5e-3	234	1	450	750	5e10	0
# Slip Systems	μ_e (MPa)	λ_e (MPa)	η	k (MPa)	(ϕ_1, Φ, ϕ_2)	
12	28,300	60,900	0	76,766	(ϕ_1, Φ, ϕ_2)	

Table 6.4: Bi-linear coupled cohesive zone model parameters.

τ_p (MPa)	k_0 (MPa)	δ_n^c (mm)	δ_t^c (mm)	β
450±10%	$\tau_p * 50$	0.005	0.005	1.0

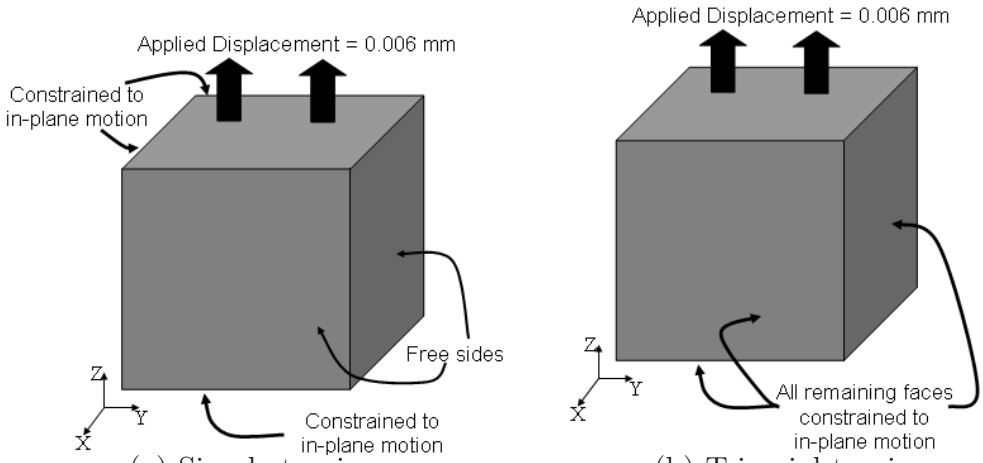

(a) Simple tension (b) Tri-axial tension

Figure 6.5: Boundary condition scenarios applied to the analyses herein.

specimen and is referred to as Type I. However, samples of the current size are actually a small volume-fraction of a test specimen. Consider extracting the current samples from an interior point of a test specimen: the surrounding material would impose additional constraint on the polycrystal samples. To approximate this situation, all sides are constrained to in-plane motion only as shown in Figure 6.5(b). This is referred to as Type II boundary conditions. The additional constraint introduced by Type II boundary conditions will alter the ultimate response of the polycrystal samples. The true boundary conditions of a small section of a test specimen are likely be somewhere between these two extreme cases. The results here can be viewed as bounding results. A displacement of 0.006 mm is applied with both sets of boundary conditions.

6.4 Computational Resources Utilized

Analyses are conducted utilizing the ADMM cluster at the Cornell Theory Center. The cluster is composed of 170 nodes, each containing two 3.6 GHz Intel Xeon EM64T processors, 4 GB of RAM, 292 GB disk, and running the Windows Server 2003 operating system. The nodes are connected via Gigabit Ethernet. Table 6.5 lists the mesh size and number of processors utilized for the polycrystal samples by size. Information is shown for the geometries designated (1) (Figure 6.1 - 6.4). Different samples of the same size are partitioned for the same number of processors since the number of elements varies only slightly. The number of DOFs listed is for linear tetrahedra and interface elements. Table 6.6 shows the number of DOFs and processors for samples using quadratic elements.

Figure 6.6 shows the mesh models for the (1) geometry of the various sample sizes. The meshes are generated using the *PolyMesh* component through the Polycrystal Generator (Section 4.2). Variation observed in mesh refinement is due to the local geometry. This variation indicates a freedom in the mesh refinement algorithm which helps to minimize the required degree of mesh refinement demanded by the geometry, thus reducing the DOFs. Alterations to *PolyMesh* to allow for local refinement due to geometry is discussed in Section 3.2.2.

Samples with linear, elastic isotropic and rate-independent crystal plasticity are analyzed using linear elements. Only samples with rate-dependant crystal plasticity are analyzed using quadratic elements to reduce the computational demand and size of output data.

Table 6.5: Mesh and computational details for polycrystal samples with linear tetrahedra and interface elements.

Sample Size (No. Grains)	No. of Tetrahedra	No. of Interface Elements	No. DOF without interfaces	No. DOF with interfaces	No. Processors
64	196,092	16,423	105,060	133,098	4
216	969,742	82,971	502,590	640,878	8
512	2,374,186	203,313	1,225,191	1,563,420	32
1000	4,732,648	410,570	2,434,944	3,117,048	64

Table 6.6: Mesh and computational details for polycrystal samples with quadratic tetrahedra and interface elements.

Sample Size (No. grains)	No. DOF without interfaces	No. DOF with interfaces	No. of Processors
64	808,485	913,641	16
216	3,935,571	4,460,415	32
512	9,612,756	10,897,620	128
1000	19,132,230	21,725,151	256

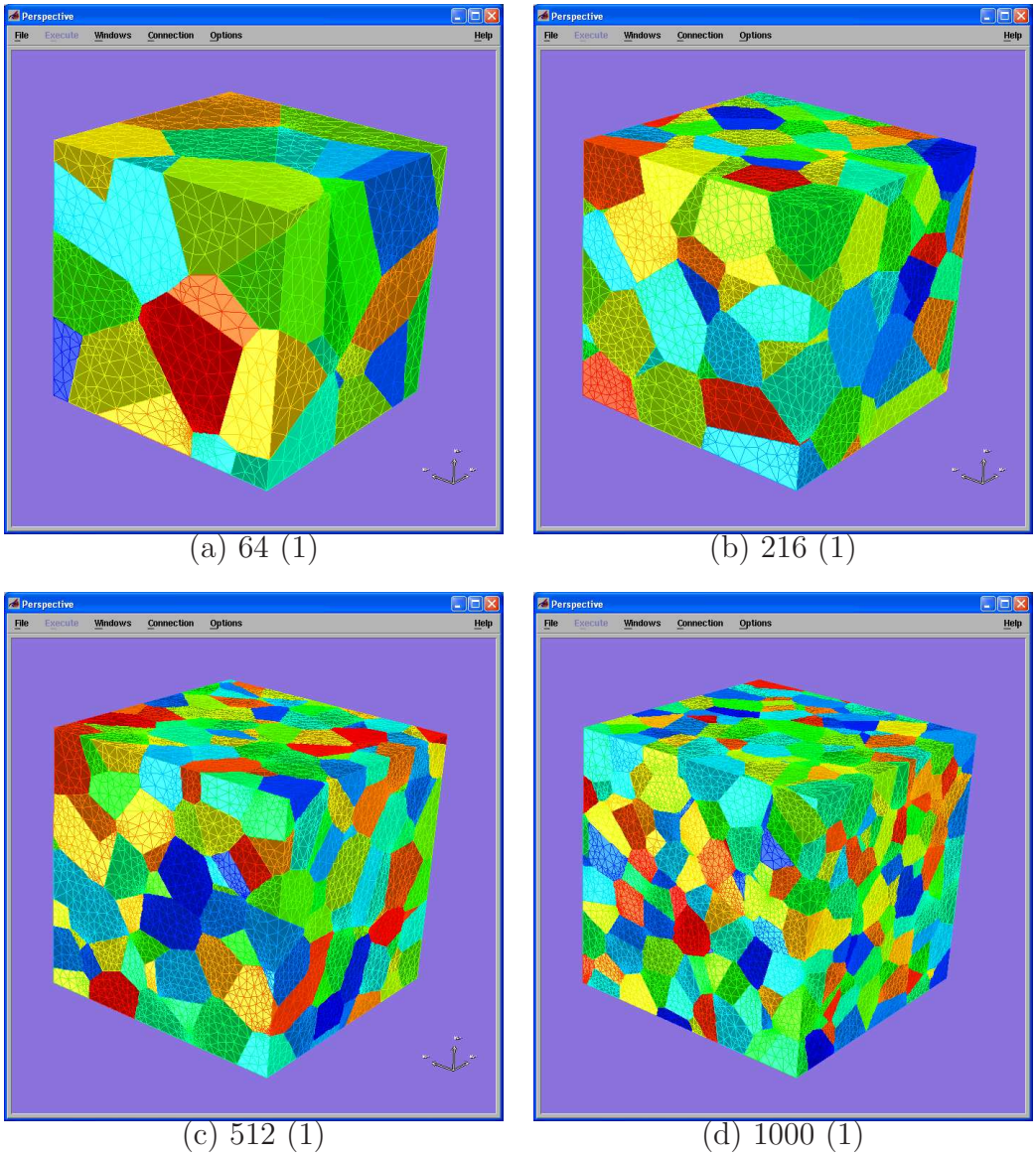

(a) 64 (1) (b) 216 (1)

(c) 512 (1) (d) 1000 (1)

Figure 6.6: Finite element meshes for each sample size.

6.5 Observations of Internal Variation

A family of artificial polycrystal samples is generated. Each sample is assigned a series of uniform or distributed grain and grain boundary properties. The samples are loaded using an applied displacement of 0.006 mm. The response of each sample is evaluated using: the effective Young's modulus, E_{eff}, of the sample; response curve; applied displacement at which plasticity, cohesive softening and decohesion are detected; and stress contours. Section 6.5.1 discusses the differences in response due to varying the Young's modulus assigned to each grain, E_{gr}, in samples with and without cohesive grain boundaries. Next, the influence of grain orientation (for plasticity models only) is studied in Section 6.5.2. The influence of varying the cohesive grain boundaries properties is then discussed in Section 6.5.3. The influence of constraining the sides of the samples with Type II boundary conditions is investigated in Section 6.5.4.

6.5.1 Variation in Response Due to Grain Properties

Each sample is first analyzed without cohesive grain boundaries. The samples are analyzed with all grains being assigned the same Young's modulus. The analyses are then repeated with randomly selected individual E_{gr} from the uniform distribution shown in Table 6.1. Two distributions termed Random1 and Random2 of E_{gr} are created for each sample size. The resulting average E_{gr} and E_{eff} for the uniform and random samples are shown in Table 6.7.

As expected, when all grains are assigned the same E_{gr}, the samples acted as homogeneous blocks returning an E_{eff} equal to the uniform E_{gr}. Varying E_{gr} alters the E_{eff} of each sample. For all samples, the difference in E_{eff} from the

Table 6.7: Average E_{gr} and resulting E_{eff} for artificial polycrystals without cohesive grain boundaries.

Sample Size	Uniform	Random1		Random2	
	E_{gr}/E_{eff} (MPa)	Avg. E_{gr} (MPa)	E_{eff} (MPa)	Avg. E_{gr} (MPa)	E_{eff} (MPa)
64 (1)	75,600	75,882	76,047	75,655	75,545
64 (2)	75,600	75,691	75,640	75,473	75,375
216 (1)	75,600	75,849	75,730	75,405	75,167
216 (2)	75,600	75,524	75,237	75,293	75,306
512 (1)	75,600	75,389	75,340	75,773	75,804
1000 (1)	75,600	75,779	75,673	75,512	75,373

mean distribution value of 75,600 MPa is below 0.6%. The difference in E_{eff} from the average E_{gr} is below 0.38%. The variation in average E_{gr} and resulting E_{eff} between the two different 64 and 216 grain geometries is less than one half of one percent. Therefore, due to the computational complexity only one geometry for the 512 and 1000 grain samples is analyzed and reported. Figure 6.7 shows the heterogeneous stress field produced by the variation in E_{gr} compared to the homogeneous field produced by the uniform E_{gr} for the 216(1) sample. The grain boundaries are super-imposed over the stress contours. The variation for the Random1 distribution clearly reflects the geometry since the internal variation is grain by grain.

The above analyses are repeated, this time introducing cohesive grain boundaries. The grain boundaries are assigned uniform parameter values from Table 6.4. Again, the samples are first analyzed with uniform E_{gr} before being repeated using a distribution of E_{gr} values. A second random distribution is used only for analyses

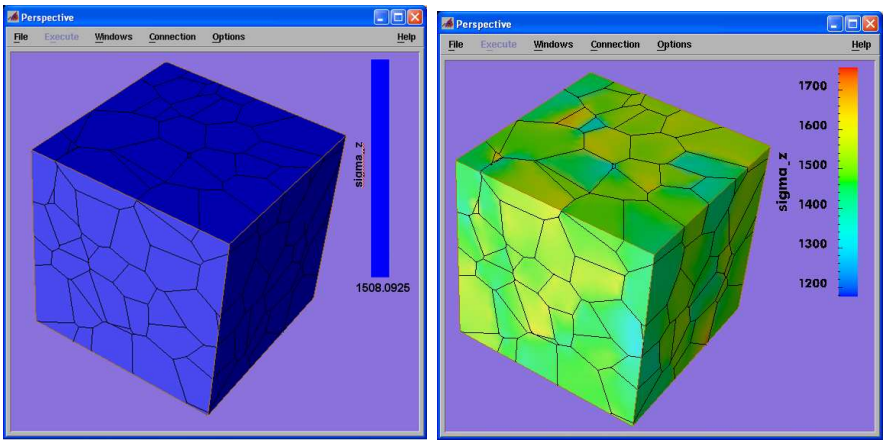

(a) Uniform E_{gr} (b) Random1 E_{gr}

Figure 6.7: σ_{zz} stress contours for the 216(1) grain sample using linear, elastic isotropic grains with Uniform and Random1 instances of E_{gr}.

of the 64(1) and 64(2) samples. Table 6.8 shows the E_{eff} and applied displacement at which softening is first detected, Δ_{soft}, for each sample and grain property distribution. For these and all analyses containing cohesive grain boundaries, the ability to specify the first step taken by the solver is used to ease calculating E_{eff}. The first step is set to 0.002 μm. E_{eff} is calculated using this first very small step to capture only the initial elastic response of the grain boundaries and not to accidentally include grain boundary softening.

The introduction of cohesive grain boundaries results in reducing E_{eff} for all samples. From Chapter 5, Eq. 5.9 estimates E_{eff} for a regular geometry and uniform E_{gr} to be 56,586 MPa. This estimate results in a lower bound for the current bulk response. The E_{eff} values shown in Table 6.7 are between 5.3% and 7.9% higher than the estimated E_{eff}. The differences in E_{eff} between samples of the same size can be attributed to the varying grain geometry and thus the variation in spacing between the cohesive grain boundaries. Variation in E_{eff} as a result of varying E_{gr} for each sample is below 0.4%. For all samples, Δ_{soft} varied

Table 6.8: Effective Young's moduli, E_{eff}, and global displacement at which softening was first detected, Δ_{soft}, for artificial polycrystals with cohesive grain boundaries.

Sample Size	Uniform		Random1		Random2	
	E_{eff} (MPa)	Δ_{soft} (μm)	E_{eff} (MPa)	Δ_{soft} (μm)	E_{eff} (MPa)	Δ_{soft} (μm)
64 (1)	60,810	1.095	61,036	1.065	60,768	1.075
64 (2)	60,859	0.975	60,851	0.985	60,702	1.005
216 (1)	60,162	1.415	60,211	1.445	—	—
216 (2)	59,888	1.415	59,621	1.445	—	—
512 (1)	59,126	1.875	59,097	1.895	—	—

1-3% due to the variation in E_{gr} and grain geometry.

Figure 6.8 shows the response curves for each distribution and geometry. Variation in E_{eff} as a result of varying E_{gr} for each sample is below 0.4%. For all samples, Δ_{soft} varied 1-3% due to the variation in E_{gr} and geometry. The response curves for different instances of a given sample are nearly indistinguishable. Slight differences are seen at the tail end of the response curve. Many of the response curves shown in Figure 6.8 terminate before reaching the full applied displacement of 0.006 mm. This can be attributed to a couple of causes. First, each analysis is given a finite amount of computational time during which to complete. The maximum time given is 10 days of wall clock time. For those analyses that do not complete in the allotted time, the available data is collected and the analysis terminated. This is most applicable to the 512 and 1000 grain samples. Second, the solver is unable to continue to find a converged solution. In the case of the 64 (2) sample, the solver is unable to apply the full displacement with uniform grain

properties and the Random1 distribution of E_{gr}. However, selecting a different distribution of values, e.g. Random2, does allow the analysis to reach the full displacement.

For all samples, non-convergence occurs after significant softening developed. As reported above, only minor variation is seen in E_{eff} before softening as well as in Δ_{soft}. Minor variation is also seen in the peak load carried by the samples. The instances in which the solver applied the full displacement show failure of the sample due to a through crack forming. Figure 6.9 shows the final λ contours for the Uniform and Random1 distributions of sample 216(1). Both instances show that softening is localizing within the sample. However, the variation in E_{gr} results in altering which grain boundaries soften. Introducing this variation distributed the softening along more grain boundaries. This can account for the post-softening deviation in the response curves in Figure 6.8c. Figure 6.10 shows the λ contours of the internal grain boundaries. For the uniform E_{gr} instance, a through crack is beginning to form. Softening is focusing along a set of grain boundaries that divide the sample into two pieces. Grain boundaries along the outer edge of the sample are fully debonded while the grain boundaries in the center of the sample are still softening. The maximum λ value in the sample is 1.13. The sample is rotated in Figure 6.9b to show that softening is localizing along two surfaces within the sample. The maximum opening seen for the Random1 instance is 1.0089 which is lower than seen in the Uniform instance.

6.5.2 Variation in Response Due to Grain Orientation

Next, the orientation of each grain is varied. Grain orientation does not influence the linear, elastic isotropic grain material model so it is not be considered here.

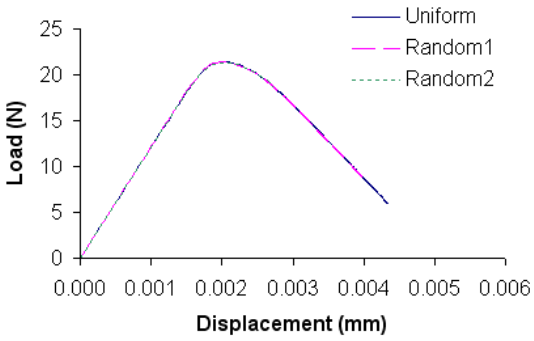

(a) 64 (1)

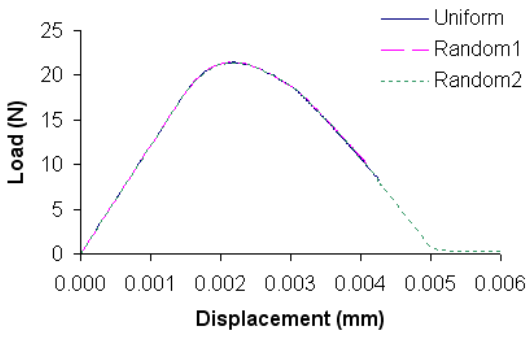

(b) 64 (2)

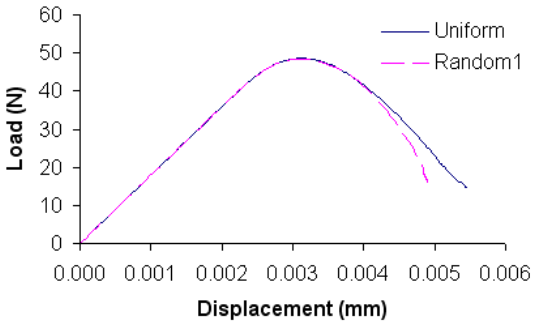

(c) 216 (1)

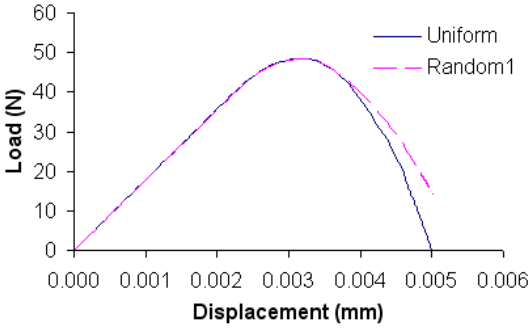

(d) 216 (2)

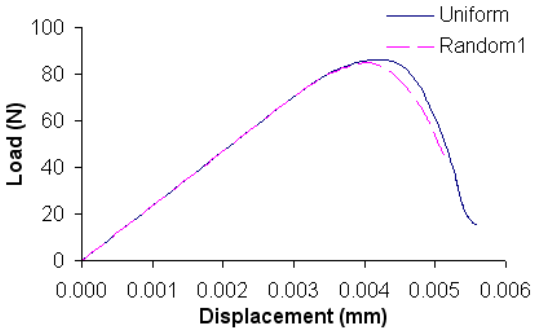

(e) 512 (1)

Figure 6.8: Response curves for different geometries with all grains having the same or random grain parameters with cohesive grain boundaries.

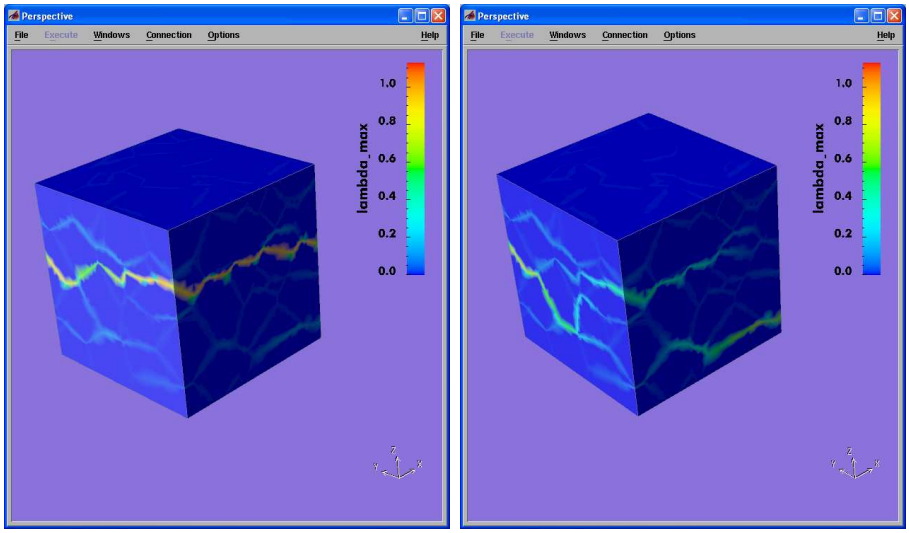

(a) Uniform E_{gr} (b) Random E_{gr}

Figure 6.9: Final λ contours for the 216(1) grain sample with uniform and random values of E_{gr}.

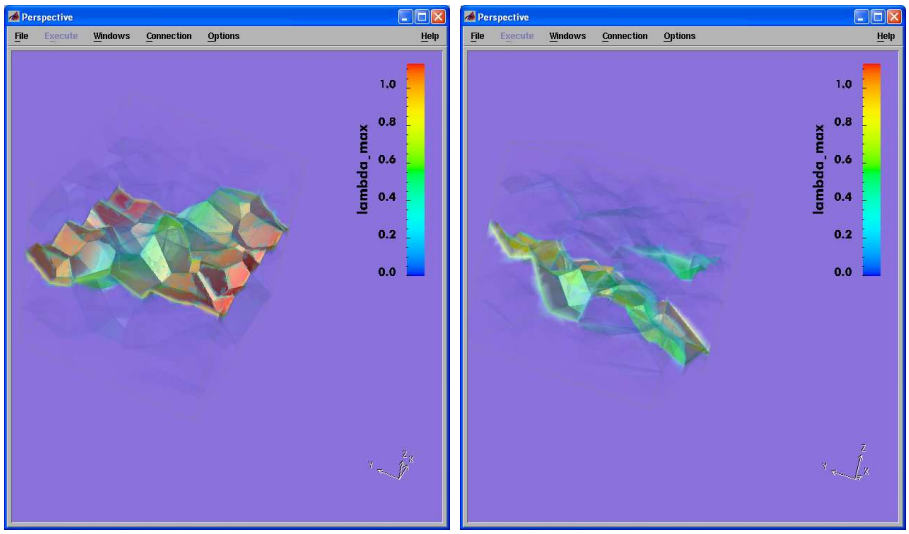

(a) Uniform E_{gr} (b) Random E_{gr}

Figure 6.10: Internal grain boundary damage for the 216(1) grain sample with uniform and random values of E_{gr}.

Only the rate-independent and rate-dependent plasticity models are discussed. First, the samples are analyzed without cohesive grain boundaries and with all grains being assigned the orientation $(\phi, \theta, \omega) = (0°, 0°, 0°)$. The grains are then each assigned random orientations from $\phi = 0to2\pi$, $\theta = 0to\pi$, and $\omega = 0to2\pi$. For both 64 grain samples with rate-independent crystal plasticity, a second distribution of orientations is also analyzed. For all samples, the grain boundary parameters are uniform. For both plasticity models, E_{gr} is 75,600 MPa and is unaffected by orientation prior to plasticity being activated; therefore, E_{eff} is also initially 75,600 MPa. Variation in the response of the samples is not seen until plasticity is activated in the sample.

Table 6.9 shows the applied displacement at which plasticity is first detected, Δ_{yld}, for the rate-independent crystal plasticity model. Again a second orientation sampling is only analyzed for the 64(1) and 64(2) samples. The Δ_{yld} reported for the 64 and 216 grain samples show that geometry has no affect on the displacement at which yielding begins. Therefore, due to the computational requirements the 512(2) and 1000(2) samples are not analyzed.

Table 6.10 shows the applied displacement at which plasticity is first detected for the rate-dependent crystal plasticity model. Again, due to the computational requirements the 512(2) and 1000(2) samples are not analyzed. The Δ_{yld} reported here does not show the geometry independence seen with the rate-independent model.

The solid curves in Figure 6.11 correspond to the response curves for the instances with uniform orientations. These curves exhibit a sharp transition between the elastic and plastic regimes. The dashed curves correspond to instances with randomly assigned orientations. The added variation softens the transition from

Table 6.9: Global displacement at which plasticity was first detected, Δ_{soft}, for samples with variation in grain orientation using rate-independent crystal plasticity.

Sample Size	$\Delta_{yld}(\mu m)$		
	Uniform	Random1	Random2
64 (1)	1.485	1.215	1.215
64 (2)	1.485	1.215	1.215
216 (1)	2.225	1.815	—
216 (2)	2.225	1.815	—
512 (1)	2.965	2.415	—
1000 (1)	3.694	3.024	—

Table 6.10: Global displacement at which plasticity was first detected, Δ_{soft}, for samples with variation in grain orientation using rate-dependent crystal plasticity.

Sample Size	$\Delta_{yld}(\mu m)$	
	Uniform	Random1
64 (1)	1.294	1.114
64 (2)	1.524	0.804
216 (1)	2.254	1.514
216 (2)	1.934	1.404
512 (1)	1.204	1.954

elasticity to plasticity and lowers the yield stress of the samples. However, the resulting hardness is higher, leading to an increased ultimate stress. For the smaller 64 grain samples, the analyses with Uniform and Random1 orientations do not reach the full applied displacement. The small size of the sample made the analysis much more sensitive to the particular distribution of grain orientations. The Uniform and Random1 distributions for both the 64 grain samples suffer non-convergence. The Random2 instance happens to be a more favorable distribution of orientation. This distribution allows the analyses to complete.

Figure 6.12 shows the σ_{zz} stress contours for the 216(1) sample using the Uniform and Random1 orientation samplings. As expected, the Uniform assignment results in a constant stress throughout the sample while the Random1 distribution shows variation in stress level. Again the variation has a geometry dependence. Higher stress values are seen along grain boundaries and around grain junctions highlighting the geometry.

As before, the above analyses are repeated with cohesive grain boundaries. Again, all grain boundaries are assigned the same parameters. The resulting applied displacement at which plasticity and cohesive softening are first detected, Δ_{yld} and Δ_{soft} respectively, are shown in Table 6.11. For all instances, plasticity is detected first followed by grain boundary softening. The applied displacement at which plasticity is activated is greatly lowered by introducing the cohesive grain boundaries. This may be due to the high initial stiffness of the CCZM. Comparing the Δ_{soft} seen here to Table 6.8, the displacement levels are only slightly lowered by introducing plasticity. Results are not reported for the rate-dependent crystal plasticity model with cohesive grain boundaries. This plasticity model diverges before softening or plasticity is detected. For future attempts this plasticity model

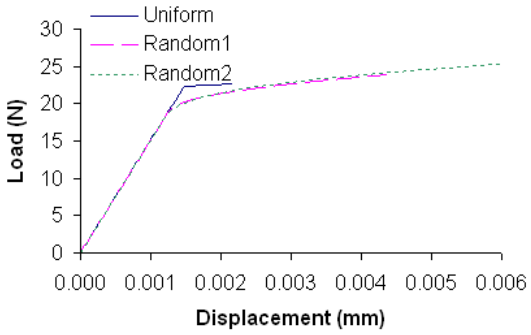

(a) 64 (1)

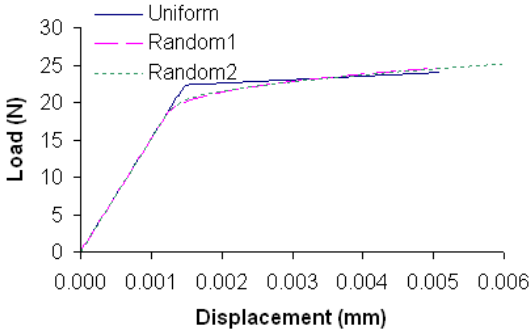

(b) 64 (2)

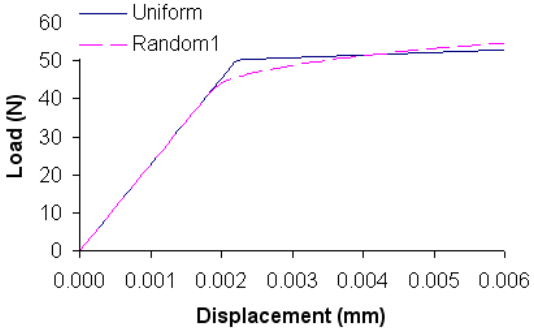

(c) 216 (1)

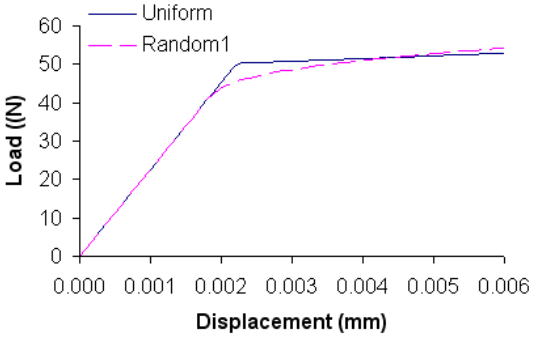

(d) 216 (2)

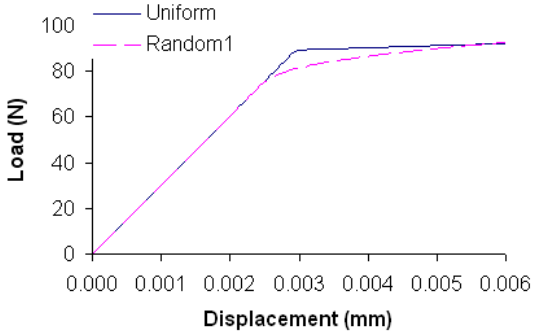

(e) 512 (1)

Figure 6.11: Response curves for different geometries with all grains having the same or random orientations using rate-independent crystal plasticity.

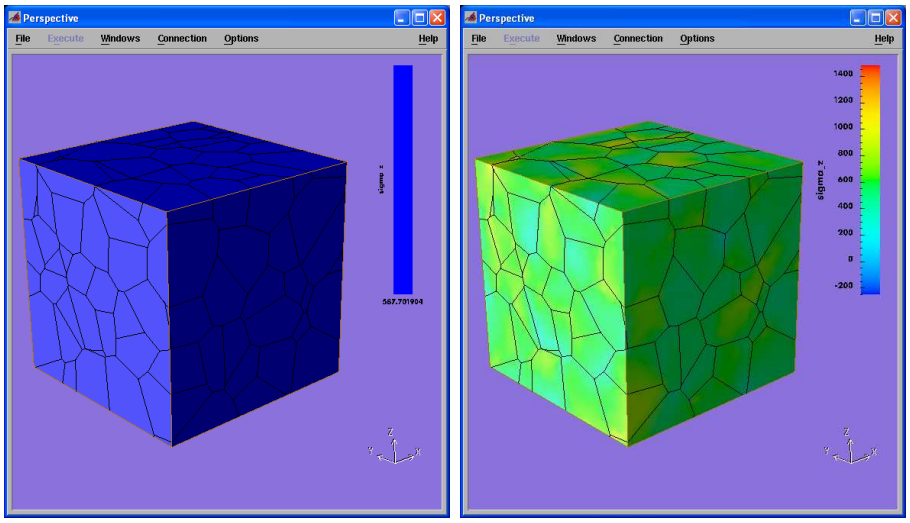

(a) Uniform E_{gr} (b) Random E_{gr}

Figure 6.12: Elastic σ_{zz} contours for the 216(1) grain sample with uniform and random values of E_{gr}.

should be examined with a rate-dependent CCZM.

Figure 6.13 shows the response curves for the samples with cohesive grain boundaries. Until grain boundary softening occurs, there is no distinguishable difference between the uniform and random orientations. Once softening occurs, the presence of random orientations greatly alters the load path. The ultimate load is lowered and the transition to global softening is drawn out. This results in a higher load capacity where the analyses terminated.

Figure 6.14 shows the final λ contours for the 216(1) grain sample with Uniform and Random1 orientations. The analysis using the Uniform orientation distribution locked shortly after softening began. Consequently, the grain boundary opening has not begun to localize within the sample. The analysis of the Random1 distribution of orientations continued significantly further. In this case, grain boundary damage has localized within the sample. Figure 6.15 shows the localized damage inside of the polycrystal.

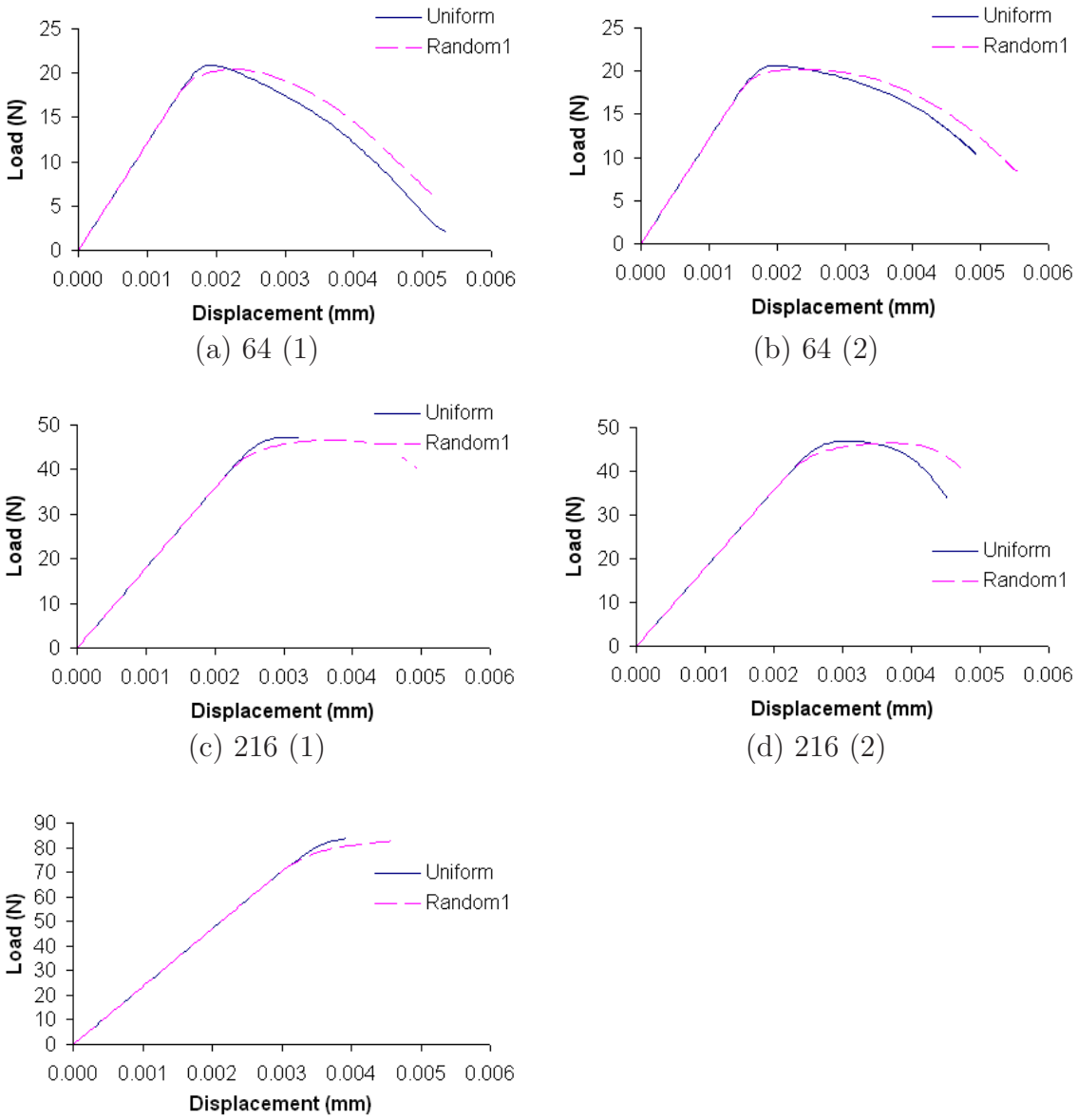

(a) 64 (1)

(b) 64 (2)

(c) 216 (1)

(d) 216 (2)

(e) 512 (1)

Figure 6.13: Response curves for different geometries with all grains having the same or random orientations with cohesive grain boundaries

Table 6.11: Global displacements at which yielding, Δ_{yld}, and cohesive softening, Δ_{soft}, are first detected for samples with various grain orientation and cohesive grain boundaries using rate-independent crystal plasticity.

Sample Size	Uniform		Random1	
	Δ_{yld} (μm)	Δ_{soft} (μm)	Δ_{yld} (μm)	Δ_{soft} (μm)
64 (1)	0.074	1.095	0.064	1.095
64 (2)	0.125	0.975	0.115	0.975
216 (1)	0.495	1.415	0.555	1.415
216 (2)	0.305	1.565	0.325	1.565
512 (1)	0.504	1.875	0.554	1.874

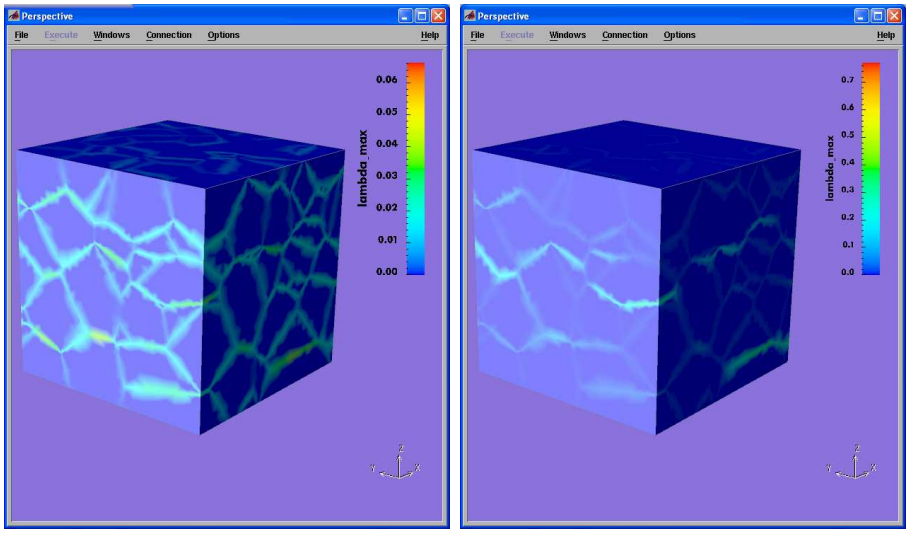

(a) Uniform E_{gr} (b) Random E_{gr}

Figure 6.14: Final λ contours for the 216(1) grain sample with uniform and random grain orientations and rate-independent plasticity.

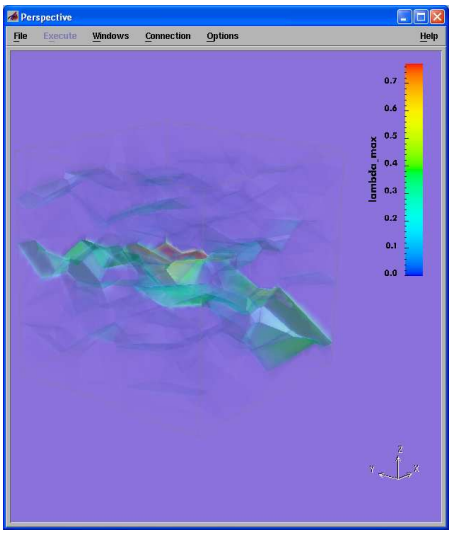

Figure 6.15: Internal grain boundary damage for the 216(1) grain sample with random rain orientations and rate-independent plasticity.

6.5.3 Variation in Response Due to Grain Boundary Parameters

Up to this point, the variation introduced has been limited to the grain material model and properties. Analyses have been conducted without cohesive grain boundaries and with all grain boundaries using the same parameter values. The next analyses are conducted varying the grain boundary parameters. Each grain boundary is randomly assigned parameter values from the distributions shown in Table 6.4. Results shown here are for each grain material model with uniform grain properties and orientations.

Variation in the resulting E_{eff} and Δ_{soft} are shown in Table 6.12. Introducing variation in the grain boundary parameters results in a slight lowering of E_{eff} of less than 0.1%. A lowering of Δ_{soft} is also seen of 3-12%. Both results can be attributed to the minimum peak traction being lower than the mean value used previously.

Table 6.12: Resulting E_{eff} and Δ_{soft} due to variation in cohesive grain boundary parameters.

Sample Size	Uniform		Random1	
	E_{eff} (MPa)	Δ_{soft} (μm)	E_{eff} (MPa)	Δ_{soft} (μm)
64 (1)	60,810	1.095	60,757	1.065
64 (2)	60,859	0.975	60,838	0.875
216 (1)	60,162	1.415	60,077	1.245
216 (2)	59,888	1.565	59,860	1.455
512 (1)	59,126	1.875	59,108	1.784

Figure 6.16 shows the response curves for the different samples with Uniform and Random1 grain boundary property distributions with linear, elastic grains. For each sample, only minor deviation is seen in the response curves. For the 64(2) grain sample, introducing variation in the grain boundaries allowed the full displacement to be applied. The grain boundary variation also allowed the 64(1) sample to strain further before suffering non-convergence.

6.5.4 Variation in Response Due to Boundary Conditions

As previously discussed, two sets of boundary conditions are being considered. Type I allows the sides of the samples to contract as would be seen in a test specimen under uniaxial tension. Analyses discussed so far in this chapter have utilized Type I boundary conditions. Type II constrains the free sides in Type I to in-plane motion only to emulate the additional constraint that a sample embedded inside the test specimen would experience. The real boundary conditions of a sample taken from the surface of a test specimen would fall somewhere between these two extremes. The following analyses examine the influence on the sample's

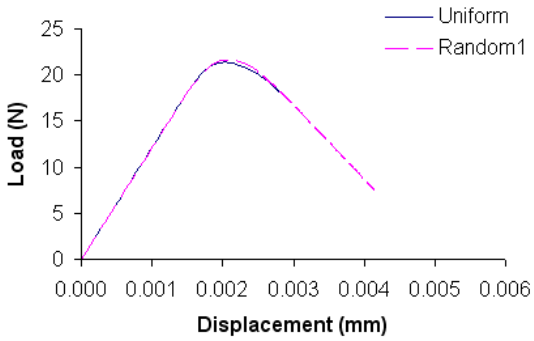

(a) 64 (1)

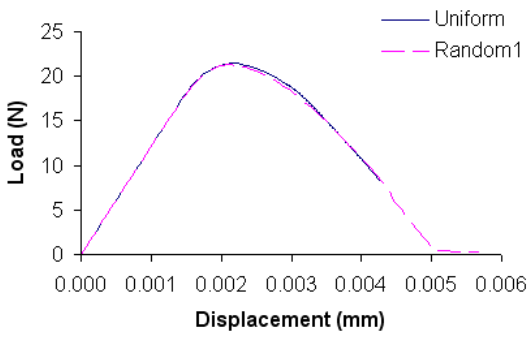

(b) 64 (2)

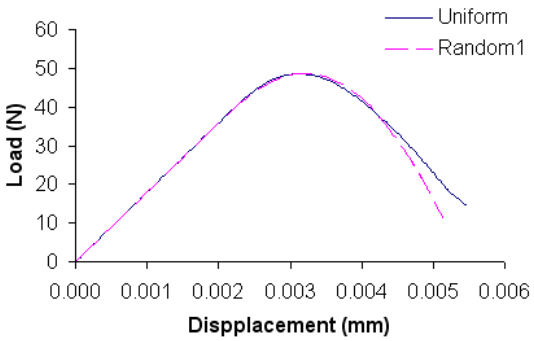

(c) 216 (1)

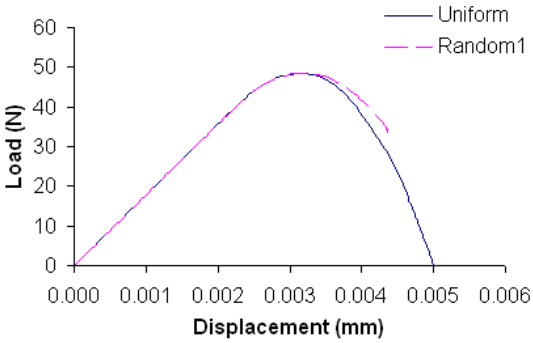

(d) 216 (2)

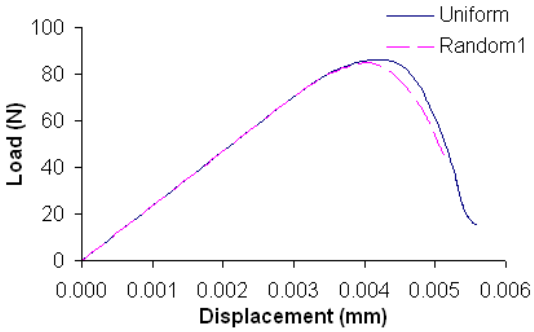

(e) 512 (1)

Figure 6.16: Resulting different response curves due to fixed or random grain boundary properties.

Table 6.13: Variation in E_{eff} due to boundary condition type in samples with linear, elastic grains.

Sample Size	E_{eff} (MPa)			
	Uniform, Type I	Uniform, Type II	Random1, Type I	Random1, Type II
64 (1)	75,600	116,362	76,047	116,983
216 (1)	75,600	116,362	75,730	116,513

response due to the two extreme boundary conditions.

First, analyses are conducted using each grain material model without cohesive grain boundaries for the 64(1) and 216(1) grain samples. These analyses are used to gauge the response of the grain material models under each set of boundary conditions. Table 6.13 shows E_{eff} for each sample under both types of boundary conditions for the Uniform and Random1 instances. The additional constraint of Type II boundary conditions results in increasing E_{eff} approximately 50% for samples with linear, elastic grains. Table 6.14 shows the same 50% increase in E_{eff} for rate-independent crystal plastic grains as well as a 33% increase in the displacement level at which plasticity is first detected. Figure 6.17 shows the response curves for each sample with rate-independent crystal plasticity under both sets of boundary conditions. The increased E_{eff} can be seen along with increases in the load at which yielding occurs and the hardening modulus. Ultimately though the samples that experienced non-convergence under Type I still experience non-convergence at the same displacement under Type II boundary conditions.

Table 6.14: Variation in Δ_{yld} due to boundary condition type in samples with rate-independent crystal plasticity and without cohesive grain boundaries.

Sample Size	$\Delta_{yld}(\mu m)$			
	Uniform, Type I	Uniform, Type II	Random1, Type I	Random1, Type II
64 (1)	0.74245	0.99225	0.60725	0.81225
216 (1)	1.1125	1.48725	0.90725	1.21725

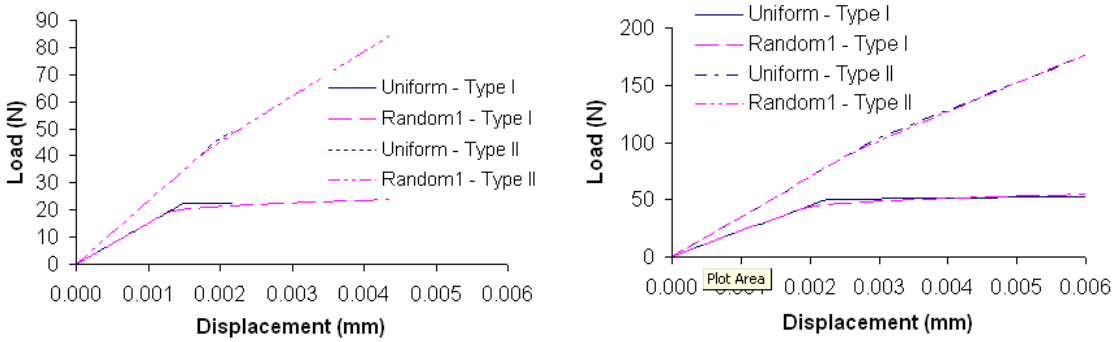

(a) 64 (1) (b) 216 (1)

Figure 6.17: Resulting different response curves due to various boundary conditions.

Table 6.15: Variation in E_{eff} due to boundary condition type in samples with rate-independent crystal plasticity and cohesive grain boundaries.

Sample Size	E_{eff} (MPa)			
	Uniform, Type I	Uniform, Type II	Random1, Type I	Random1, Type II
64 (1)	60,810	76,088	61,036	76,305
216 (1)	60,162	74,737	52,687	65,423

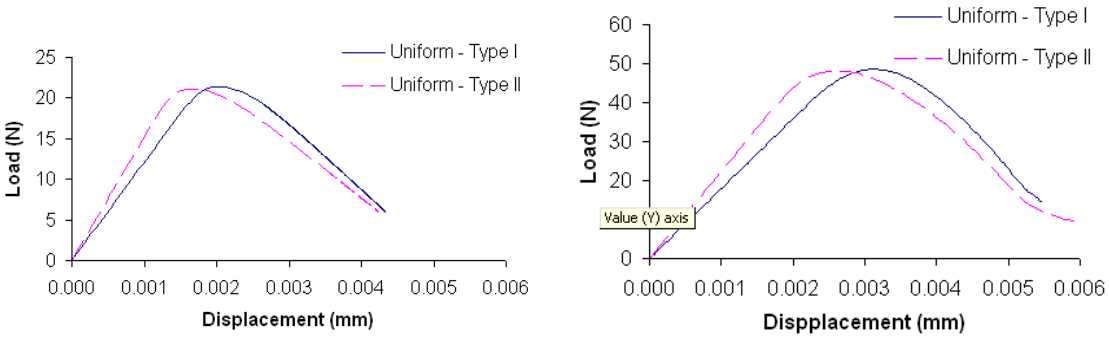

(a) 64 (1) (b) 216 (1)

Figure 6.18: Resulting different response curves due to various boundary conditions.

6.6 Discussion

A family of artificial polycrystals of increasing size is created using the Polycrystal Generator. The samples are then analyzed with and without cohesive grain boundaries using various internal property assignments. The influence of the different internal variations is observed.

First, the influence of variation in grain properties is investigated for linear, elastic isotropic grains. For a $\pm 10\%$ variation in E_{gr}, E_{eff} varies by 0.6% for samples without cohesive grain boundaries. The samples with cohesive grain boundaries show a maximum of 0.4% variation in E_{eff} while Δ_{soft} varies between 1% and 3%. The specific grain geometry and distribution of E_{gr} affected a given sample's ability to accommodate the full 0.006 mm applied displacement. The sensitivity to specific geometry and distribution of properties is most prevalent in the 64 grain samples. This indicates that a sample this small is too sensitive to the specific internal variation to be utilized reliably across a range of instances.

Next, plasticity models are utilized with variation in the orientations assigned to each grain. For the samples analyzed without cohesive grain boundaries, ge-

ometry does not influence the Δ_{yld} observed. The 64 grain samples are analyzed using two different random instances of orientation, but again this shows no affect on when plasticity is triggered. As noted above, the 64 grain samples have difficulty accommodating the entire applied displacement. The specific 64 grain geometry and distribution of orientations does affect how much the sample is able to stretch. However, all larger samples are able to reach the full applied displacement. Geometry does show an effect on the samples analyzed with cohesive grain boundaries. Variation in Δ_{yld} and Δ_{soft} are seen between different samples of the same grain size. These samples show global softening which varies greatly between the constant and distributed orientation analyses. Differences in the shape of the peak and softening slope are also seen. In several instances the analyses are unable to reach the applied displacement. This may be due to competition between plasticity and grain boundary softening within the sample.

Variation is also added to the grain boundary properties. Adding variation in the grain boundary parameters allows the 64 grain samples to accommodate additional strain. The variation modifies the post-softening portion of the response curve for larger samples without consistently allowing for the sample to accommodate additional strain. All samples experienced a decrease in E_{eff} ranging from 0.03% to 0.14% due to the decrease in the peak traction of the grain boundaries.

Finally, the boundary conditions utilized are investigated. Two sets of constraints are defined to represent the two extremes of uniaxial tension and full tri-axial stress. Up to this point, all analyses are conducted under Type I, or uniaxial tension, boundary conditions. The additional constraint from Type II results in increasing the E_{eff} of all samples, with and without cohesive grain boundaries. For samples without cohesive grain boundaries, the increased constraint does not

affect a sample's ability to accommodate additional strain. Samples that are not able to accommodate the entire applied displacement still suffer non-convergence at the same displacement. Some samples with cohesive grain boundaries are able to accommodate additional stretch under the Type II constraint. Under Type I boundary conditions, the E_{eff} of samples with cohesive grain boundaries is greatly reduced. Type II boundary conditions raises the E_{eff} to within half of one percent of the average E_{gr}. Using additional constraints to emulate a polycrystal at the surface of a specimen self-corrects for the softening effect of the non-initially rigid cohesive grain boundaries. This negates the need to investigate artificially increasing the E_{gr} values assigned in order to reproduce the expected E_{eff}.

Several analyses were unable to complete within the allotted 10 wall clock days of compute time. In these instances, the convergence rate slowed to a point that even given an infinite amount of time the analysis would not complete. A select few analyses may have benefited from further partitioning but this is not a guarantee that they would have been able to reach completion within the allotted time.

The analyses discussed here can be applied to the questions posed at the beginning of Chapter 5. At the end of the previous chapter the 64 cubical grain sample showed that it could be used as an RVE since the effective response of the sample showed minimal deviation due to internal variation. While in many instances the artificial 64 grain polycrystal samples used in this chapter showed minimal impact of internal variation, they also showed an inability to accommodate the applied 3% strain. For analyses including plasticity or cohesive grain boundaries under enough strain to reach yielding or softening, the 64 grain size is unreliable. Therefore, a minimum RVE of 216 grains is recommended. As grain geometry and constitutive model complexity increase to attempt to capture more reality within

a sample the computational requirements also increase. The 512 and 1,000 grain samples frequently exceeded the time allotment. It is recommended that samples of this size be used only when required and investigations of smaller samples have been exhausted.

Chapter 7

3D Polycrystal Simulations Under Cyclic Loading

Up to this point in this thesis, all analyses utilize monotonic loading for the purpose of studying how different modeling parameters affect each sample's overall response and crack nucleation through grain boundary decohesion. However, the material of interest is an aluminum alloy, AA 7075, used in aircraft. The loading history for any aircraft component is cyclic, resulting in possible fatigue crack nucleation and propagation. Therefore, additional analyses are conducted on the artificial polycrystal samples under cyclic loading to study fatigue crack nucleation. The feasibility of conducting such analyses and the computational requirements for conducting an adequate number of cycles are discussed. Also, the constitutive models' current implementations are evaluated for their ability to capture fatigue behavior.

7.1 Setup

Samples are selected from the family of artificial polycrystal samples generated in Chapter 6. The selected 216(1) and 512(1) grain geometries are shown in Figure 7.1. The samples are assigned grain material and grain boundary properties from Table 7.1. Finally, the samples are loaded following the cyclic load history shown in Figure 7.2 with the boundary conditions shown in Figure 7.3. The cyclic loading consists of twenty cycles with R=0.1.

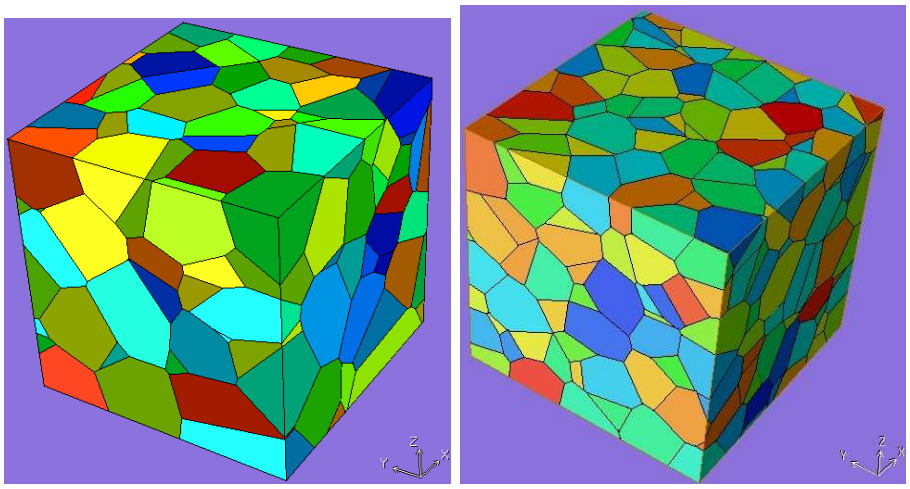

(a) 216 grains (b) 512 grains

Figure 7.1: Individual grain geometries subjected to fatigue loading.

Table 7.1: Grain Material and Grain Boundary Property Values

Rate-Independent Crystal Clasticity Grain Material				
E (MPa)	ν	g_0 (MPa)	h_0 (MPa)	(ϕ, θ, ω)
90,000±10%	0.34	228±10%	400±10%	(ϕ, θ, ω)

Bi-Linear CCZM				
k_0	τ_p	δ_n^c	δ_t^c	β
8,400±10% GPa	84±10% MPa	0.001 mm	0.001 mm	1.0

7.2 Observations

The artificial polycrystal samples can require up to 64 processors for 10 days of wall clock time to conduct analyses under monotonic loading. The current loading does not use the high strain previously applied, but does require the entire sample to undergo unloading, which causes difficulty for 2D fatigue analyses [3]. Most of the 2D samples show stress concentrations where multiple grain boundaries intersect with the geometry boundaries; grains slide relative to one another during

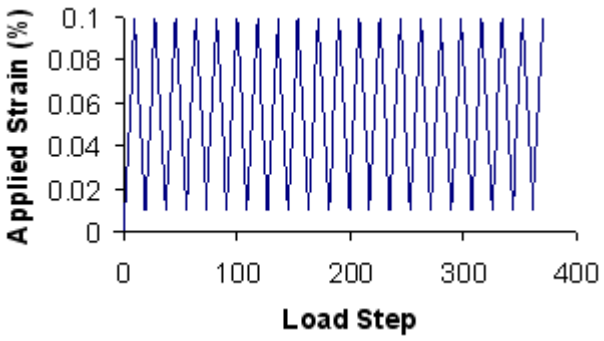

Figure 7.2: Fatigue Loading History.

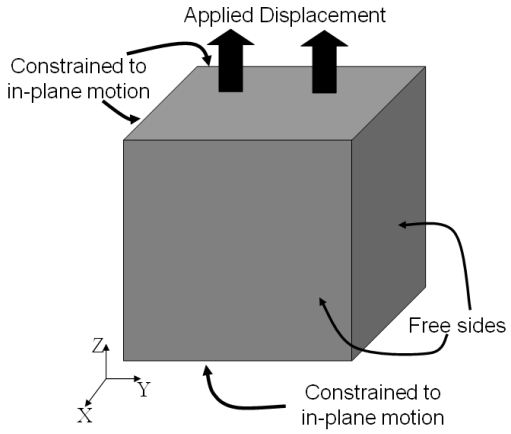

Figure 7.3: Boundary conditions applied to fatigue analyses.

Table 7.2: Computational Time for Fatigue Analyses

Sample Size	No. DOFs	No. Processors	Time (mins)
216	581,454	8	797.65
512	1,563,420	32	817.82

loading and must fit back together during unloading. Table 7.2 shows the sample size, number of DOF for linear order element, number of processors used, and computational time required to complete the twenty cycles. The computational times shown are significantly shorter than the times required to monotonically load the samples to 0.006 mm. This is likely due to the reduced strain level and the samples not undergoing global softening. Given the computational resources available, many more cycles can be conducted.

Each sample loaded under cyclic loading shows similar damage behavior. As a measure of damage, the maximum grain boundary opening, λ, present anywhere in the sample at each peak load is determined. Figures 7.4 and 7.5 show the maximum λ per load cycle for each sample. For each sample, grain boundary softening is detected during the first loading. Therefore, when the sample is first unloaded the softened CCZMs unload back to the origin. Upon reloading, any points that previously softened now follow a weakened stiffness path back to the CCZM curve. This results in additional damage accumulating during subsequent reloading.

The graphs of λ show a plateau after several cycles. For the 216 grain sample very little increase in λ is seen after the tenth cycle. The value of λ does continue to increase but very slowly. For the 512 grain sample, very little increase is seen after the eighth cycle. Figures 7.6 and 7.7 show the λ contours for the first and last peak load for each sample. The internal grain boundary opening is shown by

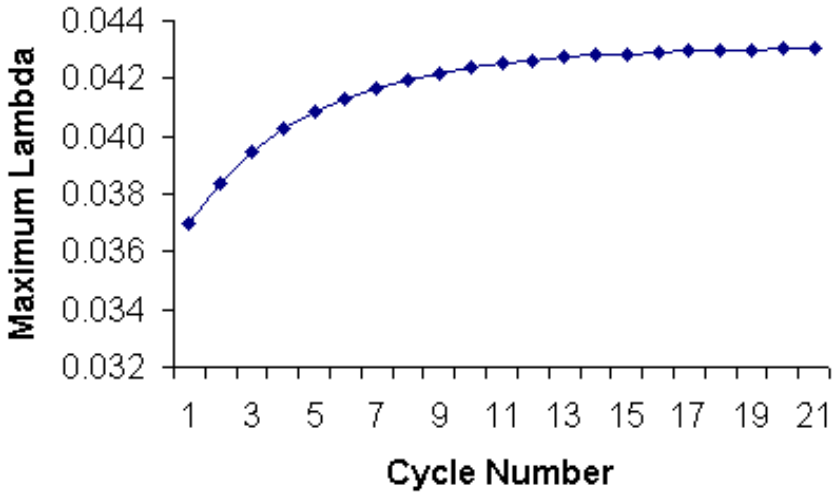

Figure 7.4: Maximum λ per load cycle for the 216 grain sample.

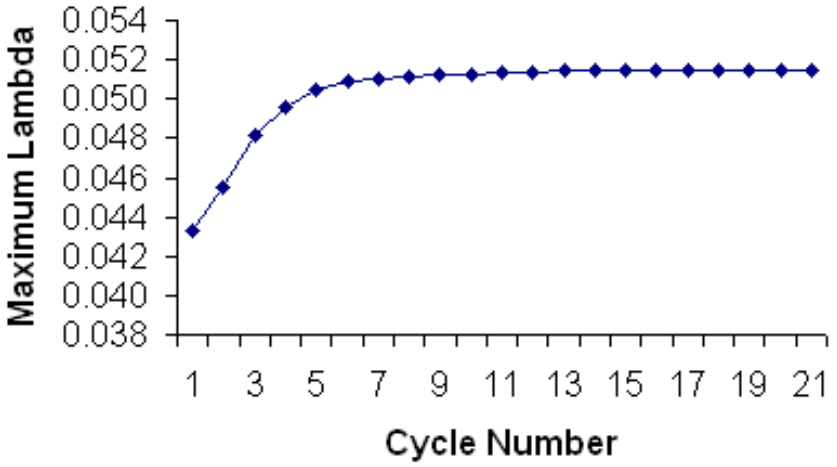

Figure 7.5: Maximum λ per load cycle for the 512 grain sample.

reducing contours below $\lambda = 0.01$ to being transparent. An increase in λ values can be seen between the first and last peak load. However, enough opening has not occurred to begin to localize the opening and define a through crack that could lead to failure.

7.3 Discussion

The previous chapter discussed the parametric study conducted on 3D polycrystal samples under monotonic loading. Based on the conclusions of the parametric study the 216 and 512 grain samples are selected to be analyzed under cyclic loading. Each sample is cycled twenty times. The maximum λ within the sample is determined to quantify the accumulation of damage for each cycle.

At first glance, it appears that fatigue crack nucleation is captured. The unloading and reloading path of the CCZM allows additional damage to accumulate as the samples are cycled. However, what is being observed is more accurately described as "shakedown" through cyclic loading. Ultimately, the samples find equilibrium states at which no additional damage occurs no matter how many additional cycles are applied. With true fatigue, additional damage continues to accumulate.

Variations of the unloading/reloading portions of the CCZM exist which are designed to capture fatigue behavior at the continuum scale. One type of variation is a damaged-based model which, for example, adds degradation during reloading as discussed in [69] and [70]. Additional variables are used to control the amount of degradation experienced during each reloading. Additional work is ongoing to implement modified versions of the 3D bi-linear and exponential CCZM that include this degradation.

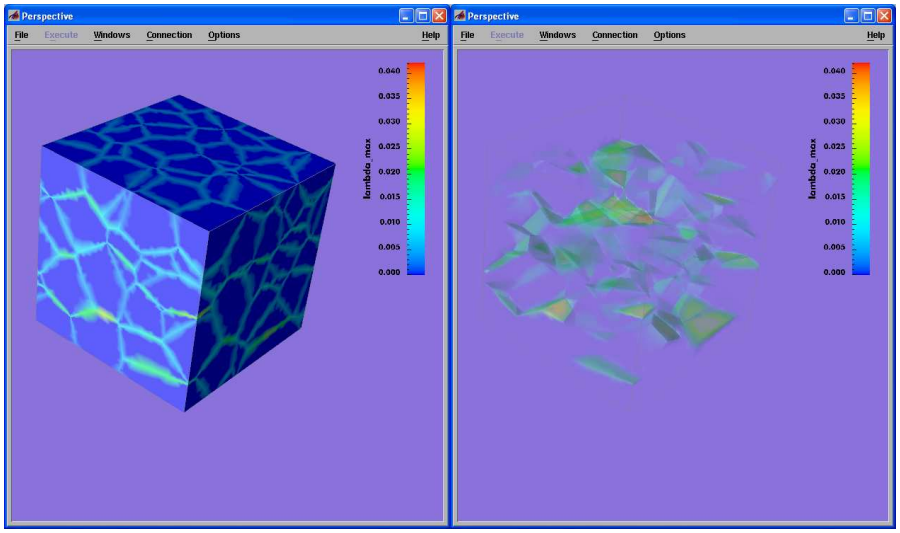

(a) 216-grains, first peak load

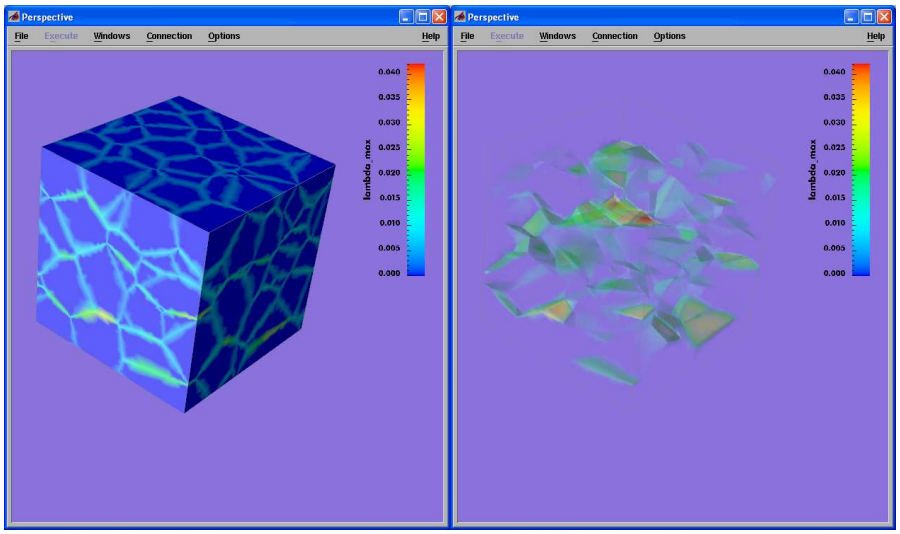

(b) 216-grains, last peak load

Figure 7.6: λ contours for the 216-grain samples loaded under fatigue.

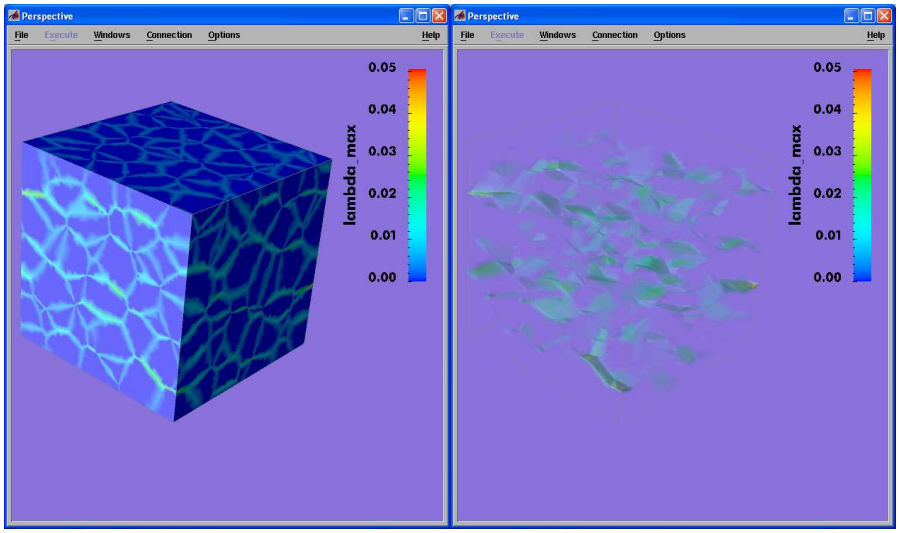

(a) 512-grains, first peak load

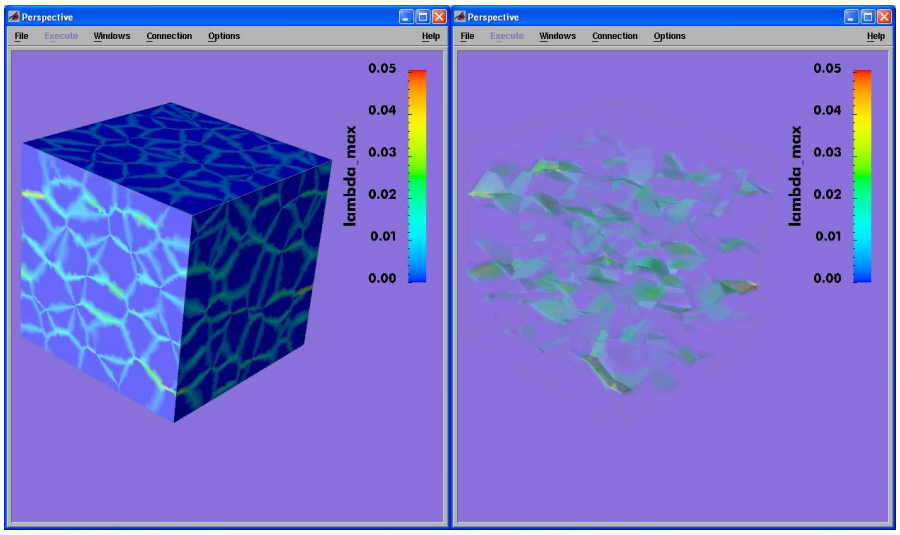

(b) 512-grains, last peak load

Figure 7.7: λ contours for the 512-grain samples loaded under fatigue.

Chapter 8

Conclusions

The goal of the research described in this thesis is to move beyond curve fitting and phenomenological "laws" for understanding, predicting, and simulating fatigue crack nucleation and subsequent propagation. Ultimately, this research aims to be able to explain the physics at work that leads to the intergranular cracks as seen in Figure 8.1 through polycrystal simulations such as shown in Figure 8.2. The contribution of the current research is to conduct parametric studies in 3D to set a baseline for future analyses. This work tackles:

- determining size requirements of a representative volume element (RVE);
- understanding the computational requirements for detailed analyses at the polycrystal-scale;
- understanding constitutive models at the polycrystal scale;
- developing effective methods for managing and post-processing large amounts of 3D data.

To conduct this research, a set of tools has been developed and compiled for generating, visualizing, and post-processing polycrystal samples and conducting analyses of grain boundary decohesion under monotonic and cyclic loading. The tools generated and assembled are successfully able to:

- generate simplified but non-regular, non-repeating (artificial) polycrystal geometries which can be successfully meshed;
- store geometry and mesh information within an off-the-shelf relational database;

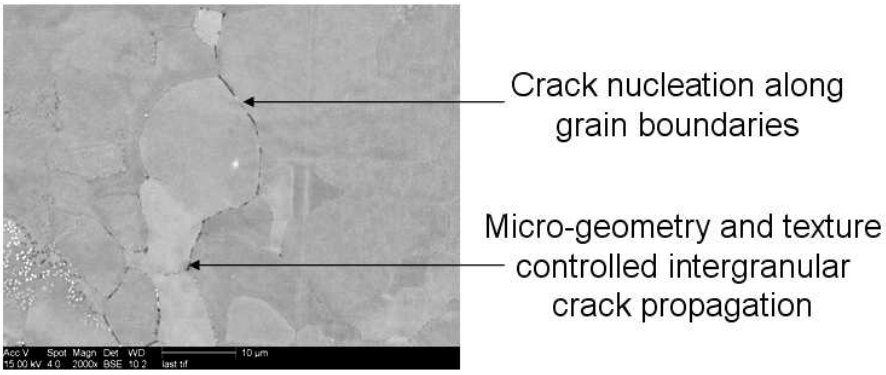

Figure 8.1: Experimentally observed intergranular fatigue cracking in 7050-T6 (Photo courtesy of Alcoa, Inc).

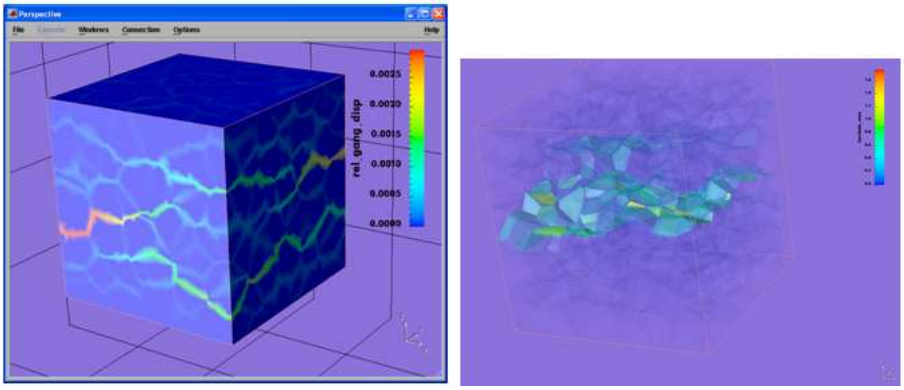

(a) Simulation of nucleation/localization

(b) Damaged grain boundaries

Figure 8.2: 3D polycrystal simulation of grain boundary decohesion.

- assign material properties to grains and grain boundaries and assign boundary conditions;
- conduct serial and parallel finite element analyses;
- import results data into the database for post-processing and visualization;
- facilitate loosely-coupled multi-scale analyses.

The tools described above are assembled into components that complete a single task required for generating, analyzing, and post-processing 3D polycrystal samples. The components are also implemented with Web service interfaces so they may be easily accessed by other researchers within the Cornell Fracture Group and collaborators world-wide. To guide a user through generating a polycrystal sample and conducting a multi-scale analysis, the Web service interfaces are connected to a client program, the Polycrystal Generator. An example of using the Polycrystal Generator to generate, mesh, and store a model of a particle on a grain boundary is shown in Chapter 4. The model is used to demonstrate how a loosely-coupled multi-scale analysis can be conducted. The OFEMD component, also available through the Polycrystal Generator, is able to access the model and conducts molecular dynamics (MD) analyses to determine the cohesive responses of the interfaces within the model. Parameters for bi-linear coupled cohesive zone models (CCZM) are determined from the MD results and utilized to conducted a finite element (FE) analysis of the model.

In Chapter 5 cubical grain samples are used to verify material model implementation and test new capabilities. Investigations of internal variations through material parameters, show that for polycrystal samples with cubical grains a 64 cube sample can serve as an RVE. The 64 cube sample is also used to determine

the effects of mesh refinement and element order as well as to determine optimal computational solution parametersThe family of cubical polycrystals is studied to anticipate sample size-related problems. Increasing the sample size increases the number of processors used and analysis time needed. The 1,000 cubical grain sample with linear, elastic grains and cohesive grain boundaries is analyzed using four processors in about 10 days. Using a more complex material model leads to longer computational times, while increasing geometric complexity requires a finer mesh resolution and thus more memory. It should be noted that the polycrystal samples analyzed in this thesis underwent 1.2% to 3% strain. Applying smaller strains will result in shorter computational times.

A parametric study conducted on artificial polycrystals with irregular grain shapes investigates how different sized polycrystal samples respond to internal variation in Chapter 6. First variation due to grain parameters is investigated. For a $\pm 10\%$ variation in E_{gr}, the resulting E_{eff} varies less than 0.6% from the mean value of E_{gr} for samples without cohesive grain boundaries. The introduction of cohesive grain boundaries with uniform parameters results in reducing E_{eff} by 20%. The variation in E_{eff} is less than 0.4% and the variation in Δ_{soft} is between 1% and 3%. Next, the influence of grain orientation is investigated. For samples analyzed with rate-independent crystal plastic grains and without cohesive grain boundaries, varying grain orientation did not influence Δ_{yld}. The amount of displacement applied to the 64 grain sample before encounter non-convergence is very sensitive to the specific instance of grain orientations. This influences the 64 grain sample's usefulness as an RVE. Analyses are also conducted with cohesive grain boundaries. Variation in grain orientation results in altering the global softening response observed. Next, variation is introduced to the cohesive

grain boundary parameters. All samples experience a decrease in E_{eff} of 0.03% to 0.14% due to the decrease in peak traction. Finally, two sets of boundary conditions are examined. All previous results are reported for the Type I, or uniaxial tension, boundary conditions. Previous results are compared to Type II, triaxial tension, boundary conditions. The additional constrain of Type II results in increasing E_{eff} approximately 50% as well as a 33% increase in Δ_{yld} for samples with rate-independent crystal plastic grains. The increase in E_{eff} for samples with cohesive grain boundaries negates the reduction caused by using CCZMs with initial elastic responses.

These results, taken as a whole, answer questions posed in Chapter 5 concerning the minimum size of an RVE and the maximum size of a polycrystal that can reasonably be analyzed. Of the sample sizes studied, the 216 grain sample is the smallest sample able to reliably provide enough internal variation to accommodate the applied boundary conditions under monotonic loading. The 512 and 1000 grain samples frequently required the maximum allotted computation time of 10 days. The larger samples should be utilized only after smaller sample sizes are exhausted.

The cyclic loading simulations described in Chapter 7 show that cyclic loading can be carried out on 3D polycrystal samples incorporating crystal plasticity and grain boundary decohesion. This is an important step forward for polycrystal-scale analyses. The polycrystal results show that the crystal plasticity model is able to handle cyclic loading and unloading. The bi-linear coupled cohesive zone mode (CCZM) also performs as designed under cyclic loading. The results of conducting such a simulation show that the unloading/reloading of the CCZM captures a phenomenon known as “shakedown” rather than fatigue. The grains and grain boundaries relaxed from their initial state to find an equilibrium state that allows

the cyclic loading to continue without causing further damage. Modifications of the CCZM are being implemented to allow for cyclic degradation. These modifications are currently used in traditional continuum applications. Investigations of their ability to work within a polycrystal analysis are being conducted.

With the tools described in this thesis in place and tested, additional features can be introduced to the grain geometry and constitutive models to increase the level of reality represented. Additional work is being carried out by the Cornell Fracture Group and collaborators to improve the reality of the geometry while still being practical to mesh and analyze. Geometries being generated by Rollett, *et al.* (as described in Chapter 3), which show elongation of grains along preferred directions and non-convexity, are able to be successfully meshed and initial analyses completed. The Voronoi geometries are being modified to include sub-grain particles, which have been shown in experiments to be common nucleation site for fatigue cracks. Exploration of alternative constitutive models, including the cyclicly degrading CCZM of Ural, et al. [69, 70], is being conducted to find appropriate models which truly capture fatigue rather than shakedown. Additional work is continuing to analyze these more complex and realistic models.

With these additions to the current tools and capabilities, more realistic polycrystal samples can be generated and analyzed. The continuation of this research will lead to a better understanding of when, where, and why fatigue cracks nucleate in metallic polycrystals. By identifying and understanding initiation sites in a polycrystal and in general how a polycrystal responds, possible changes to manufacturing processes, flaw detection, and repair and replacement guidelines can be made intelligently. Improvement to these areas can lead to improved life prediction, increased life spans of current implementations, and better materials

in the future.

Besides stand alone uses, the components developed and discussed in this thesis can be used as part of multi-scale investigations. As described in Chapter 4, the polycrystal capabilities can be used in a simulation loop with analyses at other length scales. An analysis of a macro scale component can be enhanced by loosely coupling polycrystal scale analyses to "hot spots" identified. This coupling re-introduces the micro-scale statistics and variability lost by using continuum scale constitutive models which smear out smaller scale features such as grain boundaries, grain orientations, and particles. In turn, loosely coupling polycrystal and atomic scale analyses can give insight into polycrystal scale parameters which can not currently be extracted from experiments. Again, these applications lead to higher fidelity analyses and better understanding of fatigue crack nucleation.

Appendix A

Simulations on Statistical

Representations of Polycrystals using

Franc2D/L

Polycrystal User's Guide, Version 2.0
February, 2006

Jeff Bozek, Erin Iesulauro and Ketan Dohdia

Cornell University, Ithaca, New York

Introduction

The following "Polycrystal User's Guide" is based primarily on graduate research completed by Iesulauro [3] and Dohdia [4]. This manual will effectively guide the reader through the creation of and simulation of polycrystal models in FRANC2D/L. These cited sources and also James [32] are recommended to gain a better understanding of polycrystal and interface modeling in FRANC2D/L .

The example material system used in this manual is that of AA 7075-T6, before any mechanical processing [3]. A meso-scale representation is created on which to perform simulations and to study microstructural influences on crack nucleation and propagation. The process of creating a meso-scale model with discrete grains represented is decomposed into three stages: creating a grain geometry, assigning of material model and properties for the grains, and determination of how to represent the grain boundaries to allow the initiation of cracks.

Outline of Procedure

Grain Geometry

The representation of the grain geometry could either be done to match a single observed polycrystal sample or to represent the average geometry seen over many samples. It was decided here to represent the geometry in an average sense. The polycrystal samples generated statistically match observation in terms of quantities such as average grain size and aspect ratio. However, samples won't exactly match any observed geometry. For this work, the Voronoi tessellation technique was chosen as the method by which to create the grain geometries.

Voronoi Tessellation

Voronoi tessellation begins from a random distribution of nuclei. Lines are generated connecting a nucleus to its nearest neighbors. These lines are then perpendicularly bisected to create the edges of a polygon. Each nucleus then defines a polygon within which all points are closer to the nucleus than to any other. This process best represents the initial forming of the grains from dendrite sites, within a melt with isotropic growth rates [36].

This particular choice represents the initial polycrystal structure or annealed structure well. However, Voronoi tessellations do not capture the distortion of the grains due to mechanical processing, such as rolling. Since this work was done in 2D it was determined that this would be a good tessellation with which to test modeling choices and software capabilities. Ongoing work is looking at modifications to the Voronoi tessellation as well as other tessellation methods that will better represent the rolled grain structure [71, 72].

Current modeling has been expanded to consider the discrete modeling of sub-grain sized particles. Particles well below the size of the grains are considered to be smeared out and represented through the grain material properties.

Grain Material

Once the geometry is in place, material properties are assigned to each grain. Current material model options include elastic, isotropic; elastic, orthotropic; elastic-plastic, isotropic; and elastic-plastic, orthotropic. Details concerning the plasticity implementation can be found in James [32]. See the FRANC2D/L User's Guide [25] for the necessary parameters for defining any of these material models. For the chosen material model, each grain is assigned the appropriate parameters.

Grain Boundaries

In a polycrystal, there are many mechanisms that can lead to the nucleation of micro-cracks. For example, fatigue can lead to the formation of slip bands within grains, which can lead to stage I shear cracks. Also, a corrosive environment can lead to the failure of grain boundaries due to oxygen embrittlement. The present polycrystal simulations focus on grain boundary decohesion as the primary source of localized damage. To allow decohesion to occur naturally, grain boundaries are modeled using cohesive zone models. The following discusses the theory and implementation of cohesive zone models.

Grain Boundary Property Assignment

Grain boundaries naturally arise in polycrystals due to the lattice mismatch between adjacent grains. This region of disordered atoms behaves differently than the

regular lattices of the adjacent grains. Therefore, we describe the grain boundary with its own constitutive relationship, separate from the bulk grain material. A cohesive zone model has been chosen for this purpose to describe the strength and toughness of the grain boundaries. The cohesive zone model also serves as a criterion for nucleation of intergranular cracks. The grain boundaries are allowed to decohere after reaching a critical normal, shear, or combined transmitted traction, thus gradually nucleating an intergranular crack. Once a critical opening/sliding is reached, a true crack has formed. An advantage of using such a model is that initial cracks are not arbitrarily introduced at the beginning of a simulation. Instead, cracks naturally occur due to the heterogeneous stress field throughout the sample caused by the geometry and variations in properties. Cracking first begins along grain boundaries in areas with the highest stress concentrations.

Cohesive Zone Model

In theory, the stress at a crack tip in a linear and elastic material is singular. However, in practice, materials, especially metals, have a yield stress at which they begin to deform plastically negating the singularity. This leads to the area around the crack tip called the crack tip plastic zone. The stress in the plastic zone can only reach the current yield stress. Several methods have been developed to determine the extent of the plastic zone. These include Irwin's plastic zone correction [38] and the strip yield models developed first by Dugdale [9] and Barenblatt [10].

Dugdale considered a fictitious crack tip a distance ahead of the actual crack tip. The fictitious tip carries a compressive force equal to the yield stress that tends to close the crack. An application of this approach by [39] is the fictitious crack

model or the cohesive zone model. The cohesive zone model (CZM) assumes that the compressive force applied in the plastic zone follows a traction-displacement relationship. It is also assumed that this traction-displacement behavior can be considered a material property [41, 42].

In the present case, the damage represented by the displacement softening portion of the CZM is used to describe the decohesion of the grain boundaries leading to crack nucleation. Also, the area under the traction-displacement curve represents the critical energy release rate, Gc, to nucleate a crack. The implementations available in FRANC2D/L [25], includes independent normal and shear cohesive models as well as a coupled model. The normal and shear models evaluate the transmitted traction independently of each other. In other words, the transmitted normal does not influence the amount of shear and vice versa. The coupled cohesive zone model (CCZM) was adapted from a model developed by Tvergaard and Hutchinson [7], where the normal and shear components of the traction and displacement are combined into single measures, τ and λ, respectively (Figure A.1), so that responses are coupled.

Coupled Cohesive Zone Model

With the segregated, normal and shear, models, problems can arise under mixed-mode loading. For example, since the shear and normal operate independently, it is possible for shear forces to be transmitted across an interface while no normal traction is being transmitted due to large opening. This of course is physically incorrect. Since mixed mode loading is to be expected in polycrystal samples due to inclined grain boundaries, the following coupled cohesive zone model (CCZM) is implemented in the FRANC2D/L polycrystal simulations.

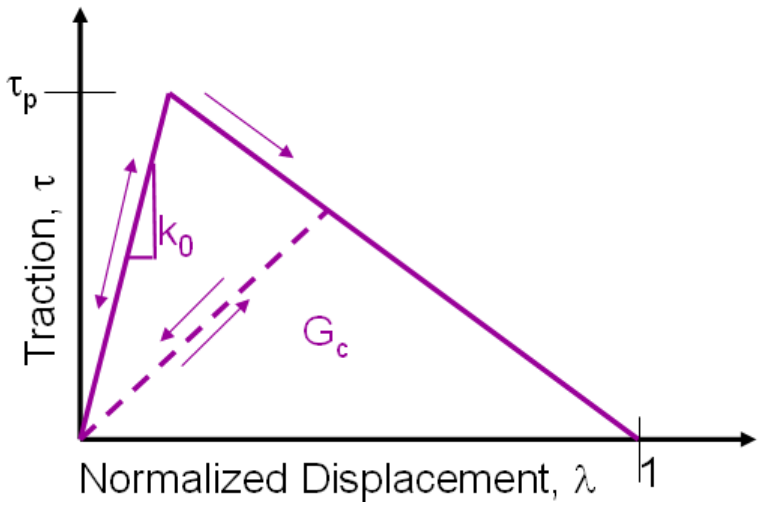

Figure A.1: Coupled cohesive zone model

The CCZM begins from a traction potential, Φ.

$$\Phi(\delta_n, \delta_t) = \delta_n^c \int_\lambda \tau(\lambda')\mathrm{d}\lambda' \tag{A.1}$$

Φ is a function of the relative normal, δ_n, and tangential, δ_t, displacements between the faces of the grain boundary. λ is a non-dimensional separation measure for the relative opening and sliding defined by Eqn. A.2. The opening and sliding displacements, δ_n and δ_t, are normalized to the relative critical displacement values, δ_n^c and δ_t^c, at which the separation is considered a true crack, or traction free surface, in pure Mode I and pure Mode II, respectively. β is a parameter that determines the ratio of shear to normal traction. When the value of λ reaches 1 this indicates the complete decohesion of the grain boundary and the formation of a true crack.

$$\lambda = \left[\left(\frac{\delta_n}{\delta_n^c} \right)^2 + \beta \left(\frac{\delta_t}{\delta_t^c} \right)^2 \right]^{1/2} \tag{A.2}$$

For a given relative displacement between two grains the combined traction, τ, transmitted across the grain boundary can be determined from the CCZM. The combined traction can then be decomposed into normal, T_n, and shear, T_t, com-

ponents by differentiating Φ with respect to δ_n and δ_t according to Eqn. A.3 and A.4 respectively.

$$T_n = \frac{\partial \Phi}{\partial \delta_n} = \frac{\tau(\lambda)}{\lambda}\frac{\delta_n}{\delta_n^c} \tag{A.3}$$

$$T_t = \frac{\partial \Phi}{\partial \delta_t} = \beta\frac{\tau\left(\lambda\right)}{\lambda}\frac{\delta_n^c}{\delta_t^c}\frac{\delta_t}{\delta_t^c} \tag{A.4}$$

The CCZM parameters have the following physical implications. This model has an initial elastic response which artificially introduces additional compliance to the sample. To minimize this unwanted artifact, k_0 must be set very high compared to E/h, where E is the Young's modulus of the grains and h is an average grain dimension. However, setting k_0 too high leads to numerical instability. The coupled value of τ_p relates to the peak normal strength, T_p^n, under pure Model I and peak shear strength, T_p^t, under pure Mode II according to Eqn. A.5 and Eqn. A.6 respectively. Whether plane stress or plane strain is assumed will vary the value of the coupled peak traction, τ_p, relative to the bulk yield stress. For plain strain, τ_p is considered to be three to five times the yield stress. For plane stress, the value is only one to one and a half times the yield stress. For the parametric studies contained in Iesulauro [3], the value of τ_p is varied to observe the influence of the relative values. After the peak traction is reached, atomic bonds begin to break allowing the faces to separate. This post-peak portion of the traction-displacement curve simulates the softening of the grain boundary. At a specific effective separation distance, the opposing faces no longer exert attractive forces on each other, resulting in a true crack. This corresponds to

$$\tau_p = T_p^n \tag{A.5}$$

$$\tau_p = \frac{\delta_n^c}{\beta\delta_t^c}T_p^t \tag{A.6}$$

(a) Unloading according to the initial stiffness.

(b) Unloading back to the origin.

Figure A.2: Possible unloading paths for the cohesive zone model.

Unloading of the Coupled Cohesive Zone Model

Since cyclic loading conditions will be used in the polycrystal simulations, the unloading of the CCZM must be implemented. Two possible unloading paths considered were unloading according to the initial stiffness and unloading back to the origin. These two paths are shown in Figure A.2. Both physical implications of the unloading paths and numerical difficulties were considered before choosing to unload to the origin.

Unloading according to the initial stiffness allows for permanent plastic deformation in the grain boundary to occur. This reflects such theories as crack closure. However, this approach causes implementation problems. When the FRANC2D/L software calculates the stiffness matrix for the model, a tangent stiffness is determined for each element. For the interface elements used along grain boundaries the secant stiffness is calculated instead. The solution technique used requires the stiffness matrix to be positive definite. Therefore the negative slope of the softening portion of the curve is not acceptable. To compensate for this, the secant stiffness is calculated instead, which still captures the softening of the stiffness matrix. Keeping this in mind, it follows that unloading according to the initial stiffness would result in an increase in stiffness of the interface upon

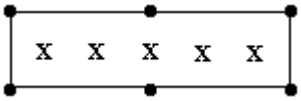

Figure A.3: 6-noded interface elements and location of integration points.

unloading and reloading.

Unloading back to the origin does result in a fully closed interface. However, the interface instead sees damage by reloading along the unloading path which has a lower value than k_0. This also removes several difficulties that would be experienced in implementation of the other unloading model. For this reason unloading back to the origin was implemented.

Interface Elements

A convenient method for implementing the CZMs is through zero thickness interface or joint elements. The 6-noded interface element (Figure A.3) implemented here creates traction forces as a function of the displacement prescribed by the CZM. The displaced location of the centerline of the element is determined from the nodal positions. The relative displacements of node pairs are determined and interpolated to the five Gauss integration points. At each of the integration points the traction is then computed from the CZM specified and integrated to determine the work equivalent nodal loads. The stiffness can also be determined from the CZM based on the relative displacement [43, 44]. A tutorial for using interface elements in FRANC2D/L simulations is included in Appendix A of Iesulauro [3] or in the FRANC2D/L User's Guide version 2.0 [25].

Creating Statistical Samples of Polycrystals for Franc2D/L

The *.inp file for FRANC2D/L contains mesh information as well as material definitions and assignments to each element. Traditionally, creating a *.inp is done using CASCA. This is an independent modeling and meshing program. A description of this tool is available in the FRANC2D and FRANC2D/L Manuals. If unfamiliar with FRANC2D or FRANC2D/L , the reader should read James [25] and complete a FRANC2D/L tutorial prior to attempting polycrystal models.

The statistical creation of polycrystal models and the corresponding *.inp, however, is not done through CASCA. Instead, a series of Matlab functions were created to statistically generate polycrystal geometries as well as distributions of particles and material properties. In order to produce polycrystal models by the following techniques, one should already have a basic understanding of Matlab.

This following section outlines the steps for creating a polycrystal sample and the corresponding *.inp file. These steps are to be followed in sequence by the user. The next section contains a tutorial, which assists the reader in using the commands for creating a polycrystal model. The entire set of Matlab algorithms must be downloaded from the Cornell Fractures Group website before completing the tutorials.

Grain Geometry

First, the size of the polycrystal, number of grains, and grain geometries are defined. Grain geometries are determined using a Voronoi tessellation as described previously. The process of creating the tessellation has been compiled into a single

Matlab script, **DM_tess**.

DM_tess('jobname',dim,num,seed)

This script requires four input functions from the user. '**jobname**' is a string indicating the job name to be assigned by the user and corresponds to the name of the .inp file that will eventually be implemented in FRANC2D/L . **DM_tess** calls a Fortran program, Vor.f, that creates the tessellation. This program produces a square sample. **Dim** is the length of a side of the square to be tessellated. Vor.f requires either the number of grains to be created or the average grain size. **DM_tess** is currently set to accept the number of grains, **num**. FRANC2D/L is capable of reading up to 500 material definitions. This includes grain materials as well as cohesive zone model definitions. This should be taken into account when determining the number of grains to create. Finally, a random number **seed** is needed.

The output is the file *jobname.tess*. This contains the tessellation information. To view the tessellation use **DM_plottess('jobname')**. There are also several intermediate files that are generated but are not necessary for future steps.

Particle Insertion

Polycrystal samples can be created with or without the inclusion of particles. The following describes the process for inserting particle geometries, distributed throughout the polycrystal. To insert particles in Matlab, type:

DM_ParticleList('jobname',n_parts,n_sides,ratio,threshold,
subdivide_ratio_max,subdivide_ratio_min,seed)

Again **jobname** is used for reading the *.tess file created and for naming output files; therefore, the user should use the same jobname as specified in **DM_tess**.

N_parts is the number of particles you wish to have. Each particle will be represented as a polygon, **N_sides** is the number of sides to be used for the polygons. **Ratio** determines the relative size of the particles to the size of the grains. The rest of the variables are used for determining overlap of particles and grain boundaries and for preparing the particles to be meshed. **Threshold** is the minimum distance allowed between a particle and a grain boundary. If a particle is closer than the threshold value then the particle is moved such that it will touch the grain boundary. This value is also used to determine the minimum distance between particles. If particles are too close they will be joined. The **subdivide_ratios** are used for subdividing the particle edges for meshing. The larger the subdivide ratios the denser the mesh. Finally a random number **seed** is also needed.

The outputs corresponding to this particle insertion are *jobname.sub*, a list of subdivision of particle boundaries for meshing, and *jobname.par*, a list of the particles. When the function concludes it will display the tessellation with the particles in a Matlab figure window.

Defining Material Properties

Once the polycrystal geometry and particles have been defined the material properties of the grains and particles must be assigned. Properties are assigned in a statistical sense. The particles are modeled as isotropic linear elastic, while four material models are available for grains: elastic-isotropic, elastic-orthotropic, von Mises plasticity, and Hill plasticity. The material properties are read from four separate text files: *properties.txt, partprop.txt, betalist.txt,* and *hardcurve.txt. Properties.txt* and *partprop.txt* define the distribution of properties to be assigned to the grains and particles respectively.

Properties.txt
E_1: Mean Range Std. Dev.
E_2: Mean Range
E_3: Mean Range
$\nu_{12}\nu_{23}\nu_{31}$
Thickness
Density
K_{IC}: Mean Range Std. Dev.
K_{IC_Inf}
σ_{Y1}: Mean Range
σ_{Y2}: Mean Range
σ_{Y3}: Mean Range

Partprop.txt
E: Mean Range
ν
Thickness
Density
K_{IC}: Mean Range

Betalist.txt is a file listing the distributions of material angles to be used for assigning lattice angles to the grains. The file lists the angles from the global X-axis to the X1-axis for each grain. *Hardcurve.txt* is used to define hardening curves for von Mises materials.

Betalist.txt
β_1
β_2
...
β_N

Hardcurve.txt
σ_Y σ_U Step-size

Meshing

After the material properties have been defined the model can be meshed. Meshing routines are called from **DM_mshtess**. The **DM_mshtess** command can be ran as follows:

DM_mshtess('jobname',mat,dim,nseed,nseed2,subdiv_ratio)

Again, **jobname** is the name given to previous output files that **DM_mshtess** will call. **Mat** is an integer that is entered to indicate the material model assigned to the grains (1-Elastic-Isotropic, 2 - Elastic-Orthotropic, 3 - von Mises, 4 - Hill). The length of one side of the square sample is again requested in **dim**. Next, 2 random number seeds must be given. Finally, if a subdivide file (*.sub) is not provided the mesh generator will use the single value specified by **subdiv_ratio**. This determines the density of the mesh, where a higher subdivision ratio creates a more dense mesh.

When meshing is conducted, the Matlab script creates several intermediate files. These files include *tess.out* and *particle.out*. The final output is an *.inp file. This file can be read by FRANC2D/L .

Defining Cohesive Zone Models

This *.inp file created at this point is readable by FRANC2D/L ; however, it does not contain any information concerning the grain boundaries or particle-grain interfaces. As discussed previously these responses are determined by CCZMs. One option is to enter this information from within FRANC2D/L , by the process outlined in Appendix A. However, if different parameters are used for each grain boundary, the more efficient option is to define the models beforehand. This is done through two additional Matlab scripts: **DM_Multiczm1** and **DM_ParicleCZM**.

DM_Multiczm1('jobname',beta)

DM_Multiczm1 appends the *jobname.inp* with parameters defining one or more cohesive zone models corresponding to ranges of misorientation between grains. To determine the ranges of properties to be assigned by **DM_multicmz1**

the file must be altered to reflect the values. **Beta** is the angle range for which each CZM to be defined will be good for. For example, if you want to use 1 CZM for all grain boundaries beta = 360. If instead beta = 5, then the first CZM will be valid for grain boundaries with a misorientation angel between 0 and 5 degrees, and the next CZM for 6 to 10 degrees, and so forth.

DM_ParticleCZM('jobname')

DM_ParticleCZM again appends *jobname.inp* with parameters defining a CZM. This cohesive zone defines the response of the particle-grain interface. The properties are read from the file *part_czm.txt*. More information about this file is contained in example 3 below.

Input *.inp File Format

The steps outlined above result in a .inp input file for FRANC2D/L that is titled *jobname.inp*. The file includes mesh information, material definitions and assignments, as well as cohesive zone definitions. The following is an example .inp file for the 16-element block shown in Figure A.4.

```
65  16   1   1
 1  2.90E+04  2.50E-01  1.00E+00  1.00E+00  1.00E+00  0.00E+00
     0.00E+00  0.00E+00  0.00E+00  0.00E+00 0.00E+00  0.00E+00
 1    1   6   1  53  52  51   2   9   7
 2    1   9   2  51  50  49   3  12  10
 3    1  12   3  49  48  62  61  60  13
 4    1  42   4   6   5  16  14  44  43
 5    1  16   5   6   7   9   8  19  17
 6    1  19   8   9  10  12  11  22  20
 7    1  22  11  12  13  60  59  58  23
 8    1  44  14  16  15  26  24  46  45
 9    1  26  15  16  17  19  18  29  27
10    1  29  18  19  20  22  21  32  30
11    1  32  21  22  23  58  57  56  33
12    1  46  24  26  25  35  34  64  47
```

```
13     1  35  25  26  27  29  28  37  36
14     1  37  28  29  30  32  31  39  38
15     1  39  31  32  33  56  55  65  40
16     1   6   4  42  41  63  54  53   1
 1     1.500000E+00  1.750000E+00
 2     1.000000E+00  1.750000E+00
 3     5.000000E-01  1.750000E+00
 4     1.750000E+00  1.500000E+00
 5     1.500000E+00  1.250000E+00
 6     1.500000E+00  1.500000E+00
 7     1.250000E+00  1.500000E+00
 8     1.000000E+00  1.250000E+00
 9     1.000000E+00  1.500000E+00
10     7.500000E-01  1.500000E+00
11     5.000000E-01  1.250000E+00
12     5.000000E-01  1.500000E+00
13     2.500000E-01  1.500000E+00
14     1.750000E+00  1.000000E+00
15     1.500000E+00  7.500000E-01
16     1.500000E+00  1.000000E+00
17     1.250000E+00  1.000000E+00
18     1.000000E+00  7.500000E-01
19     1.000000E+00  1.000000E+00
20     7.500000E-01  1.000000E+00
21     5.000000E-01  7.500000E-01
22     5.000000E-01  1.000000E+00
23     2.500000E-01  1.000000E+00
24     1.750000E+00  5.000000E-01
25     1.500000E+00  2.500000E-01
26     1.500000E+00  5.000000E-01
27     1.250000E+00  5.000000E-01
28     1.000000E+00  2.500000E-01
29     1.000000E+00  5.000000E-01
30     7.500000E-01  5.000000E-01
31     5.000000E-01  2.500000E-01
32     5.000000E-01  5.000000E-01
33     2.500000E-01  5.000000E-01
34     1.750000E+00  0.000000E+00
35     1.500000E+00  0.000000E+00
36     1.250000E+00  0.000000E+00
37     1.000000E+00  0.000000E+00
38     7.500000E-01  0.000000E+00
39     5.000000E-01  0.000000E+00
40     2.500000E-01  0.000000E+00
```

```
41      2.000000E+00  1.750000E+00
42      2.000000E+00  1.500000E+00
43      2.000000E+00  1.250000E+00
44      2.000000E+00  1.000000E+00
45      2.000000E+00  7.500000E-01
46      2.000000E+00  5.000000E-01
47      2.000000E+00  2.500000E-01
48      2.500000E-01  2.000000E+00
49      5.000000E-01  2.000000E+00
50      7.500000E-01  2.000000E+00
51      1.000000E+00  2.000000E+00
52      1.250000E+00  2.000000E+00
53      1.500000E+00  2.000000E+00
54      1.750000E+00  2.000000E+00
55      0.000000E+00  2.500000E-01
56      0.000000E+00  5.000000E-01
57      0.000000E+00  7.500000E-01
58      0.000000E+00  1.000000E+00
59      0.000000E+00  1.250000E+00
60      0.000000E+00  1.500000E+00
61      0.000000E+00   1.750000E+00
62      0.000000E+00   2.000000E+00
63      2.000000E+00   2.000000E+00
64      2.000000E+00   0.000000E+00
65      0.000000E+00   0.000000E+00
```

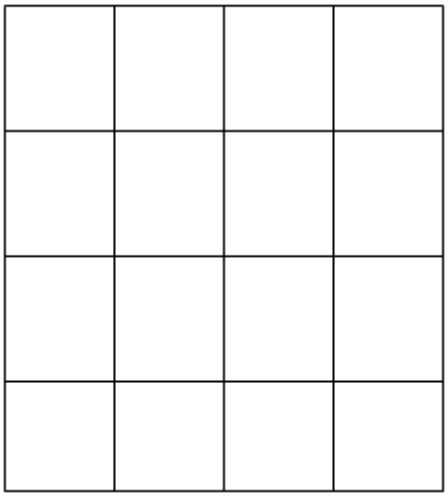

Figure A.4: 16-element block.

The first line includes the number of nodes, number of elements, number of material definitions, and the problem type.

This is followed by the material definitions. Materials are numbered according to the order they are listed. Therefore material numbers are not explicitly listed in the .inp file. For each material definition the first number is the material model. The following numbers are the parameters for the given model .

Next the element conductivities are listed. On these lines, the element number is followed by the material definition number assigned to that element and the node numbers listed in **counterclockwise** order.

Next the node data are listed. Each line contains the node number followed by the X and Y coordinates.

This would be the end of a typical FRANC2D/L input file. However, for these polycrystal models, information concerning the von Mises materials and the cohesive zone models are appended to the end of the file

The implemented von Mises plasticity model allows hardening to occur. Normally the hardening curve is defined after opening FRANC2D/L . However, with many materials defined this becomes inefficient. Therefore, the definitions of these curves were appended to the .inp file following the Matlab text string 'hardcurve.txt'. For each von Mises material defined several lines are appended. The first line indicates the number of points used to define the curve. Each subsequent line lists the X and Y coordinates of a point on the curve. Below is an example of the hardening curve information appended to the end of the file:

```
HARDCURVE
5
7
0.000000 0.000000
0.007029 501.289246
```

```
0.015000 520.443115
0.040000 533.212402
0.100000 552.366272
0.160000 565.135498
0.200000 565.135498
7
0.000000 0.000000
0.007031 503.627289
0.015000 524.024231
0.040000 537.622131
0.100000 558.019043
0.160000 571.617004
0.200000 571.617004
7
0.000000 0.000000
0.006899 499.957123
0.015000 521.006836
0.040000 535.039978
0.100000 556.089722
0.160000 570.122864
0.200000 570.122864
7
0.000000 0.000000
0.006997 502.910095
0.015000 524.325928
0.040000 538.603149
0.100000 560.019043
0.160000 574.296265
0.200000 574.296265
7
0.000000 0.000000
0.006805 495.463257
0.015000 518.383179
0.040000 533.663147
0.100000 556.583069
0.160000 571.862976
0.200000 571.862976
```

Below 'Hardcurve' is the number of grains in the file. Then an individual hardening curve for each grain is written out. Listed first is the number of load-steps in each curve, and then the corresponding strain vs. stress values of the

hardening curve.

Next, the coupled cohesive zone models for the grain boundaries are listed following the text string 'multiCZM'. Each coupled cohesive zone model is valid for a range of misorientations measured across the grain boundary. Listed first is the number of interface models listed. Below the number of models, the angle range is listed first followed by the model parameters as shown below:

```
multiCZM
1
0 360 5.500000e-001 1.000000e-006 1.000000e-006 4000000 4000000
```

Finally, the CCZM used to define the particle-grain interface is listed following the text string 'ParticleCZM'. The format is the same as listed above. However, the angle range is given as 0 360. Currently, all particle-grain interfaces must follow the same response so just one model is defined. However, the angle range is still listed for consistency and the ability to easily expand the modeling capabilities in the future. Below is example of the appended particle CCZM information:

```
ParticleCZM
1
1000 1001 5.00E-002 1.00E-005 1.00E-005 5.00E+003 5.00E+003
```

Franc2D/L Examples

Four example problems will be presented one for each of the four material models. The units of force and distance used in these examples are newtons (N) and millimeters (mm), respectively. Therefore, the derived units for stress/modulus are MegaPascals (MPa).

Example 1

The first example will examine isotropic, linear elastic grains without particles, and with grain boundaries modeled through CCZMs.

Building an Initial Geometry and Mesh

For this example, the following input was used to create a 1 mm square with 50 randomly generated grains. Start by creating the tessellation in MATLAB with the following command:

```
DM_tess('tutorial1',1,50,312)
```

Figure A.5 shows the results from this input.

This is a simple example therefore particles will not be placed in the polycrystal. Therefore, the next step is assign grain properties, mesh the tessellation, material properties, and define cohesive zone models.

The four files used to define the material properties, in general, are *properties.txt, hardcurve.txt, betalist.txt,* and *partprop.txt.* In this example only *properties.txt* is needed. The following is the input file *properties.txt* used in this example:

`Properties.txt:`

```
72000 2000 1000
0 0
0 0
0.33 0 0
1
1.0
0.00632 0.0 25
10000000
0 0
0 0
0 0
```

The first row of the input file sets the mean elastic modulus of the grains at 72000 MPa, with a range of ± 2000 MPa and a standard deviation of 1000 MPa. The next two rows are arbitrarily set to 0 because these rows are only used in orthotropic problems, whereas the grains in this example are isotropic. The next row assigns poison's ratio to 0.33, again the last two values are arbitrarily set to 0 because this is an isotropic problem. The next four rows assign the values of thickness, density, K_{IC}, and K_{IC_Inf}. The final three rows are used to define yielding points of the grains. The values are arbitrarily set to 0 in this case since the grains are considered linear elastic.

The next step is to mesh the polycrystal sample, accomplished with the following command:

```
DM_mshtess('tutorial1',1,1,284,549,.15)
```

Finally, the interface properties are assigned by the following statements. To simplify this example one CZM will be used for all of the grain boundaries. Therefore the angle inputted to **DM_multiCZM1** will be 360.

```
DM_multiczm1('tutorial',360)
```

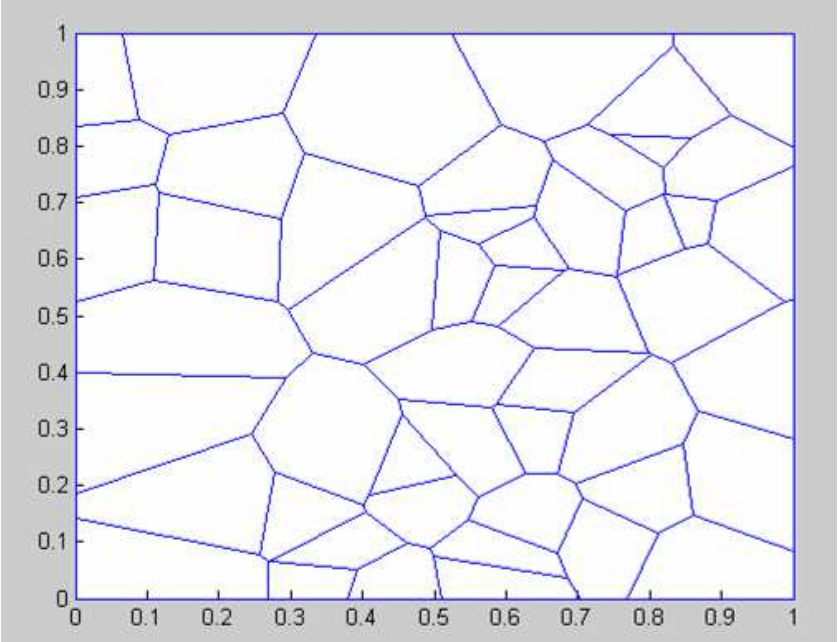

Figure A.5: Matlab figure output from DM_tess

Performing a Franc2D/L Simulation

Start FRANC2D/L with the *.inp file created above. Due to the size of the model it may be necessary to start the program with extra memory allocated. That is done by calling the program as shown below. This example is small enough that this command is not needed. However, for slightly larger models it will be needed.

```
Franc2dl.exe -mem 25000000
```

Due to the size of the models it may take a moment for the file to be read. Once the model is read in there are still several pre-processing steps before the model is ready for analysis. It is important to follow the procedure in the order listed. Of most importance is that the interface elements must be placed before applying displacements to the model.

Defining the Problem Type

The problem type is specified under **PRE-PROCESS → PROBLEM TYPE** menu. Plain strain is preferred for these models. However, if the grains are defined as Hill materials then plane stress must be used.

Boundary Conditions: Fixities

Fixities are applied from the **PRE-PROCESS → FIXITY** menu. For this example the bottom edge is fixed in the Y-direction and the left and right edges are in the X-direction.

Inserting Interface Elements

As described in the FRANC2D/L version 1.5 user's guide a feature has been added to automatically place interface elements along all interfaces. The feature can be assessed through the **PRE-PROCESS → MATERIAL** menu. Use the **-MAT+** button to move to the interface model. In the bottom menu will be the button **PLACE ALL INTS**. Click on this button. To determine that the interface elements have been placed turn on the interfaces using the **INTRFC: ON/OFF** button. The interfaces will appear white while the other element edges will be orange. If an interface element is present the corresponding material number will be next to the element. Now click on **COUPLED** and insert the proper material properties for the CCZM by clicking on each property in turn and entering the values below.

```
PEAK STRESS:   500
CRIT DISP N:   0.001
CRIT DISP S:   0.001
INIT K NORM:   5x106
INIT K SHEAR:  5x106
```

Setting the Material Properties

The grains were assigned material numbers during the meshing process. Therefore no other action is required here.

Applied Displacements

Finally the displacements are applied. Using loads is discouraged with polycrystal models since the analysis will likely become unstable.

Apply a unit displacement to the top edge of the model from the **PRE-PROCESS** → **APPLD DISP** menu. Select **EDGE DISP** → **Y DISP** and apply a displacement of 0.00583 mm along the top edge of the model. This displacement corresponds to a

Perform Analysis

Before performing the analysis be sure to save a restart file. This can be done before or after setting the control parameters. If there is not enough memory the solver will stop and the program will need to be restarted with more memory. Starting from a restart file will make this go quicker.

Even if the grains are defined to be elastic, the presence of the interface elements makes the analysis material non-linear. Therefore select the **ANALYSIS** → **MAT-NONLIN** option.

Select **CONTROL PARAM** to set up the analysis. The parameters will appear in the auxiliary window. Using the menu buttons set the option as follows.

```
Load Sub-Steps : 10
Global Tolerance: 0.001
Max Iterations : 200
Load Factor 1 : 0
Load Factor 2 : 0
```

```
Load Factor 3 : 0
Load Factor 4 : 0
Load Factor 5 : 0
Load Factor 6 : 0
Appld Dist Factor: 1
Accelerate Iter : NONE
New Analysis : YES
Current Step : 0
Final Step     : 10
Save Frequency : 0
Print Frequency : 50
Increment Method: FIXED
Anaylsis Mode : INCREMENTAL
Autosave File : jobname
```

Return from this menu. Select **ANALYZE ONE** to conduct the analysis. Do to the large number of degrees of freedom the initial set up before the solve actually begins can take a several minutes. The total solve time for example is about ? minutes.

Post-Processing

Post-processing options are discussed in the FRANC2D/L User's Guide. The feature of note for this simulation is **POST-PROCESS** → **CONTOURS** → **STRAIN** → **INT SEPAR**. This shows the separation experienced by the interface elements. This can be useful for identifying elements that have started to decohere or that have fully decohered. In this example you will notice a grain boundary beginning to decohore in the lower left corner of the polycrystal model.

Example 2

This example problem introduces linear elastic orthotropic grains.

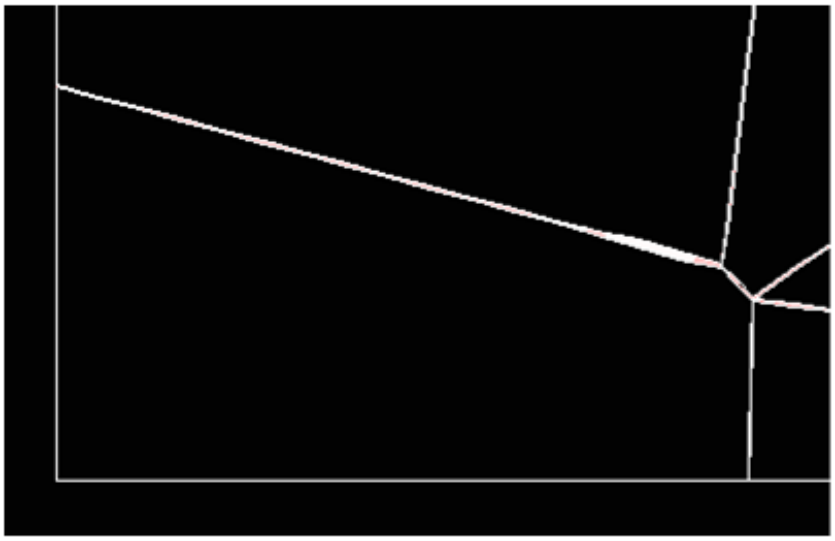

Figure A.6: FRANC2D/L showing the beginning of Grain Boundary Decohesion

Building an Initial Geometry and Mesh

We will use the same tessellation as in the first example problem, so in MATLAB, type the following command:

```
DM_tess('tutorial2',1,50,312)
```

The material properties will be assigned next. In this example two files, *properties.txt* and *betalist.txt*, are needed to assign all the pertinent material properties. The following is the input file *properties.txt* used in this example:

```
Properties.txt:
72000 2000 1000
42000 2000
42000 2000
0.33 0.33 0.33
1
1.0
0.00632 0.0 25
10000000
0 0
0 0
0 0
```

The inputs in this example are the same as the first example, except for second, third, and fourth rows. Since this is an orthotropic problem three values of elastic modulus (E_1,E_2,E_2) and three values of poison's ratio (ν_{12},ν_{23},ν_{31}) must be assign. The first row assigns the values for E_1, while the second and third rows assign the values of E_2 and E_3, respectively. The value of E_2 and E_3 are set at 42000 $\pm$ 2000 MPa, which is significantly less then the value of 72000 $\pm$ 2000 MPa for E_1. The fourth row sets all three values of Possion's ratio at 0.33. In addition to assigning three values for elastic modulus and three values for poison's ratio, the orientation of each grain must assigned. These values are assigned in the file *betalist.txt*. This file requires an orientation angle, beta (which is the angle from the global X-axis to the E_1 axis), for every grain in the example. So in this example 50 values of beta must be assigned for each of the 50 grains. Below are the first fifteen entries of the *betalist.txt* file used in this example:

```
Betalist.txt
-6.424200e+001
1.442100e+002
1.298340e+002
2.664060e+002
1.082700e+002
5.076600e+001
-2.830200e+001
1.298340e+002
1.585860e+002
4.357800e+001
-8.580600e+001
5.076600e+001
1.945260e+002
2.160900e+002
2.376540e+002
```

The rest of the betalist.txt file is just a repeated pattern of these fifteen entries. Once the material properties are set the next step is to mesh the tessellation. The same mesh from example 1 will be used:

```
DM_mshtess('tutorial2',2,1,284,549,.15)
```

Again a single CCZM will be used for grain boundary representation:

```
DM_multiczm1('tutorial2',360)
```

Performing a Franc2D/L Simulation

The *tutorial2.inp* file should be opened in FRANC2D/L.

Defining the Problem Type

The problem type is specified under **PRE-PROCESS → PROBLEM TYPE** menu.

Boundary Conditions: Fixities

Fixities are applied from the **PRE-PROCESS → FIXITY** menu. For this example the bottom edge is fixed in the Y-direction and the left and right edges are in the X-direction.

Inserting Interface Elements

Interface elements can be inserted through the **PRE-PROCESS → MATERIAL** menu. Use the **-MAT+** button to move to the interface model. In the bottom menu will be the button **PLACE ALL INTS**. Click on this button. To determine that the interface elements have been placed turn on the interfaces using the **INTRFC: ON/OFF** button. The interfaces will appear white while the other element edges will be orange. If an interface element is present the corresponding material number will be next to the element. Now click on COUPLED and insert

the proper material properties for the CCZM by clicking on each property in turn and entering the values below.

```
PEAK STRESS:   500
CRIT DISP N:   0.001
CRIT DISP S:   0.001
INIT K NORM:   5x106
INIT K SHEAR:  5x106
```

Applied Displacements

A displacement will be assigned to the top edge of the model through the **PRE-PROCESS** → **APPLD DISP** menu. Select **EDGE DISP** → **Y DISP** and apply a displacement of 0.00583 mm along the top edge of the model

Perform Analysis

Before performing the analysis be sure to save a restart file. Select the **ANALYSIS** → **MAT-NONLIN** option.

Select **CONTROL PARAM** to set up the analysis. The parameters will appear in the auxiliary window. Using the menu buttons set the option as follows.

```
Load Sub-Steps : 10
Global Tolerance: 0.001
Max Iterations : 200
Load Factor 1 : 0
Load Factor 2 : 0
Load Factor 3 : 0
Load Factor 4 : 0
Load Factor 5 : 0
Load Factor 6 : 0
Appld Dist Factor: 1
Accelerate Iter : NONE
New Analysis : YES
Current Step : 0
Final Step     : 10
Save Frequency : 0
```

```
Print Frequency : 50
Increment Method: FIXED
Anaylsis Mode : INCREMENTAL
Autosave File : jobname
```

Return from this menu. Select **ANALYZE ONE** to conduct the analysis. Do to the large number of degrees of freedom the initial set up before the solve actually begins can take a several minutes. The total solve time for example is about ? minutes.

Post-Processing

Select **POST-PROCESS** → **CONTOURS** → **STRAIN** → **INT SEPAR**. This shows the separation experienced by the interface elements. This can be useful for identifying elements that have started to decohere or that have fully decohered. In this example you will notice more grain boundaries undergoing decohesion than in the previous example.

Example 3

We will now introduce particles and plasticity into the simulation. The von Mises plasticity model will be used for this example problem, while the Hill plasticity model will be used in example 4.

Building an Initial Geometry and Mesh

Since this example is more computationally intensive, we will work with a smaller polycrystal. A polycrystalline square with sides of 0.5 mm, consisting of 25 grains, is tesselated with the following command:

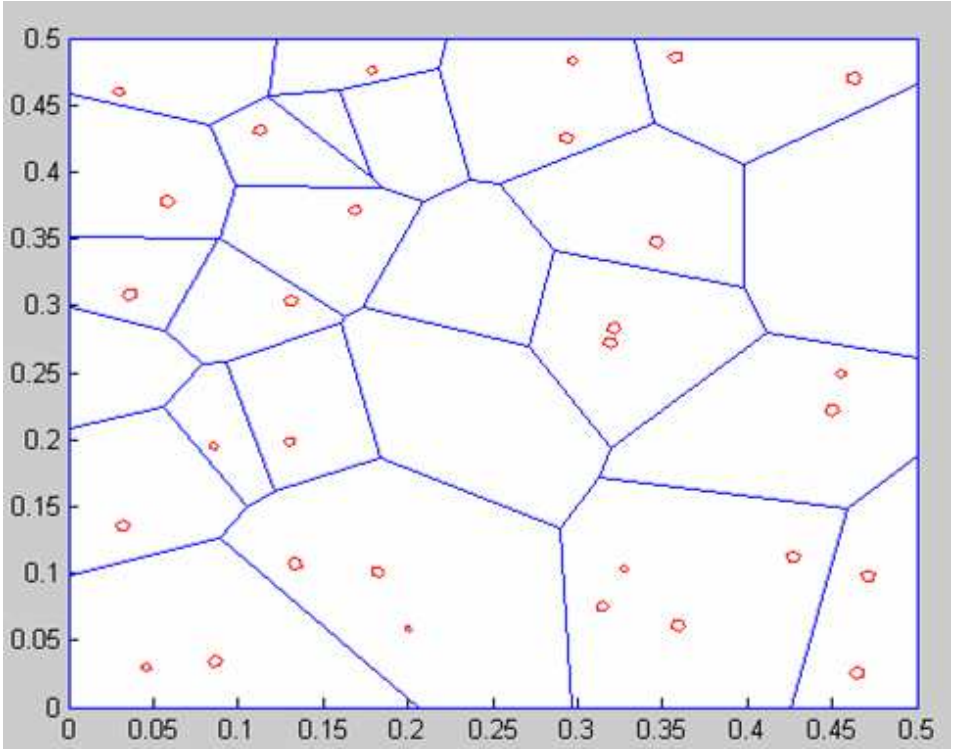

Figure A.7: Matlab figure output from DM_Particlelist

```
DM_tess('tutorial3',0.5,25,541)
```

Thirty particles will be inserted into the polycrystal. The particles are modeled as polygons. In this case pentagons will be used to represent the particles. The particles can be inserted with the following command:

```
DM_ParticleList('tutorial3',30,5,.05,.005,.5,.25,471)
```

The polycrystal with the inserted particles can be seen below in Figure A.7.

Three files are needed to assign the material properties in this example: *properties.txt, hardcurve.txt*, and *partprop.txt*. The *properties.txt* file controls the elastic properties of grains, while the *hardcurve.txt* file controls the hardening properties of the grains. The —it partprop.txt controls the elastic properties of the particles. The following is the input file *properties.txt* used in this example:

```
Properties.txt:
72000 2000 1000
0 0
0 0
0.33 0 0
1.0
1.0
0.00632 0.0 25
10000000
500 10
0 0
0 0
```

The properties in this file are the same as in the first example except for the ninth row. Instead of being arbitrarily set to 0, as in the first example, the yield strength of the grains is set at 500 MPa, with a range of ± 10 MPa. The last two rows are still arbitrarily set to 0 because the grains are modeled as isotropic. The following is the input file *hardcurve.txt* used in this example:

```
Hardcurve.txt
500 570 10
```

This file defines a hardening curve for the grains. The first entry corresponds to a yield strength of 500 MPa, which is the same yield strength entered in the *properties.txt* file. The second entry sets the ultimate strength of the grains at 570 MPa, while the third entry sets the step-size used in defining the hardening curve. Since the step-size is set at 10 MPa in this example, the hardening curve is defined in seven evenly spaced increments from 500 MPa to 570 MPa. The following is the input file *partprop.txt* used to define the particle properties in this example:

```
Partprop.txt
166400 10000
0.33
1
1.0
0.00632 0.0
```

The first row of this file set the elastic modulus of particles at 166.4 GPa with a range of ± 10 GPa. While the second row sets poison's ratio at 0.33. The last three rows assign the values for thickness, density, and K_{IC}.

The next step is to mesh the model. This is accomplished with the following command:

```
DM_mshtess('tutorial3',3,.5,372,406,.1)
```

Two CCZMs have to be defined in this example problem: one between the grains and one surrounding the particles. The CCZM between the grains is established with the following command:

```
DM_multiczm1('tutorial3',360)
```

The properties of the CCZM are assigned in *part_czm.txt*. The *part_czm.txt* file for this example is as follows:

```
Part_czm.txt
ParticleCZM
1
1000 1001 5.00E+002 1.00E-005 1.00E-005 5.00E+006 5.00E+006
```

The third through seventh entries in the last rows set the CCZM model parameters. The peak traction is set at 50 MPa, both critical opening displacements at 10 nm, and both initial stiffnesses set at 5,000 GPa. Once the properties are assign the the CCZM is placed in the *tutorial3.inp* file with the following command:

```
DM_ParticleCZM('tutorial3')
```

Performing a **Franc2D/L** Simulation

The *tutorial3.inp* file can be opened in FRANC2D/L.

Defining the Problem Type

The problem type is specified under **PRE-PROCESS → PROBLEM TYPE** menu. Plain strain is preferred for these models.

Boundary Conditions: Fixities

Fixities are applied from the **PRE-PROCESS → FIXITY** menu. For this example the bottom edge is fixed in the Y-direction and the left and right edges are in the X-direction.

Inserting Interface Elements

The feature can be assessed through the **PRE-PROCESS → MATERIAL** menu. Use the **-MAT+** button to move to either of the interface model. In the bottom menu will be the button **PLACE ALL INTS**. Click on this button. To determine that the interface elements have been placed turn on the interfaces using the **INTRFC: ON/OFF** button. The interfaces will appear white while the other element edges will be orange. There should be two different material numbers shown along the interfaces. Between the grains material number 26 should displayed, while around the particles material number 27 should be displayed. The parameters for the interface model surrounding the particles have already been assigned. The parameters for interface model between the grains must now be assigned. Use the **-MAT+** button to select material number 26. Click on **COUPLED** and insert the proper material properties for the CCZM by clicking on each property in turn and entering the values below:

```
PEAK STRESS:   500
CRIT DISP N:   0.001
CRIT DISP S:   0.001
```

```
INIT K NORM:    5x106
INIT K SHEAR:   5x106
```

Applied Displacements

Apply a unit displacement to the top edge of the model from the **PRE-PROCESS** → **APPLD DISP** menu. Select **EDGE DISP** → **Y DISP** and apply a displacement of 0.005 mm along the top edge of the model. This displacement corresponds to a 1% strain on the polycrystal model.

Perform Analysis

Before performing the analysis be sure to save a restart file. Select the **ANALYSIS** → **MAT-NONLIN**.

Select **CONTROL PARAM** to set up the analysis. The parameters will appear in the auxiliary window. Using the menu buttons set the option as follows.

```
Load Sub-Steps : 10
Global Tolerance: 0.001
Max Iterations : 200
Load Factor 1 : 0
Load Factor 2 : 0
Load Factor 3 : 0
Load Factor 4 : 0
Load Factor 5 : 0
Load Factor 6 : 0
Appld Dist Factor: 1
Accelerate Iter : NONE
New Analysis : YES
Current Step : 0
Final Step     : 10
Save Frequency : 0
Print Frequency : 50
Increment Method: FIXED
Anaylsis Mode : INCREMENTAL
Autosave File : jobname
```

Return from this menu. Select **ANALYZE ONE** to conduct the analysis. Do to the large number of degrees of freedom the initial set up before the solve actually begins can take a several minutes. The total solve time for example is about ? minutes.

Post-Processing

Post-processing options are discussed in the FRANC2D/L User's Guide. The feature of note for this simulation is **POST-PROCESS** → **CONTOURS** → **STRAIN** → **INT SEPAR**. This shows the separation experienced by the interface elements. This can be useful for identifying elements that have started to decohere or that have fully decohered. In this example you will notice most of the particles have completely decohered.

Example 4

This example will use the orthotropic Hill plasticity model in conjunction with grains and particle inclusions.

Building an Initial Geometry and Mesh

The polycrystal and included particles in this example will be the same as was used in example 3. The tessellation and particle inclusions can be created with following two commands:

```
DM_tess('tutorial3',0.5,25,541)
```

```
DM_ParticleList('tutorial3',30,5,.05,.005,.5,.25,471)
```

Two files, *properties.txt* and *betalist.txt*, are needed to assign the grain properties with the Hill plasticity model. The particle properties are assigned in the *partprop.txt* file.

```
Properties.txt:
72000 2000 1000
0 0
0 0
0.33 0 0
1.0
1.0
0.00632 0.0 25
10000000
500 10
0 0
0 0


Betalist.txt
500 570 10


Partprop.txt
166400 10000
0.33
1
1.0
0.00632 0.0


DM_mshtess('tutorial3',3,.5,372,406,.1)


DM_multiCZM1('tutorial3',360)

Part_czm.txt
ParticleCZM
1
1000 1001 5.00E+002 1.00E-005 1.00E-005 5.00E+006 5.00E+006


DM_partCZM('tutorial3')
```

Performing a Franc2D/L Simulation

The *tutorial3.inp* file can be opened in FRANC2D/L.

Defining the Problem Type

The problem type is specified under **PRE-PROCESS → PROBLEM TYPE** menu. Plain stress must be used for Hill materials.

Boundary Conditions: Fixities

Fixities are applied from the **PRE-PROCESS → FIXITY** menu. For this example the bottom edge is fixed in the Y-direction and the left and right edges are in the X-direction.

Inserting Interface Elements

The feature can be assessed through the **PRE-PROCESS → MATERIAL** menu. Use the **-MAT+** button to move to either of the interface model. In the bottom menu will be the button **PLACE ALL INTS**. Click on this button. To determine that the interface elements have been placed turn on the interfaces using the **INTRFC: ON/OFF** button. The interfaces will appear white while the other element edges will be orange. There should be two different material numbers shown along the interfaces. Between the grains material number 26 should displayed, while around the particles material number 27 should be displayed. The parameters for the interface model surrounding the particles have already been assigned. The parameters for interface model between the grains must now be assigned. Use the **-MAT+** button to select material number 26. Click on **COUPLED** and insert the proper material properties for the CCZM by clicking

on each property in turn and entering the values below:

```
PEAK STRESS:   500
CRIT DISP N:   0.001
CRIT DISP S:   0.001
INIT K NORM:    5x106
INIT K SHEAR:   5x106
```

Applied Displacements

Apply a unit displacement to the top edge of the model from the **PRE-PROCESS** → **APPLD DISP** menu. Select **EDGE DISP** → **Y DISP** and apply a displacement of 0.005 mm along the top edge of the model. This displacement corresponds to a 1% strain on the polycrystal model.

Perform Analysis

Before performing the analysis be sure to save a restart file. Select the **ANALYSIS** → **MAT-NONLIN**.

Select **CONTROL PARAM** to set up the analysis. The parameters will appear in the auxiliary window. Using the menu buttons set the option as follows.

```
Load Sub-Steps : 10
Global Tolerance: 0.1
Max Iterations : 200
Load Factor 1 : 0
Load Factor 2 : 0
Load Factor 3 : 0
Load Factor 4 : 0
Load Factor 5 : 0
Load Factor 6 : 0
Appld Dist Factor: 1
Accelerate Iter : NONE
New Analysis : YES
Current Step : 0
Final Step   : 10
Save Frequency : 0
```

```
Print Frequency : 50
Increment Method: FIXED
Anaylsis Mode : INCREMENTAL
Autosave File : jobname
```

Return from this menu. Select **ANALYZE ONE** to conduct the analysis. Do to the large number of degrees of freedom the initial set up before the solve actually begins can take a several minutes. The total solve time for example is about ? minutes.

Post-Processing

Post-processing options are discussed in the FRANC2D/L User's Guide. The feature of note for this simulation is **POST-PROCESS** → **CONTOURS** → **STRAIN** → **INT SEPAR**. This shows the separation experienced by the interface elements. This can be useful for identifying elements that have started to decohere or that have fully decohered. In this example you will notice most of the particles have completely decohered.

Acknowledgments

Prof. Anthony Ingraffea (Cornell University) has focused on the goal of developing the ability to rapidly model discrete crack growth for about fifteen years. FRANC2D/L represents the work of several generations of students: Prof. Ingraffea modeled discrete crack growth by changing a mesh described by a deck of computer cards, Victor Sauoma modeled discrete crack growth on a Tektronix terminal, Walter Gerstle modeled crack growth on an Evans and Sutherland display, and finally, Paul Wawrzynek (Wash) used a workstation, started from scratch, and introduced robust data schemes to the engineers who had come before. Layering

has been added by Sudhir Gondhalekar and Srinivas Krishnan at Kansas State University. Mark James is the most significant developer of the code at Kansas State. He has stabilized the code, added new features, maintained the multiple platform versions, and done all the work necessary to make the code a genuinely useable tool. In addition, he is extending FRANC2D/L to include elastic/plastic fracture. The approach is the crack tip opening angle method of Dr. Jim Newman, NASA. The port of GRA to Windows 95/NT was done by Brian Hardeman.

The addition of layers has been supported by the Mechanics of Materials Branch at NASA Langley Research Center under the direction of Dr. Jim Newman and Dr. Charlie Harris. We appreciate comments received from Dave Dawicke, an early user of the program.

APPENDIX A.1

Although coupled cohesive zone properties of the interfaces can be defined within the .inp file prior to running FRANC2D/L there are some instances where the user may prefer to create the cohesive zone models while pre-processing in FRANC2D/L . The following is a brief overview of how to do so for the coupled cohesive zone model described in this tutorial.

As shown in Figure A.8, the user must select "Pre-Process", then "Material" to access the material menu. Since the DM_MultiCZM and DM_ParticleCZM functions were not run while creating the .inp file, the interface materials are yet to be defined. Therefore, the user must click on "New Mat" to define the interface properties. Since the coupled cohesive zone models used in this tutorial are bilinear, the user should select "NL Interface" for the non-linear menu, then "Coupled" for the CCZM menu. The "symmetry" flag has a default setting of "0", meaning that the interface is not on a symmetry plane, but if there is a symmetry interface, the flag should be changed to "1". The "Peak Stress" should be entered as the tp value from the CCZM bilinear curve. The "Crit Disp N" and "Crit Disp S" should be entered for the respective cn and ct values. Lastly, for the CCZM's discussed in this tutorial, "Init K Norm" and "Init K Shear" are both entered as the same value, kn from the linear softening curve.

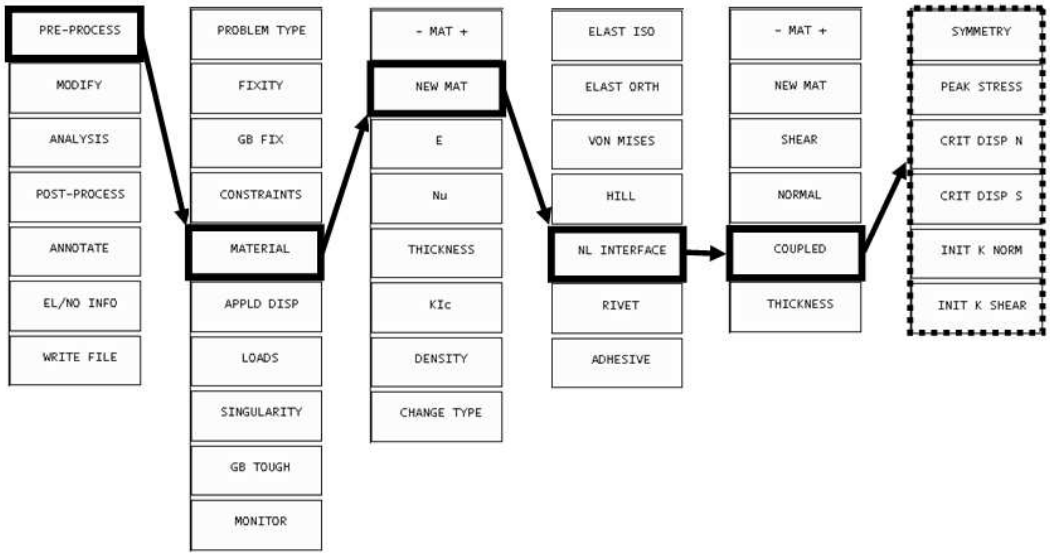

Figure A.8: CCZM Pre-Processing Menus

BIBLIOGRAPHY

[1] P.M. Anderson and J.R. Rice. Constrained creep cavitation of grain boundary facets. *Acta Metallurgica*, 33(3):409–422, 1985.

[2] N. Kanetake, M. Nomura, and T. Choh. Continuous observation of microstructural degradation during tensile loading of particle reinforced aluminum composites. *Materials Science and Technology*, 11:1246–1252, 1995.

[3] E. Iesulauro. Decohesion of grain boundaries in statistical representations of aluminum polycrystal. Master's thesis, Cornell University, Ithaca, NY, January 2001.

[4] K. Dodhia. Simulations of crack initiation in aluminum alloys with inclusions. Master's thesis, Cornell University, Ithaca, NY, January 2001.

[5] J.E. Hatch. *Aluminum: properties and physical metallurgy*. American Society for Metals, 1984.

[6] A.D. Rollett, D. Saylor, J. Fridy, B. El-Dasher, A. Brahme, S-B Lee, C. Cornwell, and R. Noack. Modeling polycrystalline microstructures in 3d. In S. Ghosh, J.C. Castro, and J.K Lee, editors, *CP712, Materials Processing and Design: Modeling, Simulation, and Applications*, pages 71–77, Cardiff, Wales, 2004. NUMIFORM 2004, American Institute of Physics.

[7] V. Tvergaard and J.W. Hutchinson. The relation between crack growth resistance and fracture process parameters in elastic-plastic solids. *Journal of the Mechanics and Physics of Solids*, 40(100):1377, July 1992.

[8] W. Elber. *ASTM STP 486*, pages 230–242, 1971.

[9] D.S. Dugdale. Yielding of steel sheets containing slits. *Journal of the Mechanics and Physics of Solids*, 8(100):100–108, July 1960.

[10] G.I. Barenblatt. Mathematical theory of equilibrium of cracks in brittle fracture. *Advanced Applications in Mechanics*, 7:55–129, July 1962.

[11] P.C. Paris, R.E. Gomez, and W.E. Anderson. A rational analytic theory of fatigue. *The Trend in Engineering*, 13(1), 1961.

[12] S. Pearson. Initiation of fatigue cracks in commercial aluminum alloys and the subsequent propagation of very short cracks. *Engineering Fracture Mechanics*, 7(2):235–247, 1975.

[13] J. Lankford. Growth of small fatigue cracks in 7075-T6 aluminum. *Fatigue of Engineering Materials and Structures*, 5(3):233–248, 1985.

[14] S. Suresh. *Fatigue of materials*. Cambridge University Press, 1991.

[15] J. Schijve. Fatigue crack growth and fracture mechanics. *Engineering Fracture Mechanics*, 11(1):167–181, 1979.

[16] Cornell Fracture Group. *Users Guide to* FRANC2D. Cornell Fracture Group. www.cfg.cornell.edu.

[17] M. Gao, C.R. Feng, and R.P. Wei. An analytical electron microscopy study of constituent particles in commercial 7075-T6 and 2024-T3 alloys. *Metallurgical and Materials Transactions A*, 29A:1145–1151, 1998.

[18] P. Campestrini, E.P.M. van Westing, H.W. van Rooijen, and J.H.W. de Wit. Relation between microstructural aspects of AA2024 and its corrosion behavior investigated using afm scanning potential technique. *Corrosion Science*, 42:1853–1861, 2000.

[19] S.E. Stanzl-Tschegg, O. Plasser, E.K. Tschegg, and A.K. Vasudevan. Influence of microstructure and load ratio on fatigue threshold behaviour in 7075 aluminum alloy. *International Journal of Fatigue*, 21:225–262, 1999.

[20] D.G. Harlow and R.P. Wei. Probability modelling for the growth of corrosion pits. *Structural Integrity in Aging Aircraft ASME*, 47:185–194, 1995.

[21] J.R. Rice. Constraints on the diffusive cavitation of isolated grain boundary facets in creeping polycrystals. *Acta Metallurgica*, 29:675–681, 1981.

[22] R. Raj and M.F. Ashby. Intergranular fracture at elevated temperature. *Acta Metallurgica*, 23(3):653–666, 1975.

[23] D.G. Harlow, H-M. Lu, J.A. Hittinger, T.J. Delph, and R.P. Wei. A three-dimensional model for the probabilistic intergranular failure of polycrystalline arrays. *Modelling and Simulation in Material Science and Engineering*, 4(3):261–279, 1996.

[24] F.L. Carranza and R.B. Haber. A numerical study of intergranular fracture and oxygen embrittlement in an elastic-viscoplastic solid. *Journal of the Mechanics and Physics of Solids*, 47:27–58, 1999.

[25] M. James. *Users Guide to* FRANC2D/L. Kansas State University. www.mne.ksu.edu/franc2d/.

[26] R.P. Wei, D. Masser, H. Liu, and D.G. Harlow. Probabilistic considerations of creep crack growth. *Material Science and Engineering*, A189:69–76, 1994.

[27] M.M. Rashid. Texture evolution and plastic response of two-dimensional polycrystals. *Journal of the Mechanics and Physics of Solids*, 40(5):1009–1029, 1992.

[28] H.S. Turkmen, R.E. Loge, P.R. Dawson, and M.P. Miller. On the mechanical behaviour of aa 7075-t6 during cyclic loading. *International Journal of Fatigue*, 25:267–281, 2003.

[29] Y. Zhao and R. Tryon. Automatic 3d simulation and mises-stress distribution of polycrystalline metallic materials. *Computer Methods in Applied Mechanics and Engineering*, 193:3919–3934, 2004.

[30] E. Iesulauro and K. Dodhia. *Simulations of Statistical Representations of POlycrystal using* FRANC2D/L. Cornell Fracture Group. www.cfg.cornell.edu.

[31] The MathWorks, Inc. *Matlab*.

[32] M.A. James. *A plane stress finite element model for elastic-plastic mode I/II crack growth*. PhD dissertation, Kansas State University, Department of Mechanical and Nuclear Engineering, May 1998.

[33] F. Aurenhammer. Voronoi diagrams - a survey of a fundamental geometric data structure. *ACM Computing Surveys*, 23:345–405, 1991.

[34] J. OŔourke. *Computational Geometry in C*. Cambridge University Press, 1994.

[35] C.B. Barber, D.P. Dobkin, and H.T. Huhdanpaa. The quickhull algorithm for convex hulls. *ACM Trans. on Mathematical Software*, 22(4):469–483, 1996.

[36] S.R. Arwade. Probabilistic models for aluminum microstructure and intergranular fracture analysis. Master's thesis, Cornell University, Ithaca, NY, May 2000.

[37] J.B. Cavalcante Neto, P.A. Wawrzynek, M.T.M Carvalho, L.F. Martha, and A.R. Ingraffea. An algorithm for three-dimensional mesh generation for arbitrary regions with cracks. *Engineering with Computers*, 17:75–91, 2001.

[38] G.R. Irwin. Plastic zone near a crack and fracture toughness. *Proceedings of the 7th Sagamore Conference*, 7:4–63, July 1960.

[39] A. Hillerborg, M. Modeer, and P.E. Petersson. Analysis of crack formation and crack growth in concrete by means of fracture mechanics and finite elements. *Cement and Concrete Research*, 6:773–782, July 1976.

[40] A. Hillerborg. Application of the fictitious crack model to different materials. *International Journal of Fracture*, 51:95–102, July 1991.

[41] D. Broek. *Elementary engineering fracture mechanics*. Kluwer Academic Publishers, 1986.

[42] T.L. Anderson. *Fracture mechanics: Fundamentals and applications.* CRC Press, 1995.

[43] P.A. Wawrzynek. Interactive finite element analysis of fracture processes : an integrated approach. Master's thesis, Cornell University, Department of Civil and Environmental Engineering, May 1987.

[44] T. Bittencourt. *Computer simulation of linear and nonlinear crack propagation in cementitous materials.* PhD dissertation, Cornell University, Department of Civil and Environmental Engineering, May 1993.

[45] C.Q. Bowles and K. Schive. The role of inclusions in fatigue crack initiation in an aluminum alloy. *International Journal of Fatigue*, 9(2):171–179, 1973.

[46] D.S. Thompson. Metallurgical factors affecting high strength aluminum alloy production. *Metallurgical Trans-actions A*, 6A:671–682, 1975.

[47] D. Saylor, J. Fridy, B. El-Dasher, K-Y Jung, and A. Rollet. Statistically representative three-dimensional microstructures based on orthogonal observation sections. *Metallurgical and Materials Transactions A*, 35:1969–1979.

[48] D. Basanta, P. Bentley, M. Miodownik, and E. Holm. Evolving and growing microstructures of materials using biologically inspired ca. In *In proceedings of the 2004 NASA/DoD Conference on Evolvable Hardware, Seattle, WA.*, 2004.

[49] Chris Myers. *PyXL.* http://www.tc.cornell.edu/

[50] S. Balay, W.D. Gropp, L.C. McInnes, and B.F. Smith. *PETSc Users Manual.* Argonne National Laboratory, ANL-95/11-Revision 2.1.1 (2001).

[51] C. Miehe and J. Schroder. A comparative study of stress update algorithms for rate-independent and rate-dependent crystal plasticity. *International Journal for Numerical Methods in Engineering*, 50(2):273–798, January 2001.

[52] K Matous and A.M. Maniatty. Finite element formulation for modelling large deformations in elasto-viscoplastic polycrystals. *International Journal for Numerical Methods in Engineering*, 60(14):2312–2333, August 2004.

[53] dA. e Andrés and J.L. Peréz. Elastoplastic finite element analysis of three-dimensional fatigue crack growth in aluminum shafts subjected to axial loading. *International Journal of Solids and Structures*, 36:2231–2258, 1999.

[54] P.A. Wawrzynek. *Discrete modeling of crack propagation : theoretical aspects and implementation issues in two and three dimensions.* PhD dissertation, Cornell University, Department of Civil and Environmental Engineering, May 1991.

[55] Jim Gray, David T. Liu, Maria Nieto-Santisteban, Alexander S. Szalay, David DeWitt, and Gerd Heber. Scientific data management in the coming decade. Technical Report MSR-TR-2005-10, Microsoft Research, January 2005.

[56] K. Delaney. *Inside Microsoft SQL Server 2000*. Microsoft Press, 2002.

[57] Gerd Heber and Jim Gray. Supporting finite element analysis with a relational database backend; part i. Technical Report MSR-TR-2005-49, Microsoft Research, May 2005.

[58] Gerd Heber, Chris Pelkie, Andrew Dolgert, Jim Gray, and David Thompson. Supporting fintie element analysis with a relational database backend; part iii. Technical Report MSR-TR-2005-151, Microsoft Research, December 2005.

[59] IBM Corporation. *IBM Visualization Data Exploration*.

[60] *http://www.python.org*.

[61] Paul Stodghill, Rob Cronin, Keshav Pingali, and Gerd Heber. Performance analysis of the pipe problem, a multi-physics simulation based on web services. Computing and Information Sciences Technical Report TR2004-1929, Cornell University, February 2004.

[62] Paul Chew, Nikos Chrisochoides, S. Gopalsamy, Gerd Heber, Tony Ingraffea, Edward Luke, Joaquim Neto, Keshav Pingali, Alan Shih, Bharat Soni, Paul Stodghill, David Thompson, Steve Vavasis, and Paul Wawrzynek. Computational science simulations based on web services. In *Workshop on Dynamic Data-Driven Application Systems, International Conference on Computational Science*, 2003.

[63] World Wide Wed Consortium. Extensible markup language (xml) 1.0 (second edition). Technical report, W3C Recommendation, 2000.

[64] Valerie Coffman. *http://www.python.org*.

[65] N. Bailey, T. Cretegny, J.P. Sethna, V.R. Coffman, A.J. Dolgert, C.R. Myers, J. Schiotz, and J.J. Mortensen. Digital material: a flexible atomistic simulation code. submitted.

[66] B.R. Lawn and T.R. Wilshaw. *Fracture of Brittle Solid*. Cambridge University Press, 1975.

[67] M.P. OD́ay and W.A. Curtin. Bimaterial interface fracture: A discrete dislocation model. *Journal of the Mechanics and Physics of Solids*, 53:359–382, 2005.

[68] M.L Falk, A. Needleman, and J.R. Rice. A critical evaluation of cohesive zone models of dynamic fracture. *Journal de Physique IV, Proceedings, Pr-5-42-Pr-5-50*, 2001.

[69] Ani Ural. *Modeling and Simulation of Fatigue Crack Growth in Metals Using LEFM and a Damage-Based Cohesive Model*. PhD dissertation, Cornell University, Department of Civil and Environmental Engineering, May 2004.

[70] A. Ural, V. R. Krishnan, and K. D. Papoulia. A damage-based cohesive model for simulating fatigue crack growth. ***in preparation***, 2006.

[71] D.M. Saylor and et al. Statistically representative three-dimensional microstructures based on orthogonal observation sections. *Metallurgical and Materials Transactions A: Physical Metallurgy and Materials Science*, 35 A:1969–1979, 2004.

[72] R.A. Lebenson and et al. Study of the antiplane deformation of linear 2-d polycrystal with different microstructures. *International Journal of Solids and Structures*, 42:5441–5459, 2005.